Measuring Electron Sticking Coefficients using Dust in Plasma

Dissertation

zur Erlangung des Doktorgrades
der Mathematisch-Naturwissenschaftlichen Fakultät
der Christian-Albrechts-Universität zu Kiel

vorgelegt von

Armin Mengel

Kiel, 2025

1. Gutachter:	PD Dr. Franko Greiner
2. Gutachter:	Prof. Dr. Kai Rossnagel

Tag der mündl. Prüfung: 28.03.2025

Abstract

In this work, a novel method for the measurement of electron sticking coefficients at energies in the single-digit electronvolt range was developed, and applied to several materials.
As the charging of objects in contact with plasmas is dominated by electron currents, the electron sticking coefficient is one of the central properties in the description of the interaction between plasmas and solid surfaces. Plasma-surface interaction occurs in the vast majority of technological applications of plasmas, and in many plasma-related research fields. While material properties such as the electron sticking coefficient have been studied for electron energies above roughly $100\,\mathrm{eV}$, the energy range below $10\,\mathrm{eV}$ remains largely unexplored, especially with regards to dielectric materials. However, many plasmas mainly feature electrons with such low energies, incentivizing investigations of low-energy electron-surface interactions.
To this end, an experimental setup, the "Sticking Machine", was developed, set up in the lab and used to measure electron sticking coefficients in this work. The Sticking Machine employs micrometer-sized particles of different materials levitating in the plasma sheath, and a relative measurement and evaluation scheme to determine their sticking coefficients from the charging behavior of the microparticles.
Initially, a new measurement method for the microparticle charge, the pulse excited oscillation method PEOM, was developed. Like other high-precision methods such as the phase-resolved resonance method (PRRM), it bases on externally driven oscillations of the particle in the plasma sheath. However, it reaches the same precision as the PRRM while being faster and more robust with respect to short-term instabilities and perturbations.
Using this new method, the Sticking Machine is implemented as an experiment to measure the sticking coefficients of spherical particles. The relative measurement approach combined with auxiliary particle-in-cell (PIC) simulations is able to resolve the charging difference between conducting and dielectric microparticles in the plasma for the first time, and made it possible to measure the sticking coefficients of SiO_2 and the two widely used polymers MF and PMMA. These results allow for a much more accurate description of dusty plasma systems, and prove the existence of a charging difference between dielectric and conducting surfaces in the plasma. For silica, the theoretical prediction (Bronold et al., *Plasma Phys. Control. Fusion* **59**, 014011 (2017) [1]) of this effect was confirmed.
To be able to measure the sticking coefficients of a wider range of technologically relevant materials such as MgO or Al_2O_3, for which, in contrast to MF and PMMA, theoretical predictions are available as well, the measurement scheme of the Sticking Machine has to be extended to non-spherical microparticles. Non-spherical particles are currently not in the focus of dusty plasma research due to the complications they introduce to experiments, despite their relevance for many real systems. Based on the few previous

experimental investigations on this topic, a combined study using experimental data and simulation results is conducted to find the appropriate Ersatz radius of a non-spherical particle. The Ersatz radius of a non-spherical particle is the radius of a spherical particle with the same charge, and allows for the reduction of non-spherical geometries to a single radius which can directly be used for the charge estimation in dusty plasmas. It is found that the Ersatz radius is directly related to the electrostatic capacitance of the geometry, and that only one of the proposed geometrical approximations for the Ersatz radius, the orientation-averaged equivalent sphere model (OAES) is applicable within certain limits. These new results may contribute to ending the ongoing debate in the dusty plasma field if the OAES model or the smallest enclosing sphere model (SES) is valid for non-spherical particles. Furthermore, the findings allow for the determination of sticking coefficients of materials only available as non-spherical particles, such as MgO or Al_2O_3. With this valid approximation for the Ersatz radius now available, the Sticking Machine can now be used to measure the sticking coefficient of non-spherical particles. Thus, the Sticking Machine is a setup allowing for the determination of the sticking coefficient of any material that can be trapped in the plasma sheath.

Kurzfassung

In dieser Arbeit wurde eine neuartige Methode zur Messung von Elektronenhaftkoeffizienten entwickelt und auf verschiedene Materialien angewendet.
Da die Aufladung von makroskopischen Objekten im Kontakt mit Plasmen von Elektronenströmen dominiert wird, ist der Elektronenhaftkoeffizient (engl. *sticking coefficient*) eine der zentralen Eigenschaften für die Beschreibung von Plasma-Oberflächen-Wechselwirkungen. Diese Wechselwirkungen treten in vielfältigen technischen Anwendungen von Plasmen auf, sowie in vielen plasmabezogenen Forschungsfeldern. Während Materialeigenschaften wie der Elektronenhaftkoeffizient für Elektronenenergien höher als ca. $100\,\mathrm{eV}$ gut untersucht sind, bleibt der Energiebereich unter $10\,\mathrm{eV}$ größtenteils unerforscht. Allerdings beinhalten viele Plasmen hauptsächlich Elektronen bei ebendiesen niedrigen Energien, weshalb Untersuchungen der Interaktion von Oberflächen mit niederenergetischen Elektronen vonnöten sind.
Zu diesem Zweck wurde im Rahmen dieser Arbeit die „Sticking Machine" als experimenteller Aufbau konzipiert, im Labor aufgebaut und zur Messung von Elektronenhaftkoeffizienten verwendet. Die Sticking Machine nutzt mikrometergroße Partikel unterschiedlicher Materialien, die in der Plasmarandschicht levitieren, und ein relatives Mess- und Auswerteschema, um die Elektronenhaftkoeffizienten der Materialien aus dem Aufladeverhalten der jeweiligen Partikel abzuleiten.
Zunächst wurde die pulsangeregte Oszillationsmethode (PEOM) als neue Messmethode für die Partikelladung entwickelt. Wie andere Präzisionsmessmethoden, wie z.B. die phasenaufgelöste Resonanzmethode (PRRM), basiert die PEOM auf extern angeregten Schwingungen des Partikels in der Plasmarandschicht. Allerdings erreicht die PEOM sowohl die gleiche Genauigkeit wie die PRRM, als auch eine deutlich schnellere Messgeschwindigkeit, und ist überdies weniger anfällig gegenüber kurzfristigen Störungen und Instabilitäten. Mithilfe dieser neuen Messmethode wurde die Sticking Machine als experimenteller Aufbau für die Messung von Elektronenhaftkoeffizienten kugelförmiger Partikel implementiert. Das relative Messverfahren in Kombination mit unterstützenden Particle-in-Cell-Simulationen (PIC-Simulationen) erlaubt, die Aufladungsunterschiede zwischen leitfähigen und dielektrischen Mikropartikeln im Plasma erstmals aufzulösen, und die Elektronenhaftkoeffizienten sowohl von SiO_2 als auch der vielfach verwendeten Kunststoffe MF und PMMA zu bestimmen. Diese Ergebnisse ermöglichen eine weitaus genauere Beschreibung staubiger Plasmen, und belegen die Aufladungsunterschiede zwischen leitfähigen und dielektrischen Materialien im Plasma. Im Bezug auf Silica konnte die theoretische Vorhersage (Bronold et al., *Plasma Phys. Control. Fusion* **59**, 014011 (2017)[1]) dieses Phänomens bestätigt werden.
Um die Elektronenhaftkoeffizienten eines breiteren Spektrums an technologisch relevanten Materialien, wie MgO oder Al_2O_3, für die ebenfalls theoretische Vorhersagen existieren, messen zu können, muss das Messschema der Sticking Machine

auf nichtsphärische Mikropartikel erweitert werden. Obwohl sie in vielen realen Systemen vorkommen, sind nichtsphärische Partikel ein zurzeit wenig beforschter Aspekt Staubiger Plasmen, da sie für zusätzliche Komplikationen in Experimenten sorgen. Auf der Grundlage der wenigen bisher durchgeführten experimentellen Untersuchungen wurde eine Studie unter Verwendung von experimentellen Daten und Simulationsergebnissen durchgeführt, um den für verschiedene nichtsphärische Partikel geeigneten Ersatzradius zu bestimmen. Der Ersatzradius eines nichtsphärischen Partikels ist der Radius eines gleich stark elektrisch geladenen sphärischen Partikels, und erlaubt die Reduktion nicht-sphärischer Partikelformen auf einen direkt für die Ladungsbestimmung nutzbaren Radius. Es ergibt sich, dass der Ersatzradius im direkten Bezug zur elektrostatischen Kapazität der Partikelform steht, und dass lediglich eine der vorgeschlagenen geometrischen Näherungen, das Modell der richtungsgemittelten äquivalenten Kugel (OAES), für den Ersatzradius unter bestimmten Voraussetzungen anwendbar ist. Diese neuen Erkenntnisse tragen möglicherweise dazu bei, die Debatte beizulegen, ob OAES oder das Modell der kleinsten einhüllenden Kugel (SES) das für nichtsphärische Partikel gültige Modell ist. Außerdem ermöglichen diese Ergebnisse die Bestimmung von Elektronenhaftkoeffizienten auch für Materialien, welche als Mikropartikel nicht in Kugelform verfügbar sind, so z.B. MgO oder Al_2O_3. Mithilfe der nun zur Verfügung stehenden Näherung kann die Sticking Machine nun für die Messung der Elektronenhaftkoeffizienten nichtsphärischer Partikel verwendet werden. Somit handelt es sich bei der Sticking Machine um einen Aufbau zur Bestimmung des Elektronenhaftkoeffizienten all jener Materialien, die sich in der Plasmarandschicht einfangen lassen.

Contents

Abstract iii

Kurzfassung v

1 Introduction 1

2 Dust charge measurements in dusty plasmas 5
- 2.1 Existing dust charge measurement techniques . . . 5
- 2.2 Resonance-based methods . . . 7
- 2.3 The Pulse-Excited Oscillation Method (PEOM) . . . 9

3 Charging difference between dielectrics and metals 13
- 3.1 Secondary electron emission and electron sticking . . . 13
  - 3.1.1 Differences between high- and low-energy electron emission . . . 14
  - 3.1.2 *Invariant embedding* description of sticking and SEE . . . 17
- 3.2 Predictions and considerations for microparticles in a plasma . . . 18
  - 3.2.1 Influence of the plasma sheath . . . 20

4 Measurement of the dielectric-metal charging difference using spherical particles 23
- 4.1 Experimental concept . . . 23
- 4.2 Floating potential difference . . . 24
- 4.3 Calculation of the sticking coefficient . . . 25
  - 4.3.1 Models for the charging currents . . . 26
  - 4.3.2 PIC simulation . . . 29
- 4.4 Results for SiO_2 . . . 31
- 4.5 Measurements for additional materials . . . 32
- 4.6 Possible limitations of the method . . . 32

5 Extending the method to non-spherical particles 35
- 5.1 Floating potential of non-spherical particles . . . 35
- 5.2 Generalization of the capacitor model . . . 38
  - 5.2.1 Geometrical approximation models for the capacitance . . . 38
  - 5.2.2 Experiments and simulation for sphere aggregates . . . 39
- 5.3 Additional effects of non-spherical geometries . . . 42
  - 5.3.1 Re-sticking and possible correction . . . 42
  - 5.3.2 Transmission through thin walls . . . 42

6 Conclusion 45
- 6.1 Results . . . 45

6.2 Perspectives for the Sticking Machine 46
6.2.1 Application to non-spherical particles 46
6.2.2 Auxiliary simulation 47
6.2.3 Electron energy variation 48
6.3 Perspectives regarding systems featuring plasma-solid interfaces 48
6.3.1 Dusty plasmas/dust in plasma 48
6.3.2 Plasma diagnostics 52
6.3.3 Reactor design 52
6.4 Summary 53

Scientific Contributions 55

Bibliography 108

Declarations 109

Danksagung 111

1 Introduction

The interaction between surfaces and plasmas is central to a wide array of applications at the core of modern technology. Many branches of manufacturing employ plasma processes [2–6], for example in the etching of semiconductors [7–9], surface modification and coating of mechanical and optical parts [10–14], packaging [15, 16] and even for biomaterials [17, 18]. To improve traditional chemical industrial processes, plasma catalysis reactors are developed to eliminate the need for high temperatures or pressures, improve energy efficiency, and enable the usage of the electrical energy provided by most renewable energy sources [19, 20]. Plasma catalysis may provide new reaction routes, and allow for conversion of detrimental or undesired substances into harmless or even usable products, for instance in CO_2 conversion [21–26]. The catalyst surface is of course a crucial site in the used devices, and its interaction with the plasma is of great interest [27, 28]. The plasma-surface interactions at electrodes or the dielectric barrier of dielectric barrier discharges (DBDs) are significantly influencing the generated plasmas [29–36], and their effectiveness in plasma catalysis [23, 37–39]. Surface interactions are also central in plasma medicine treatments [40–46]. Moreover, surface charging of spacecraft and space stations in the plasma of Earth's magnetosphere can pose a hazard for their operation [47–53].
The topic of plasma-surface interactions is also an implicit and fundamental aspect of dust-in-plasma and dusty plasma investigations in basic research, where nano- to micrometer-sized particles charge in the plasma environment. This charging process is governed by the fluxes of electrons, ions and photons to (and from) the particle surface [54, 55], and is able to strongly influence the plasma environment, e.g. through electron depletion (*Havnes* effect) [56–59]. The early stages of nanoparticle growth from reactive gases are also influenced by their ability to absorb plasma electrons [60, 61].

Plasma-surface interactions are often classified according to the different aspects of the plasma interacting with the surface. These aspects encompass the plasma components – ions [62–66], electrons and possibly reactive species [44] – as well as electric fields [46] and radiation [41, 45] resulting from the presence of a plasma. Moreover, synergies between these aspects may enhance surface processes in certain applications [25, 41, 43–45]. While the surface in question is a solid in the majority of applications, the interaction of plasmas with liquid surfaces [67, 68] is of interest in biomedical applications or wastewater treatment [69, 70].

Despite the successes regarding the individual aspects of plasma-surface interaction, the unified theoretical description of the *plasma-solid interface* as a whole proves difficult [71]. A reason for this is the large difference in time- and length scales between solid and plasma: A typical electron Debye length $\lambda_{\mathrm{D,e}}$ in a low-pressure

plasma (electron temperature $T_\mathrm{e} \approx 3\,\mathrm{eV}$, electron density $n_\mathrm{e} \approx 10^{15}\,\mathrm{m}^{-3}$) is on the order of $400\,\mu\mathrm{m}$, while the typical length scale in (crystalline) solids, the spacing of the crystal grid, is on the order of angstrom to a few nanometers. Regarding time scales, the differences are comparably large: the fastest dynamic in the plasma is that of the electrons. Their characteristic frequency, the plasma frequency $\omega_\mathrm{p,e}$, is on the order of $10^9\,\mathrm{s}^{-1}$ for a typical laboratory plasma at low pressure ($n_\mathrm{e} \approx 10^{15}\,\mathrm{m}^{-3}$), so their characteristic time scale is in the range of nanoseconds. Electrons in the solid, however, are packed much denser and can have different effective masses compared to free electrons, resulting in characteristic plasma frequencies on the order of 10^{15} to $10^{17}\,\mathrm{s}^{-1}$, or timescales on the order of femtoseconds and shorter.
These differences of 5 or more orders of magnitude make the plasma-solid interface challenging to model using simulations [71]. Oftentimes, one of the two subsystems (plasma or solid surface) is simplified. Simulations regarding the plasma emulate the surface by introducing coefficients for the processes happening at the surface on impact of plasma particles. These processes include for example electron reflection, secondary electron emission (SEE) by electrons or ions, and sputtering.

In this thesis, the interaction between electrons and the (solid) surface is focused on. These interactions are described mainly by two of the coefficients mentioned above, which represent the probability with which a certain process happens upon electron impact on the surface. The two important processes are electron sticking (or absorption), and electron-induced secondary electron emission (e-SEE, in contrast to the ion-induced secondary electron emission i-SEE). These are quantified by the coefficients S_e and δ, respectively. Generally, these coefficients depend on the energy and impact angle of the impinging electrons. In the majority of applications, the plasma has a comparatively low electron temperature T_e of only a few (typically 3 to 5) eV. Due to the thermal distribution of electron energies, higher energies occur, but with greatly diminished probability. On the contrary, SEE and electron sticking coefficients for most materials are only known for high energies ($\geq 100\,\mathrm{eV}$) from conventional experiments [72]. Measurements for electron energies below $10\,\mathrm{eV}$ were primarily concerned with metallic surfaces [73]. The few measurements for dielectric surfaces faced significant difficulties at low energies and provide no reliable data [74, 75]. These difficulties predominantly arise from the inherently low conductivity of dielectrics, which is on the order of $10^{-15}\,\mathrm{Scm}^{-1}$ for MgO and Al_2O_3, and $10^{-18}\,\mathrm{Scm}^{-1}$ for ceramic SiO_2 [76]. In comparison, typical (noble) metals like Cu, Ag, Au, Pt etc. have electrical conductivities on the order of 10^5 to $10^6\,\mathrm{Scm}^{-1}$ [76]. However, many of the above-mentioned applications feature dielectric or at least non-metallic surfaces, emphasizing the need for low-energy surface coefficients of these materials. This work focuses on the low-energy electron sticking coefficient, and how to create a versatile method to measure it for arbitrary materials, the so-called *Sticking Machine*.

The Sticking Machine [77] is a proposed experimental approach for the determination of low-energy electron sticking coefficients of arbitrary materials that employs single, micrometer-sized particles of the material of interest trapped in the plasma sheath of a low-pressure, radio-frequency-driven parallel plate discharge. The aim of the Sticking Machine is to be a setup which is capable of determining the low-energy electron

sticking coefficients of a wide range of materials provided as micrometer-sized grains. Such an approach would be the first of its kind, and possibly allow the measurement of electron sticking coefficients for materials and energy ranges otherwise inaccessible. The typical microparticles (radius $a \approx 1$ to $10\,\mu\mathrm{m}$) used in the Sticking Machine are well represented by the picture of the plasma-solid interface: For example, a silica microparticle with a radius of $3.5\,\mu\mathrm{m}$ consists of roughly 10^{13} atoms, which justifies the treatment as a solid of macroscopic size. Even the layers on coated microparticles qualify for the treatment as a solid surface as long as they are at least about 50 to $100\,\mathrm{nm}$ thick.
Particles from the material of interest are compared against particles with a known sticking coefficient, eliminating dependencies on absolute parameters in the plasma sheath, such as species densities and temperatures, or the electric field.
As this is a typical *dust-in-plasma* [78] situation, the plethora of diagnostics developed for the field of dusty plasmas are applicable. Of central importance is the charge of the particles, as it is symptomatic for the material's capability to capture the low-energy electrons of the ambient plasma. Particle resonance methods [79–81] developed in the context of dusty plasma research offer a unique way to access the particle charge without relying on the conductivity of the particle material, which makes them invaluable for the investigations on dielectric materials. A relative measurement and analysis scheme then allows for the determination of the low-energy electron sticking coefficient.

The structure of this dissertation is as follows: A new high-precision particle resonance method tailored to the requirements of the Sticking Machine is presented in Chapter 2, based on the contribution [AM1]. Theoretical considerations on the difference between dielectric and metallic particles in terms of charging are given in Chapter 3. The core of this work, the relative measurement concept of the Sticking Machine, is presented along with its results in Chapter 4, based on the contributions [AM2] and [AM3]. The third portion of this work is covered in Chapter 5, which entails investigations regarding the treatment of non-spherical particles in the framework of the Sticking Machine, part of which is covered in the contribution [AM4]. Finally, the work is summarized and an outlook towards future investigations is given in Chapter 6.

2 Dust charge measurements in dusty plasmas

This chapter outlines the contribution [AM1]*, and provides context to the overarching work as well as additional considerations beyond the scope of the publication. After giving a short overview over existing charge measurement techniques, the requirements for a measurement in the framework of the Sticking Machine are considered. Based on these requirements, the design process behind the PEOM is then outlined, and its performance assessed.*

2.1 Existing dust charge measurement techniques

From the beginning of the research on dusty plasmas, it was evident that the charge on the dust particles plays a major role in their interaction with the electrons, ions, electromagnetic fields and other dust particles present in the plasma environment. In the context of this work, accurate charge measurements are critical, as the particle charge is the primary indicator for the underlying charging process. The charging process is in turn affected by the plasma-surface interaction at the particle surface. This chapter is concerned mainly with the measurement of the particle charge. The topic of charging processes is discussed in Chapter 3, while the corresponding investigations are presented in Chapter 4.

Over the years, several approaches for particle charge measurements in dusty plasmas have been developed, often optimized for a certain experimental situation. This situation can be classified by the size, shape, material or optical properties of the particle(s) in question, the number and arrangement of particles (single particle, pair, 1D-chain, 2D-cluster or 3D-cloud), or the kind of plasma environment (plasma bulk, plasma sheath, spatial/temporal afterglow etc.). In the following, an overview over different existing techniques is given, before the focus is shifted towards resonance-based charge measurements, and the PEOM as the method of choice for the Sticking Machine is presented.

While historically, one of the first charge measurement techniques was the classical resonance method by Melzer et al. [79], several other approaches should be mentioned before going into detail regarding resonance methods in Section 2.2. One aspect influenced by the particle charge is their interaction with each other, which is shielded by the highly mobile electrons and oftentimes described by the Yukawa potential (called also Debye-Hückel potential). Sometimes, in situations in which the Debye shielding plays only a minor role, a pure Coulomb potential is used for simplicity. In the simplest case, the trajectories of two interacting particles are tracked, and from their motion,

information about their interaction potential and thus their charge is gained. Examples include particles pushed together by an external dc voltage [82], or one particle being dropped onto the other, resulting in an attenuated oscillation [83]. The rotating electrode method (REM) [84] uses the balance of centrifugal and electrostatic force between the particles in a rotating particle pair to gain information about the particle charge and the screening length. In systems of significantly more particles, the coupling between the particles allows for waves and related phenomena. In two-dimensional clusters of microparticles, Mach cones can be excited using external laser excitation. Analysis of the Mach cone structure allows for the determination of the screening strength and subsequently the particle charge [85]. Another approach is based on dust-density waves (DDW). DDWs have been observed in systems composed of microparticles [86–90] or sub-micrometer particles [91, 92]. Such an approach has been conducted by Tadsen et al. [91], who observed DDWs in a dense cloud of nanoparticles formed from reactive gas in an argon discharge. The observed dispersion relation of the waves, together with a fluid model for the ions, is used to obtain the ion density and velocity. The dust charge can then be calculated from the ion density using the *orbital motion limited* (OML) charging model [54, 55, 93] and the capacitor model [54, 55, 94] assuming spherical particles. In the case of dense dust clouds, electron depletion needs to be considered. A suitable charging model has been discussed by Goertz et al. [58] and adapted for the DDW diagnostic as the *local ion density model* (LIM) by Tadsen et al. [91].

Another approach makes use of the direct interaction between the charged particle and electric fields. The electric field in question can be either intrinsic to the plasma situation, or externally applied. From the trajectory of falling particles, their acceleration can be determined, and translated into the charge with knowledge of the electric field. This approach has been used in rf discharges [95] as well as in the temporal plasma afterglow [96–98]. Techniques using external electric fields include the determination of the charge from the amplitude of particle oscillation in an external, sinusoidal electric field [99], as well as the determination from the trajectories of particles falling through the spatial afterglow that are deflected by a horizontal electric field [100–102].

Other charge measurement methods make use of the interaction between particle charge and light. For example, the charge of silica nanoparticles was obtained from a shift in the infrared absorption spectrum measured using Fourier-transform infrared spectroscopy (FTIR) [103], and the charge on particles on whose surface quantum dots had been deposited was measured exploiting the quantum-confined Stark effect [104]. Methods making use of the Pockels effect have already been applied to measure surface charges in DBD cells [105], which could potentially also be applied to suitable dust particles.

While these various methods exist, none of them meet the requirements for usage in the sticking machine. They either make use of a system of more than one particle, are not easily repeatable, do not work for the highly charged microparticles to be considered in the Sticking Machine project, or require particles of a specific material. However, these criteria can all be fulfilled using resonance (or resonance-based) methods, which are presented in detail in the next section.

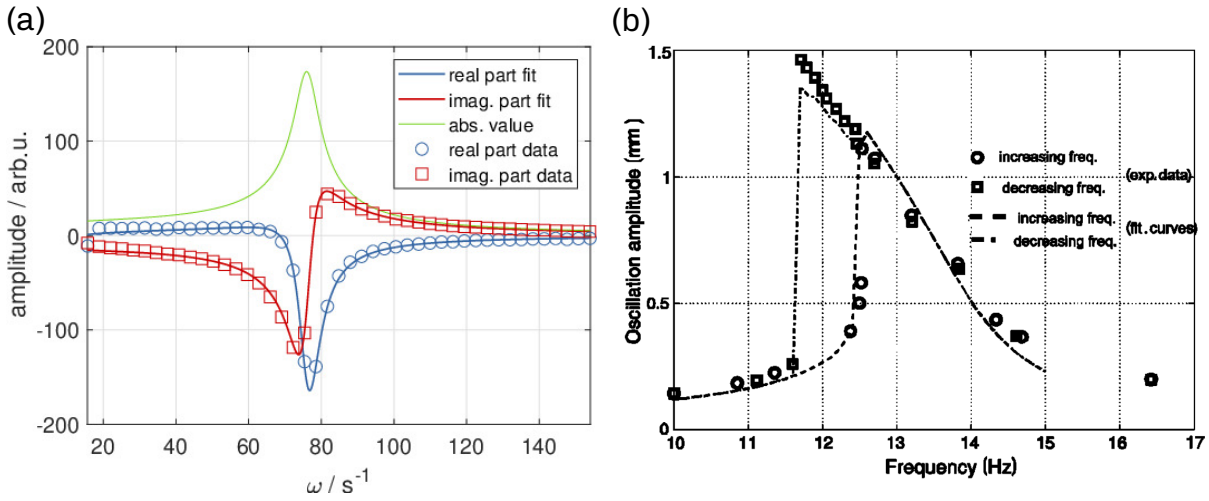

Figure 2.1: Comparison between linear and nonlinear resonance curves. (a) Linear resonance as measured with the phase resolved resonance method (PRRM) [80]. Real (blue) and imaginary part data (red) are shown as markers, with the corresponding fits drawn as solid lines. The green line represents the absolute value of the amplitude as reconstructed from the fits for real and imaginary part. (b) Nonlinear resonance; Only the absolute value of the amplitude is shown for increasing (circles) as well as decreasing (squares) frequency, with respective fits (dashed and dash-dotted lines, respectively). *The figure on the right is reprinted with permission from C. Zafiu et al., Phys. Rev. E* ***63****, 066403 (2001) DOI: 10.1103/PhysRevE.63.066403,* [106]. *Copyright (2024) by the American Physical Society.*

2.2 Resonance-based methods

In 1994, the first resonance method for the measurement of particle charge was presented [79]. Like all subsequent resonance methods, its foundation was the description of the trapped dust particles as harmonic oscillators. The balance between gravitation and electric field force in the lower sheath of a parallel plate reactor provides a vertical confinement. Considering also the neutral gas drag and an arbitrary external excitation, the vertical particle position $z(t)$ with respect to the equilibrium position is given by the equation of motion of the classical, damped and driven harmonic oscillator:

$$\ddot{z} + 2\gamma\dot{z} + \omega_0^2 z = \frac{1}{m} F_{\text{ext}}(t). \tag{2.1}$$

The eigenfrequency ω_0 of this system contains, among others, the charge-to-mass ratio q/m of the particle. For reasonably small amplitudes, the charge can be treated as constant, simplifying the eigenfrequency (using Gauss's law):

$$\omega_0^2 = \frac{1}{m}\frac{d}{dz}\Big(q(z)E(z)\Big) \overset{q\,\text{const.}}{=} \frac{q}{m}\frac{\rho_{\text{q}}}{\varepsilon_0}. \tag{2.2}$$

In the case of significantly higher excitation amplitudes, nonlinear resonances have been observed that need to be considered via higher-order terms [106]. Interestingly, they originate from the height-dependent charge of the particles rather than any

nonlinearity of the sheath electric field. In Fig. 2.1, the resonance curves for linear and nonlinear resonances are compared side-by-side, showing a typical Lorentzian curve for the linear resonance. In the case of nonlinear resonance, the data is dependent on whether the frequency is increased or decreased (similar to a hysteresis), and the resonance curve is strongly skewed to the left.
As a "byproduct" of resonance methods, the neutral gas damping rate γ is also often obtained. For spherical particles, modeling it with the Epstein formula [107] yields information about the mass and radius of the particles. The principle of the measurement has largely remained the same since then: A known external excitation $F_{\mathrm{ext}}(t)$ is coupled into the system, the response of the system is measured, and the eigenfrequency, among other parameters, is extracted from the response by fitting a model function to the data.

The existing resonance methods can be classified regarding the mechanism of the external excitation, as well as the shape of the excitation signal. Excitation mechanisms include modulation of the driving rf-power [81], additional bias voltage on the driven electrode [79, 80, 108–112] or on a thin conductive wire introduced into the plasma [113, 114], random oscillations in many-particle systems [115, 116] and radiation pressure from laser pulses [117]. Another classification is by the mathematical shape of the excitation signal, irrespective of its nature, distinguishing between periodic oscillations leading to a steady state of the particle oscillation, and singular excitations resulting in transient responses back to a ground state.

In the case of the classical resonance method by Melzer et al. [79], the excitation is a sinusoidal voltage signal on the lower electrode with varying frequency ω, allowing to measure the absolute value of the oscillation amplitude $|A(\omega)|$ for each frequency. From this resonance curve, ω_0 and γ are extracted using a model function fitted to the experimental data. A significant improvement was made with the introduction of the phase-resolved resonance method (PRRM) [80], which allowed to measure the real and imaginary part of the response amplitude separately. These carry the same information as the absolute value and phase of the complex amplitude, and can be use to calculate them. The high gradients of the model functions in the vicinity of ω_0 greatly enhance the precision of the method compared to the classical resonance method. The PRRM has since then been the workhorse method for particle q/m measurements in dusty plasmas, due to its high precision and comparatively inexpensive setup. However, the high precision of the PRRM comes at the cost of time resolution, as the resonance curve is recorded one frequency at a time. As a result, a single PRRM measurement can take several minutes.

This can pose a problem for observations on time-dependent systems like the etching of polymer particles. While polymer particles in mostly pure argon plasmas only change over the course of hours [108–110], etching processes with oxygen admixture or in oxygen plasmas are much faster and can occur on the scale of minutes [64, 118–120]. To resolve the evolution of q/m during these processes, a faster method than the PRRM is needed. Another benefit of a faster method concerns the stability of trapped non-spherical particles. Compared to spherical particles, these feature additional degrees of freedom associated with their rotation, which in turn affects their interaction with the sheath electric field and the neutral gas drag. During prolonged external

excitation, it becomes more likely that a particle starts random rotations or oscillations, rendering the recorded resonance curve unusable. This behavior was also theoretically investigated by Krasheninnikov et al. [121]. When replacing a single measurement taking minutes with a series of repetitions of another, much faster measurement, the results of the measurements with erratic behavior can simply be excluded from the evaluation, while still allowing the remaining, unaffected measurements to be evaluated.

2.3 The Pulse-Excited Oscillation Method (PEOM)

By using a singular event as an excitation and evaluating the response of the particle in the time domain, the time requirement can be drastically reduced. In that case, the response is oftentimes some form of attenuated oscillation. Such attenuated vertical oscillations of the particle position have been evaluated in investigations of the interaction potential of particle pairs [83, 122].
Mathematically speaking, a singular excitation event can be described using the Dirac Delta distribution,

$$F_{\mathrm{ext}}(t) \propto \delta(t). \tag{2.3}$$

The Fourier transform of the Delta distribution is constant unity, meaning that every frequency is contained in the spectrum of this signal. Because the response of the particle to a given excitation contains information about the response the frequencies contained in the spectrum of the excitation, the response to a Delta-shaped excitation carries information about all frequencies. In practice, this means that the particle response to a Delta-like excitation carries the same information as a complete resonance curve. A recent approach, the step-wise excitation method [81] (or step-excited oscillation method, SEOM), employed a step-wise switching of the rf voltage driving the plasma as an excitation. The method yielded values for ω_0 and γ for a single particle that agreed with the results of a classical resonance method performed in parallel. However, the rf power had to be changed by approximately a factor of 2 to achieve a clearly resolvable particle motion, which is a significant distortion of the plasma parameters and makes it unsuitable for precision measurements of plasma-surface interaction. Moreover, there was a clear discrepancy between the results depending on the direction of the power step. This discrepancy persisted when reproducing the method for comparisons sake, even though the power change was toned down to ca. 26%. The relative discrepancy in the plasma conditions was estimated based on the dc self-bias voltage U_{sb}, which changed by 10%, and on the rf voltage amplitude $\hat{U}_{\mathrm{RF}}$ that changed by ca. 17%. The strength of this method is that it eliminates the need for a time-consuming frequency sweep.
The new method developed in this work, the pulse-excited excitation method (PEOM), is designed to combine the strengths of the PRRM and step-excitation. The design process is outlined below.

As a first step, the (modulated) step-excitation method is made significantly less invasive by coupling the excitation signal into the system as a bias voltage on the lower electrode (as done with the PRRM [80]), while keeping the step function as the excita-

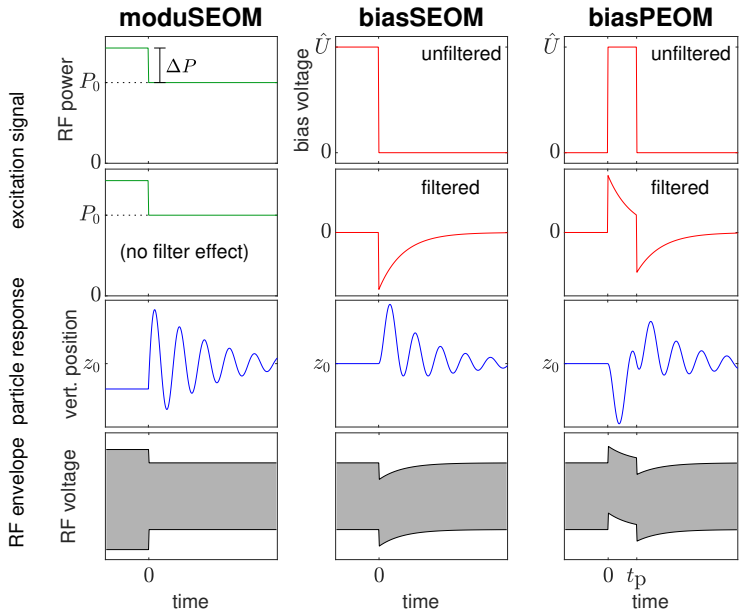

Figure 2.2: Schematic overview over the signal forms of modulated step-wise excitation (moduSEOM, as in [81], left column), bias-excited step excitation (biasSEOM, middle column) and bias-excited pulse excitation (biasPEOM, right column). The upper two rows show the excitation signal before and after the coupling network, while the resulting motion of the particle is displayed in the third row. The low-frequency envelopes of the rf voltage signal at the driven electrode are sketched in the fourth row. *Reproduced from A. Mengel et al., Phys. Plasmas* ***30****, 123704 (2023)* [AM1] *with the permission of AIP Publishing.*

tion signal, resulting in the bias-SEOM method. Doing this keeps the rf power constant, and the excitation amplitude is very small compared to the rf voltage amplitude and the self-bias voltage of the driven electrode, minimizing the effect on the plasma conditions. However, it introduces the need to incorporate the characteristics of the coupling network into the analysis. Thus, the externally applied excitation signal $U_{\mathrm{LF}}(t)$ is distorted by the coupling network into a signal $U_{\mathrm{e}}(t)$. The signal $U_{\mathrm{e}}(t)$ is then coupled into the plasma, so that a force $F_{\mathrm{ext}} \propto U_{\mathrm{e}}(t)$ acts on the particle, which in response follows a trajectory $z(t)$. As a result, the actual force acting on the particle is slightly distorted in comparison to the original excitation signal U_{LF}.
These two steps between the externally applied excitation signal and the particle trajectory are modeled using two Green functions G_{f} and G_{p}, respectively. Green functions are a solution technique for differential equations, where a given Green function solves a specific differential equation. For common differential equations like the damped harmonic oscillator, the Green functions are well known and discussed in theoretical physics and math textbooks, e.g. [123].
By analyzing the circuit diagram of the network (see also Fig 1 in [AM1]), the incoming excitation signal U_{LF} and the distorted excitation signal U_{e} affecting the particle can be related through a 1$^{\mathrm{st}}$-order ordinary differential equation (ODE). Solving this ODE using the respective Green function G_{f}, it is found that the network acts similar to an analog

differentiator, distorting an incoming slope into an exponentially decaying step (which can be seen in Fig. 2.2 as the transition between the first and second row). The next step consists in obtaining the particle response $z(t)$ from U_e. Using a driving force term in Eq. 2.1 proportional to U_e, the resulting 2nd-order ODE of a driven harmonic oscillator is solved by using the Green function G_p of the harmonic oscillator:

$$G_\mathrm{p}(t-t') = \theta(t-t')\frac{\sin\left(\omega_\mathrm{d}(t-t')\right)}{\omega_\mathrm{d}}e^{-\gamma(t-t')}. \tag{2.4}$$

Here, ω_d is the damped eigenfrequency given by

$$\omega_\mathrm{d}^2 = \omega_0^2 - \gamma^2. \tag{2.5}$$

This step from U_e to $z(t)$ can be seen in Fig. 2.2 as the transition from the second to the third row. The solution for $z(t)$ obtained in this way is used as a fit function to obtain ω_d and γ from the position time series measured in the experiment (see [AM1], Sec. II C for details). This approach using the two Green functions of the coupling network and the harmonic oscillator is, in principle, able to produce fit model functions for arbitrary excitation signals.
The bias-SEOM method constructed in this way yields two slightly different sets of results, one for rising and one for falling slopes of the excitation signal. The set for rising slopes, however, contains information about the particle in slightly altered plasma conditions due to the added bias, because the time scale for particle charging ($< 0.5\,\mathrm{ms}$) is much faster than the oscillation period of the particle ($T_\mathrm{osc} \approx 100\,\mathrm{ms}$). This causes a discrepancy between the results for rising and falling slopes to be observed. The results for rising slopes therefore do not represent the unperturbed state of the plasma and particle well, and half of the measurement time is spent obtaining data that yields no accurate information. By reducing the time after a rising and before a falling slope, the excitation signal transitions from a slow square wave ($f = 0.5\,\mathrm{Hz}$, $1\,\mathrm{s}$ time after each slope) to a short pulse (pulse duration $t_\mathrm{p} = 10$ to $100\,\mathrm{ms}$) repeated every second. Thus, the particle response mainly takes place while the plasma conditions are the same as without the external signal, and a particle trajectory that can be evaluated is recorded for every second of measurement time. This second step finalizes the conceptualization of the PEOM as a method combining the strengths of the PRRM and step-wise excitation method.

Interestingly, the incorporation of the coupling network not only greatly improves the fit of the model function to the data, but also introduces the Ohmic plasma resistance R_p into the fit function. This allows for measurements of the plasma resistance using the bias-SEOM or bias-PEOM. Although R_p is also a fit parameter in the PRRM, the complex resonance curve is barely sensitive to R_p, making a determination from the PRRM fit extremely imprecise, if not impossible.

An important parameter for the PEOM is the pulse duration t_p. If chosen as the optimal value $t_\mathrm{p,opt}$, about half a period of the particle oscillation, the best possible precision is achieved. Additionally, the highest ratio of oscillation amplitude to excitation amplitude is reached, so that the PEOM is the least invasive using the optimal pulse duration $t_\mathrm{p,opt}$. This is also visible in Fig. 2.3 c-e: The pulse duration in Fig. 2.3 c is too short, so that the peak-to-peak amplitude of the particle motion is only about $150\,\mu\mathrm{m}$ or 3 pixel. The long pulse duration in Fig. 2.3 e, on the other hand, leads to double the amplitude,

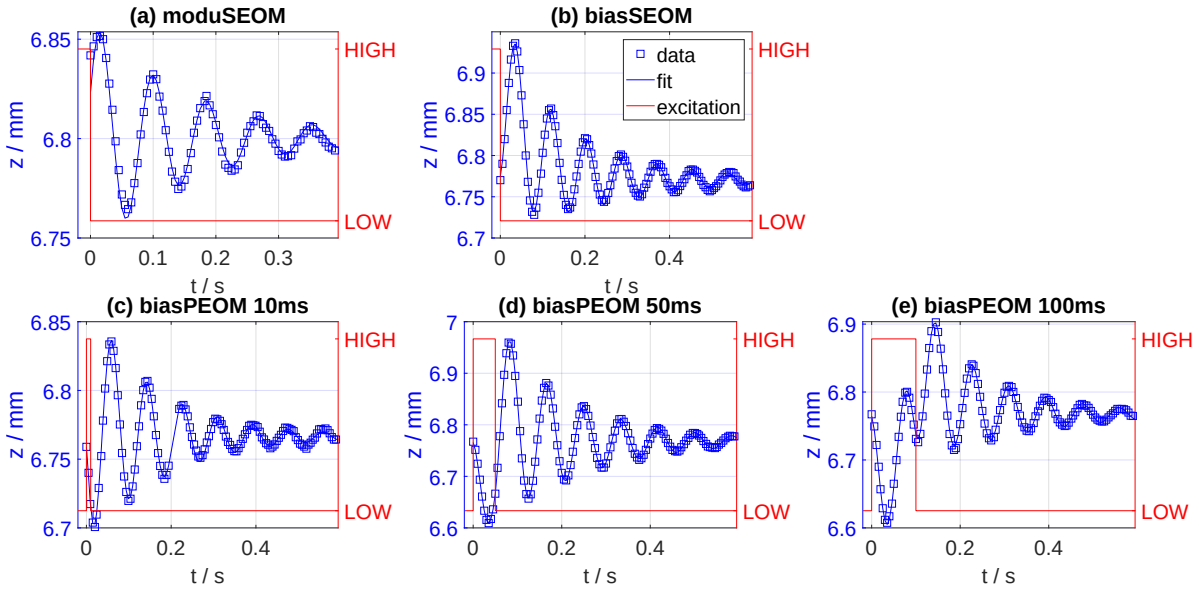

Figure 2.3: Example time series for (a) the modulated step-excitation, (b) the bias-excited step-excitation (SEOM), and the PEOM with different pulse durations (c-e). The excitation signal is shown in red. For the modulated excitation (a) it represents the power modulation, for the bias-excitation (b-e) the additional voltage before the distortion by the coupling network. *Reproduced from A. Mengel et al., Phys. Plasmas* ***30****, 123704 (2023)* [AM1] *with the permission of AIP Publishing.*

but produces a more irregularly shaped trajectory, which impedes the performance of the fit procedure. The data shown in Fig. 2.3 d were measured with a near-optimal pulse duration, resulting in an evenly spaced oscillation with a high amplitude almost 3 times that of the short pulse.
Statistical comparisons between measurements of the same particles using PEOM, PRMM and step-excitation method show that the PEOM is comparable in accuracy to the PRRM and as fast as the step-excitation method. The speed of the PEOM allows for a higher degree of versatility, offering a trade-off between speed and precision by running multiple repetitions of the PEOM.

The short time required for a PEOM measurement indeed qualifies the PEOM as a fast high-precision measurement technique for etching processes of microparticles in a plasma, as argued at the outset of this chapter.
In the context of this work, the PEOM takes on the role of a versatile and robust measurement method for eigenfrequency and damping of microparticles. Especially in the experiments with non-spherical particles (see Chapter 5 and the contribution [AM4]), it reliably provides data even for particles which have become unstable after a few measurement cycles.
Another advantage of the PEOM is that it also serves as a way of monitoring the plasma resistance, which aids in maintaining stable and reproducible plasma conditions throughout later measurements, justifying the relative measurement scheme of the Sticking Machine (see Chapter 4 and Refs. [AM2] and [AM3]).

3 Charging difference between dielectrics and metals

The following chapter provides the theoretical background and context on electron-surface interactions specific to this work, namely electron-induced secondary electron emission (SEE), and electron sticking. After giving some basic context about electron-surface interactions, the case of low-energy ($\leq 10\,\mathrm{eV}$) electrons is discussed. The relevant approach for the modeling of SEE and sticking in this energy range using the invariant embedding *principle is shortly outlined. As a basis for the measurement of electron sticking coefficients in the dust-in-plasma situation in the Sticking Machine, considerations regarding the plasma sheath and the energy distribution of the plasma electrons impinging on the dust particles are finally given.*

3.1 Secondary electron emission and electron sticking

As argued in the introduction, this work's focus lies on the interactions of plasma-facing surfaces with electrons. In the general case of a primary electron hitting a solid surface (wall), this interaction can lead to different outcomes:

- The electron can be absorbed by the wall (*electron sticking/absorption*),
- it can be reflected back elastically or inelastically (*electron reflection*),
- or it can enter the wall, but cause one or more secondary electrons to be emitted (*electron-induced secondary electron emission*). In general, the term *secondary electron emission* (SEE) encompasses the emission of electrons from surfaces due to impinging primary particles. In the context of this project, the focus lies on the emission due to primary electrons, and the term *secondary electron emission* is used with respect to this case.

At very thin walls (10-100 or less monolayers), electron transmission through the whole wall can additionally occur, which is discussed later on in Section 5.3.2. The solid objects of primary interest here, such as electrodes or micrometer-sized dust particles, can be considered thick enough to neglect electron transmission through the whole object. The statistical character of the electron-surface interactions is accounted for by assigning each outcome a coefficient, namely the (electron) sticking probability S_e, the (electron-induced) SEE yield δ_e, and the (electron) reflection probability η_e (sometimes also denoted ρ)*. These coefficients are generally dependent on the primary electron

*To avoid confusion with other quantities in this work, these coefficients are denoted with an index "e", as they refer specifically to electrons.

energy and incident angle, as well as characteristics of the surface such as the electronic structure.

3.1.1 Differences between high- and low-energy electron emission

The phenomenon of electron-induced secondary electron emission is utilized in several applications. The functionality of electron multipliers bases on repeated secondary electron emission at dynodes, which is for example used in photomultiplier tubes and detectors of mass spectrometers. Incident electron energies at each dynode are about $100\,\mathrm{eV}$ [124]. To reach a high overall multiplication efficiency of electron multipliers, a high secondary electron yield of the dynode material at this energy is required [124]. SEE is also a critical aspect of spacecraft charging [125]. The respective electron energies can range from a few eV to the order of keV [125]. One of the most widely used application of SEE, however, is electron microscopy, where electron beams are used to image structures that can not be resolved using conventional microscopes. The usage of electron waves instead of light allows for a much better resolution due their much smaller (de Broglie) wavelength. While transmission electron microscopes (TEM) detect electrons transmitted through the sample, scanning electron microscopes (SEM) rely on secondary and backscattered (reflected) electrons for imaging. In SEMs, the secondary electrons carry important information about the sample surface regions, so that the SEE yield influences the quality and information content of the resulting images. Typical beam energies in TEMs are in the range of hundreds of keV, while SEMs often use beams with 15 to $20\,\mathrm{keV}$ [126]. Low-energy SEM approaches make use of down to $300\,\mathrm{eV}$ beams, and techniques for surface imaging, like low-energy electron diffraction (LEED), operate in even lower energy ranges [126]. The LEED technique was introduced by Davisson and Germer in 1927 [127] and makes use of a collimated electron beam with energies in the range of 30 to $200\,\mathrm{eV}$ [128]. Electrons in this energy range have de Broglie wavelengths of only a few angstrom and can therefore be diffracted at the grid atoms of the target. Moreover, the short mean free path of electrons at these energies means that their interaction is only with the topmost layers of the target, which is why LEED is so suited to probe the surface structure of a target. The spatial diffraction pattern of the scattered electrons then provides information about the two-dimensional structure of the surface. Spot profile analyzing LEED (SPA-LEED) even provides information about the surface morphology derived from the profile of the diffraction spots [129, 130].
In these applications, the electron energies range from some $100\,\mathrm{eV}$ to tens of keV. In contrast, the electrons in a typical laboratory low-pressure plasma like in the Sticking Machine have energies below $10\,\mathrm{eV}$. The interaction of the low-energy electrons of the plasma with the electrodes of rf discharges impacts discharge parameters like the electron density [33, 34]. For an accurate description of electron-surface interaction, the distinction needs to be made between the high-energy case usually considered in applications such as those presented above, and the low-energy case relevant for this work.

In investigations regarding electron-surface interaction in general, the most basic ob-

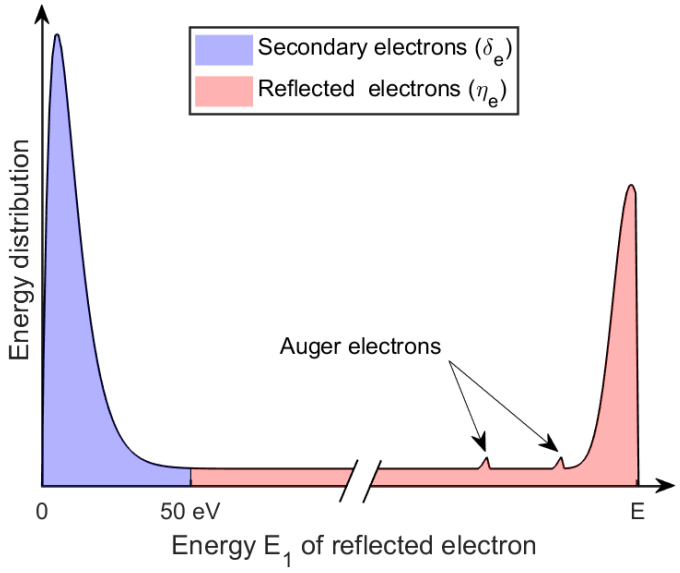

Figure 3.1: Sketch of the energy distribution of emitted electrons for a primary electron with energy $E \gg 50\,\mathrm{eV}$. The blue and red areas represent δ_e and η_e, respectively. Details of the reflected electron peak have been omitted for clarity. *Based on a figure in the work of Schou* [131].

servable quantity is the *total yield* σ_tot [72], which describes the number of emitted electrons per incident electron. For the sufficiently high energies of electron microscopes and similar electron beams, σ_tot is commonly separated into the two components δ_e and η_e, representing secondary electrons and reflected primary electrons, respectively [131]:

$$\sigma_\mathrm{tot} = \delta_\mathrm{e} + \eta_\mathrm{e}. \tag{3.1}$$

For high-energy primaries, the distinction between reflected primary electrons and secondary electrons is typically made according to their energy, counting emitted electrons with energies lower than $50\,\mathrm{eV}$ as secondary electrons, and those with energies above that as reflected primaries. This view neglects the contribution of Auger electrons, which add diminutive peaks to the spectrum in the energy region above $50\,\mathrm{eV}$. A sketch of the energy spectrum of the emitted electrons for high energy primary electrons is shown in Fig. 3.1.
In the case of low-energy ($E \leq 50\,\mathrm{eV}$) primary electrons, this energy-based distinction vanishes, as the energy of the reflected electrons is also in the interval below $50\,\mathrm{eV}$. Consequentially, the situation is simplified by considering only the total emission yield. Furthermore, the primary energy of only a few eV is not sufficient to allow for the emission of more than one secondary electron, as the work function of most materials alone is in the range of eV as well. Therefore, the SEE part δ_e of σ_tot has to be ≤ 1 for the energies considered here. Under these conditions, the sticking coefficient S_e is related to the total yield σ_tot via

$$S_\mathrm{e} = 1 - \sigma_\mathrm{tot}, \tag{3.2}$$

meaning that an incoming electron can either remain in the solid, or cause an emitted electron to be detected. The cause of the latter can be either secondary emission or reflection, but one cannot identify which was the case. It should be noted that, at low

energies, the total yield σ_{tot} is sometimes measured as a low-energy limit of δ_{e} and also denoted δ_{e}, even though it potentially includes reflected electrons.
As mentioned before, the energy range of particular interest in this work encompasses energies below $10\,\mathrm{eV}$. The availability of literature data for low-energy electron emission yields varies greatly depending on the material, because only few conventional measurements provide results. For metals, the emission yield has been measured including this energy range [73]. In the relevant energy range, the emission yield of silver and gold is almost zero [73], indicating a sticking coefficient that is justifiably approximated as constant unity in this energy range. For dielectrics, however, no conclusive measurements exist for energies below $10\,\mathrm{eV}$. Early beam experiments on MgO remained inconclusive [75], while even modern approaches only reach down to a few hundred eV [72]. Two single data points for a primary energy of approximately $10\,\mathrm{eV}$ were reported by Dionne [132] for a thin SiO_2 layer on a Si target. To develop more suitable methods for the measurement of low-energy SEE yields and electron sticking coefficients, one might look at where electrons with respective energies occur: The technological relevance of low-energy electron sticking and emission coefficients, as argued before, mainly concerns plasma devices, where a surface, for example an electrode [33, 34], a catalyst [39] or a dust particle [54, 55, 78], is bombarded with plasma electrons, which typically have mean energies around $5\,\mathrm{eV}$. Conversely, plasma-facing surfaces offer a unique opportunity to study the interaction of low-energy electrons with the surface.
One such approach would entail comparing a measured discharge profile with that of many simulated ones for different sticking coefficients of the electrode, as the latter affects the discharge profile [33, 34]. This also allows to access the sticking coefficient at low energies, as the electrons arrive at the electrode with energies $< 10\,\mathrm{eV}$ [133]. However, this indirect approach has some disadvantages: A precise determination of the sticking coefficient requires simulations for many different values of the sticking coefficient, which is computationally expensive. Moreover, the comparison with the experiment requires precise, spatially resolved measurements of e.g. electron density profiles, which are a challenge in itself, as techniques such as Langmuir probes [54, 134, 135] do not perform well in the plasma sheath and possibly introduce perturbation to the plasma. On top of that, not every material can be used to manufacture or coat an electrode, limiting the range of materials that can be investigated.

To avoid these drawbacks, the dust-in-plasma-based approach was chosen for the Sticking Machine. The dust-plasma system is easier to describe theoretically, and more controllable in the experiment. With methods like the PEOM [AM1], the dust particle charge is measurable regardless of the conductivity of the dust particle, offering an advantage over the current measurements required in beam experiments. Moreover, the material in question is only required in the form of a number of microparticles, so there is no need for extensive preparation of a target. Also, the method promises to be cheaper in terms of material cost, as a much smaller quantity of the material of interest is needed. As a basis for this dust-particle-based measurement scheme, the following considerations lean into the relation between the particle surface material and its charge.

3.1.2 *Invariant embedding* description of sticking and SEE

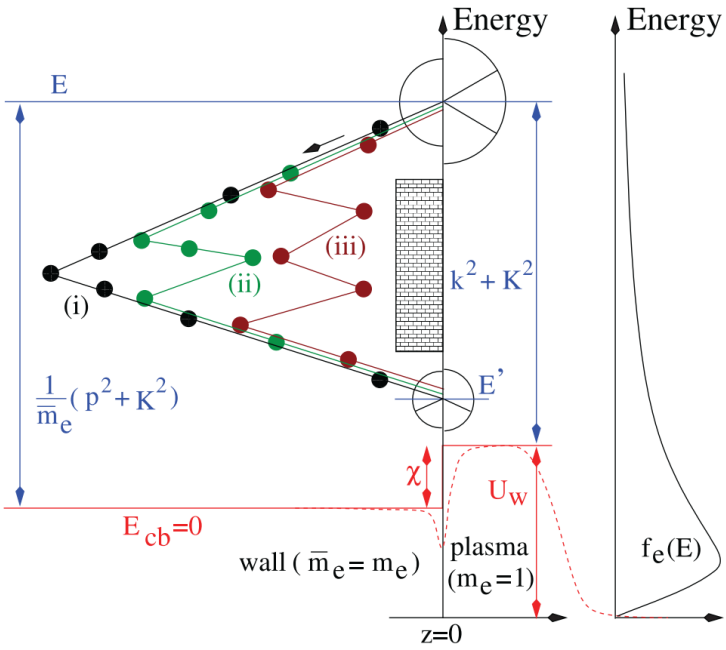

Figure 3.2: Schematic overview over the interface model used in the invariant embedding approach. The interface to the plasma is to the right. Note that the energy axis of the solid starts at the upper edge of the conduction band, so that the wall potential is always χ above zero. The difference between the wall potential and the reference point of the EEDF (sketched vertically on the right) is the energy U_W, which can vary depending on the situation. The solid red line represents the approximation of the surface potential (dashed red line) as a potential step. K is the momentum component of the electron parallel to the surface, while k and p denote the momentum components perpendicular to the surface in the vacuum and inside the solid, respectively. (i)-(iii) are three different scattering trajectories due to interaction with phonons, which result in an energy E' of the scattered electron. *Reproduced from: F. X. Bronold et al., Plasma Phys. Control. Fusion* ***59*** *(2017), 014011* [1]. *©IOP Publishing. Reproduced with permission. All rights reserved.*

As mentioned earlier, the plasma-solid interface is a challenging system due to the large differences in time- and length scales. In order to investigate the interaction of electrons with the surface, ideally all relevant mechanisms have to be considered, regardless of whether they stem from the plasma, the solid, or arise at the interface. Recently, the *invariant embedding principle* has been employed as a technique to describe electron sticking and SEE due to plasma electrons at the surface of solids [1, 136–139]. The invariant embedding technique was first applied by Dashen to electron backscattering [140]. The core principle of invariant embedding is, that certain quantities stay invariant when adding an infinitesimally thin slab of material to the surface. In the works of Bronold et al., this quantity was the probability $Q(E, \tilde{\eta}|E', \tilde{\eta}')$ that an electron with initial energy E and direction cosine $\tilde{\eta}$ that has already entered the surface is scattered

into a state with the energy E' and the direction cosine $\tilde{\eta}'$. Besides this central scattering quantity, other aspects have to be considered in the interface model. An overview over the interface model used for the calculation of electron sticking at dielectric surfaces is sketched in Fig. 3.2. The sticking probability $S_\mathrm{e}(E, \xi)$ is generally angle- and energy-dependent. To include this fact, each incoming electron has an energy from the electron energy distribution function (EEDF) $f_\mathrm{e}(E)$ of the plasma electrons in the sheath, and an incident angle β represented by its cosine $\xi = |\cos\beta|$. To even reach the solid surface, it has to have at least the energy corresponding to the wall potential U_W. In the case of dusty plasmas, this wall potential is given by the floating potential Φ_f of the dust particle. This portion of the electrons with $E \geq U_\mathrm{W}$ is counted as the incoming electrons. To enter the solid, i.e. occupy a state in the conduction band, the electron has to pass over a potential step the size of the electron affinity χ. This functions as a quantum mechanical barrier. The description of the latter has to account for the additional difference in effective electron mass $\bar{m}_\mathrm{e}$ between vacuum and conduction band. Dependent on angle and energy, the electron is then either quantum-mechanically reflected back into the vacuum, or transmitted into the conduction band of the solid. Transmitted electrons are then subject to scattering with (optical) phonons, dissipating their kinetic energy. Each scattering event can either be forward- or backward scattering, potentially allowing electrons to reach the surface again with reduced energy. At the surface, these electrons again interact with the quantum-mechanical potential barrier, allowing for a transmission back into the vacuum. The approach also considers surface impurities and roughness through a parameter C indicating the degree of order of the surface, from a perfectly clean ($C = 0$) to a completely disordered surface ($C \to \infty$). In accordance with the processes described above, the surface material is additionally characterized by the electron affinity χ and the effective mass $\bar{m}_\mathrm{e}$ for the description of the quantum-mechanical transmission, and the phonon energy ω. Using this approach, low-energy electron sticking coefficients for the dielectrics MgO, Al_2O_3 and SiO_2 have been predicted [1]. Closely related approaches designed for metals additionally considered electron-electron and electron-ion core scattering and predicted electron emission yields for the metals Al, W, Cu, Ag and Au [137, 138]. Thus, invariant embedding is a powerful theoretical approach for the description of low-energy electron-surface interaction.
The predictions for low-energy electron sticking coefficients are a solid foundation for experimental studies. However, the resulting sticking coefficient $S_\mathrm{e}(E, \xi)$ is a function of electron energy and incident angle. In contrast to monoenergetic, directed electron beams, where energy and angle are the same for all electrons, the conditions in the plasma environment are different, and electron energies and angles are distributed. This is considered in the following section, where the connection to the experimental dust-in-plasma situation is made.

3.2 Predictions and considerations for microparticles in a plasma

To produce a result that is more easily transferred to the experimental context, the resulting energy- and angle-dependent sticking probability $S_\mathrm{e}(E, \xi)$ is averaged over all possible incident angles and over the portion of the EEDF with $E \geq U_\mathrm{W}$. The angle av-

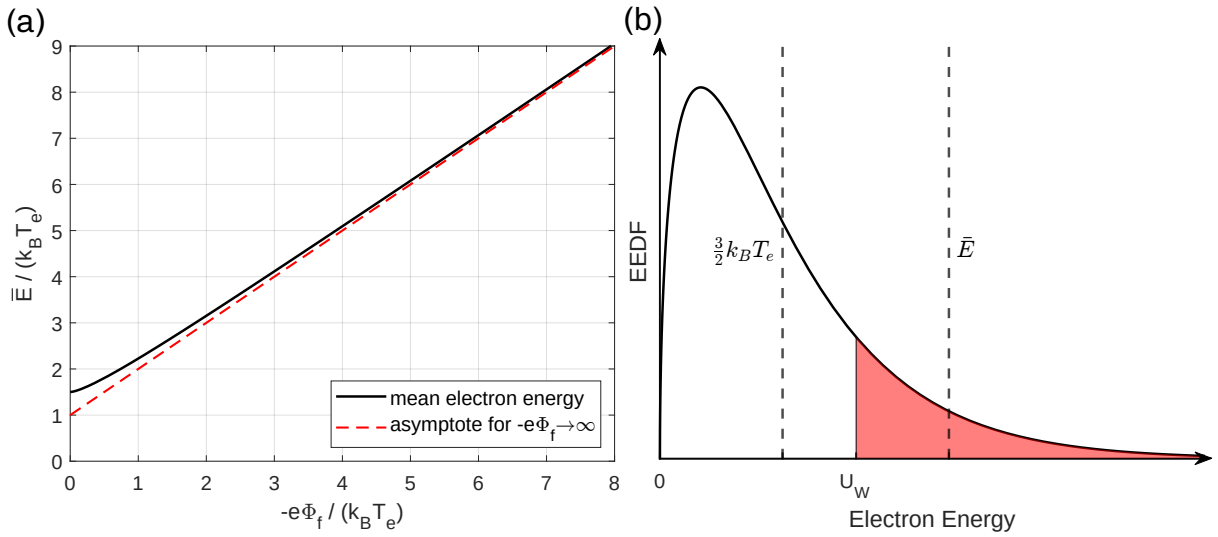

Figure 3.3: (a) Mean energy $\bar{E}$ from Eq. 3.3 dependent on the floating potential Φ_f (black solid line). The linear asymptote for high wall potentials $U_\mathrm{W} = -e\Phi_\mathrm{f}$ is shown as a red dashed line. For $U_\mathrm{W} = 0$, the mean energy $\frac{3}{2}k_\mathrm{B}T_\mathrm{e}$ of the whole Maxwellian distribution is reproduced. (b) Visualization of the Maxwellian distribution, with the mean energy $\frac{3}{2}k_\mathrm{B}T_\mathrm{e}$ of the whole distribution drawn in. The red area corresponds to the part of the portion of the electrons able to overcome the wall potential U_W. The respective mean energy $\bar{E}$ of this "tail" is also marked. For this example, $U_\mathrm{W} = 2.41 k_\mathrm{B}T_\mathrm{e}$, which is a value found for the floating potential in the bulk of argon plasmas [54, 55].

eraging is done by assuming an uniformly distributed direction cosine (see [1], Eq. 28). This yields an averaged sticking coefficient $\tilde{s}$ corresponding to a specific EEDF. In most dusty plasmas, the electron energies follow a Maxwell-Boltzmann distribution with an electron temperature T_e of 2 to $5\,\mathrm{eV}$, so that $\tilde{s}$ is best parametrized by the floating potential Φ_f and either the electron temperature T_e, or the mean electron energy $\bar{E}$. When calculating the latter, it must be considered that only electrons with $E \geq U_\mathrm{W} = -e\Phi_\mathrm{f}$ even reach the surface. Also, the energy scale of the plasma is used, in the reference point of the solid energy scale sits at $U_\mathrm{W} - \chi$ (see also Fig. 3.2). The mean energy $\bar{E}$ is therefore given by

$$\bar{E} = \frac{\int_{U_\mathrm{W}}^{\infty} E f_\mathrm{e}(E) dE}{\int_{U_\mathrm{W}}^{\infty} f_\mathrm{e}(E) dE} = k_\mathrm{B}T_\mathrm{e} \frac{u^{3/2}e^{-u} + \frac{3}{2}u^{1/2}e^{-u} - \frac{3\sqrt{\pi}}{4}\left[\mathrm{erf}(u^{1/2}) - 1\right]}{u^{1/2}e^{-u} - \frac{\sqrt{\pi}}{2}\left[\mathrm{erf}(u^{1/2}) - 1\right]}, \tag{3.3}$$

where $u = U_\mathrm{W}/(k_\mathrm{B}T_\mathrm{e}) = -e\Phi_\mathrm{f}/(k_\mathrm{B}T_\mathrm{e})$. This function $\bar{E}(\Phi_\mathrm{f})$ is visualized in Fig. 3.3 (a). As the Maxwell-Boltzmann distribution decays exponentially towards higher energies, $\bar{E}$ lies not far from the lower end of the distribution's "tail", i.e. the portion above U_W. This is visualized in Fig. 3.3 (b). Therefore, the majority of electrons have energies near $\bar{E}$.

In the work of Bronold et al. [1], predictions for the averaged sticking coefficients $\tilde{s}$ and resulting charges of $2\,\mu\mathrm{m}$-diameter particles made from SiO_2, Al_2O_3 and MgO in

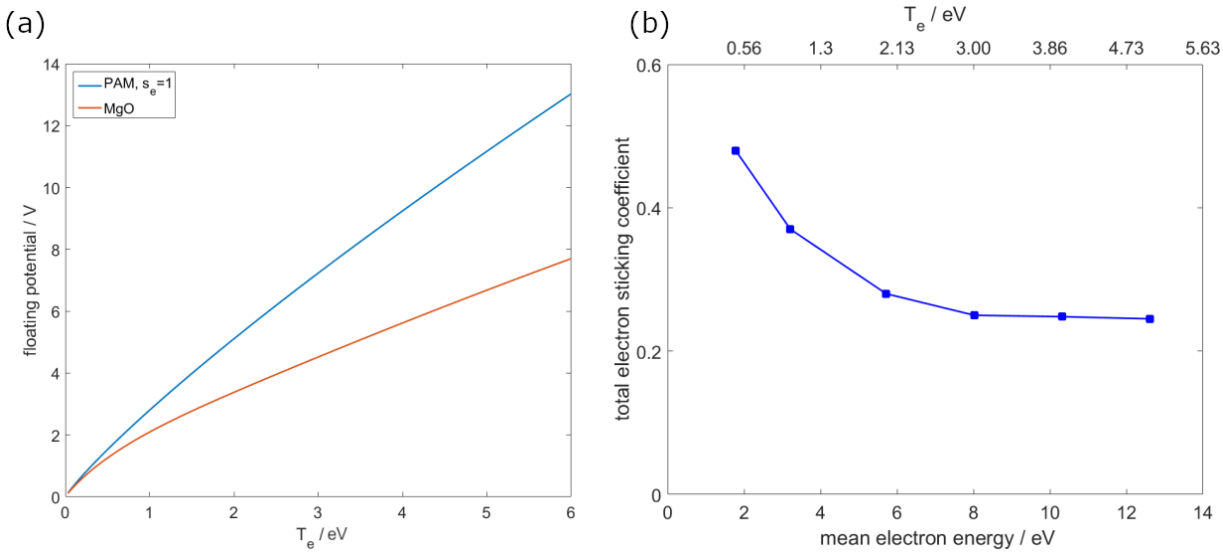

Figure 3.4: (a) Floating potential in dependence of electron temperature, for a perfectly absorbing particle (PAM, blue) and a MgO particle (red) in an argon plasma. The argon ions were assumed to be at room temperature ($k_\mathrm{B}T_\mathrm{i} = 0.026\,\mathrm{eV}$). (b) Energy dependence of the averaged sticking coefficient $\tilde{s}$. The lower x-axis displays the mean electron energy of the maxwellian tail starting at the floating potential given in (a), while the upper x-axis shows the corresponding electron temperature T_e. *Edited after: Private communication F. Greiner/F. X. Bronold.*

an argon plasma have been computed and compared to the *perfect absorber model* (PAM). The floating potential Φ_f needed for these results was obtained as the solution of a modified current balance for the charging of the particle, where the charging currents are modeled using the *orbital motion limited* (OML) [54, 55, 93] expressions:

$$\tilde{s} I_\mathrm{e}^\mathrm{OML}(\Phi_\mathrm{f}) + I_\mathrm{i}^\mathrm{OML}(\Phi_\mathrm{f}) = 0. \tag{3.4}$$

The corresponding electron and ion temperatures were $2\,\mathrm{eV}$ and $0.026\,\mathrm{eV}$, respectively. The particle charge was then obtained from Φ_f via the standard spherical capacitor model [54, 55]. Results for the floating potential of a PAM particle and a MgO particle are shown in Fig. 3.4 (a) plotted over the electron temperature. Using the floating potential arising from the charging current balance, and the relevant portion of the Maxwellian EEDF, the variation of the averaged sticking coefficient $\tilde{s}$ with the electron temperature T_e is obtained, which is shown in Fig. 3.4 (b).

3.2.1 Influence of the plasma sheath

It has been demonstrated that the portion of the plasma electrons reaching the dust particle surface depends on its floating potential. Eq. 3.4 describes the connection between the floating potential and the electron sticking coefficient at the respective energy. Apart from the sticking coefficient, the charging process is also influenced by the plasma environment itself. The microparticles used here levitated in the plasma sheath, warranting

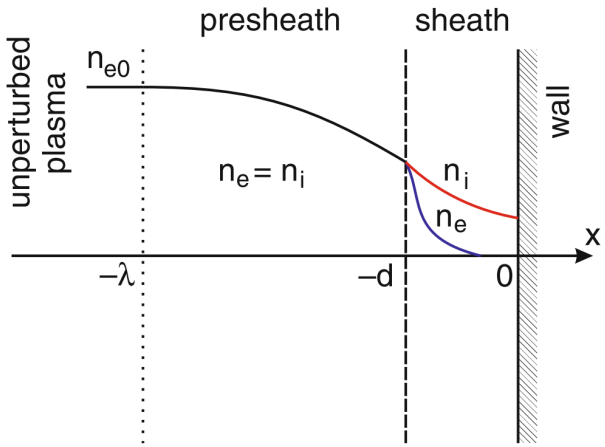

Figure 3.5: Illustration of the electron and ion density profiles in the plasma sheath and presheath. The wall sits at $x = 0$, and the plasma extends in negative x direction. The sheath width is denoted d, the Debye length is denoted λ and n_{e0} is the bulk plasma density. While the quasineutrality is valid in the unperturbed plasma and the presheath, the electron density n_e in the sheath is much lower than the ion density n_i. *Reproduced from: A. Piel, "Plasma Physics: An Introduction to Laboratory, Space, and Fusion Plasmas" (Springer, 2010)* [54] *with permission of Springer Nature.*

a brief description of the characteristic properties of the plasma sheath in comparison with the plasma bulk. This description mainly follows the explanation given in the textbook by Piel [54], where in-depth explanations are given.
A plasma sheath forms when a plasma is in contact with a wall, which can also be considered an interaction between plasma and surface that impacts the plasma. Due to the much higher thermal velocity of the electrons, the electron current onto the wall is initially much stronger than the ion current, resulting in a negative potential on the wall. If the wall is electrically floating, this corresponds to the floating potential of a dust particle. Another consequence of the initially much higher electron current is the formation of a region adjacent to the wall where the quasineutrality of the plasma no longer holds, i.e. the ion density is higher than the electron density. This region is called the plasma sheath, or *space charge sheath*. Between the plasma bulk and the sheath, a transition region, the *presheath*, forms, where quasineutrality holds, but the overall plasma density is reduced with respect to the plasma bulk. At distances further than the Debye length away from the wall, the plasma is unperturbed. The density profiles in the sheath and presheath are schematically drawn in Fig. 3.5. In this model, the sheath can be described using the *Child-Langmuir law* [141, 142]:

$$j_\mathrm{i} = \frac{4}{9}\varepsilon_0 \sqrt{\frac{2e}{m_\mathrm{i}}} \frac{U^{3/2}}{d^2}, \tag{3.5}$$

where j_i is the ion current density in the sheath, U is the fixed voltage drop across the sheath, and d is the sheath thickness. The ion current density is additionally constrained by the *Bohm* criterion:

$$u_{\mathrm{i},0} \geq v_\mathrm{B} = \sqrt{\frac{k_\mathrm{B} T_\mathrm{e}}{m_\mathrm{i}}}. \tag{3.6}$$

The Bohm criterion states that the velocity $u_{\mathrm{i},0}$ of the ions at the sheath edge (the boundary between presheath and sheath) has to be greater than or equal to the Bohm velocity v_{B}, which is the speed of sound of the ions. Due to this constraint and the fixed voltage drop U, the sheath width d adjusts to fulfill the Child-Langmuir law.

In rf plasmas, the situation is slightly different, as the electrons are oscillating back and forth with the rf voltage signal, while the ions remain almost unaffected due to their much higher inertia. As a result, the whole sheath oscillates with the rf frequency [2]. For the dynamics of ions and dust particles, it is reasonable to consider the time-averaged electron density instead. This also leads to a slightly different formula for the Child law in rf discharges, which retains its scaling with $U^{3/2}$ [2].
In recent times, more sophisticated sheath models have been developed. For example, the influence of collisions on the validity and existence of the Bohm criterion has been studied [143], and a model with regard to the influence of the sheath on dust particles have been developed by Douglass et al. [144].

Regardless of the complexity of the used sheath model, the existence of the sheath has consequences for the dust-in-plasma situation. The electric field arising from the positive space charge in the sheath facilitates the levitation of the negatively charged dust particles in the sheath, and provides the potential well used for the resonance-based methods (see also Chapter 2). However, the directed ion motion through the sheath also distorts the ion velocity distribution, which has consequences for the ion charging current onto a dust particle. This is discussed later on in Section 4.3.1. Additionally, the anisotropy of the ion velocity distribution may lead to inhomogeneous surface particles on non-conductive dust particles, which is discussed in Section 5.1. Most importantly, the electron and ion energy distributions as well as their densities vary with the position in the sheath. As a consequence, the charging currents and therefore also the floating potential, which depend on the densities and energy distributions, are generally height dependent in the sheath, which has also been discussed by Douglass et al. [144]. This is an important aspect in the evaluation of the Sticking Machine experiments, and is considered by the evaluation scheme.

To conclude this chapter, low-energy electron-surface interaction differs from the high-energy case. The low-energy electron sticking coefficient is closely related to the low-energy secondary electron yield. It is dependent on the energy of the impinging electrons, and determines which floating potential a surface in a plasma attains. This, in turn, influences the portion of plasma electrons that can reach the surface. The floating potential of a dust particle is directly connected to its charge q, so that the particle charge is sensitive to the energy- and angle-averaged electron sticking coefficient of its surface. The particle charge q, as argued in Chapter 2, is a well measurable parameter in dust-in-plasma situations. In principle, knowledge of the surrounding plasma, mainly the electron temperature, allows for a determination of the averaged sticking coefficient from the floating potential, which in turn is linked to the particle charge. This connection enables a new approach for the determination of sticking coefficients using dust in plasma. The experimental realization of this approach is the subject of the next chapter and the corresponding publication.

4 Measurement of the dielectric-metal charging difference using spherical particles

This chapter presents the method used in the publications [AM2] and [AM3], which is at the core of the Sticking Machine. In addition to the results for the sticking coefficients of silica and two polymers often used in dusty plasma research, considerations beyond the publications and the supplemental material are given.

4.1 Experimental concept

After discussing the theoretical background in Chapter 3, the experimental procedure and the analysis scheme used in the Sticking Machine will be presented here. The experimental determination of the electron sticking coefficient of a given material comes down to two steps: First, the particle charge needs to be measured, before the sticking coefficient is obtained in a second step. To avoid unknown quantities and eliminate uncertainties, a relative measurement scheme is chosen, which is described in Secs. 4.2 and 4.3. In the framework of the relative measurement scheme, particles of a material of interest (*grains of interest, GOI*) are compared against particles of a material for which the sticking coefficient is known. To this end, single particles of both materials are, one after another, trapped in the lower sheath of a low-pressure discharge. Their respective particle radius a is measured in situ using long-distance microscopy, while the oscillator parameters ω_0 and γ are measured using PEOM (see Chapter 2) or PRRM [80]. The primary investigations focused on SiO_2 as a material of interest due to the availability as spherical microparticles, the existence of theoretical predictions [1], and the long-time stability in the plasma [145]. Subsequent investigations also yield sticking coefficients for the polymers polymethyl methacrylate (PMMA) and melamin formaldehyde (MF), see Section 4.5. Based on the results of Gonzalez et al. [73], gold is chosen as the reference material, with its sticking coefficient approximated as constant unity in the energy range in question. Due to the high mass density of gold (about ten times that of silica), a solid gold particle levitating in a typical low-pressure plasma sheath would have to be significantly smaller than a silica particle levitating roughly at the same position. Instead, gold-coated melamin formaldehyde particles are used, because their mean mass density is comparable to that of silica. The coating thickness of 50 to $250\,\mathrm{nm}$, which amounts to some 10^2 to 10^3 atom layers, ensures that the gold layer acts as a solid body and is unaffected by thin-film effects.

4.2 Floating potential difference

In order to resolve the difference in the charging of two particles due to the different surface material, all other factors leading to a charge difference need to be eliminated. Firstly, the spherical capacitor model states that the charge q of a dust particle scales linearly with its radius a as well as its floating potential Φ_f:

$$q = 4\pi\varepsilon_0 a\Phi_\mathrm{f}. \tag{4.1}$$

The floating potential itself is independent of the particle size, and is therefore easier to compare between particles. Secondly, the floating potential is the potential at which the charging currents on the particle are in balance. In contrast to astrophysical situations, photoemission and electron emission due to high-energy primaries are not relevant charging mechanisms in the laboratory context [54, 55, 78]. The resulting current balance therefore only consists of the ion and electron collection currents, where the latter is attenuated by the averaged electron sticking coefficient:

$$\tilde{s}I_\mathrm{e}(\Phi_\mathrm{f}) + I_\mathrm{i}(\Phi_\mathrm{f}) = 0. \tag{4.2}$$

The magnitude of the collection currents generally depends on plasma parameters such as the electron and ion densities n_e and n_i and their velocity or energy distribution functions. Maxwellian distributions are defined by their temperatures T_e and T_i, while other distribution functions may require more parameters. As the particles levitate in the plasma sheath, densities and temperatures, and consequentially also Φ_f, are dependent on the position in the sheath (see also Section 3.2.1), which is described by the height h above the lower electrode in this work. For this reason, the charging conditions are only comparable for particles at the same position in the sheath. Due to the unknown sticking coefficients of the material of interest, and the size distribution of the microparticles, the charge-to-mass ratio q/m of the particles, which determines the levitation height h, cannot be predicted accurately. As a consequence, two particles of different materials levitating at the same height is a situation that cannot be deliberately generated in the experiment. Therefore, an interpolation approach is chosen. A multitude of gold-coated reference particles with different sizes are utilized to obtain a calibration curve for the following auxiliary quantity η:

$$\eta(h) := \frac{m\omega_0^2}{4\pi a} = \Phi_\mathrm{f}(h)\rho_\mathrm{q}(h). \tag{4.3}$$

This calibration curve spans an interval of several millimeters in height, which makes up a substantial portion of the sheath thickness of roughly $7.5\,\mathrm{mm}$. The quantity η has the useful property that it links the measured quantities (m, ω_0 and a) to the otherwise experimentally inaccessible and position-dependent floating potential Φ_f and space charge density $\rho_\mathrm{q} = e(n_\mathrm{i} - n_\mathrm{e})$. Values for η of the reference particles are calculated from the measured values of the eigenfrequency ω_0, the damping rate γ, and the particle radius a. The particle mass m is obtained from the damping rate employing the Epstein friction model for spheres [107].
As both Φ_f and ρ_q are expected to be continuous functions of the height h, it is justified to interpolate between the measured values for η of the gold reference particles, resulting

in a reference curve $\eta_{\mathrm{Au}}(h)$. In the original *StickingCube* setup (see Chapter 3), $\eta_{\mathrm{Au}}(h)$ was interpolated in a height interval spanning ca. $0.9\,\mathrm{mm}$ using a linear fit. The levitation heights of the gold particles in the upgraded *StickingCube II* chamber were more evenly distributed, allowing for the interpolation of $\eta_{\mathrm{Au}}(h)$ over a range of ca. $4.1\,\mathrm{mm}$ via a 5$^{\mathrm{th}}$-order polynomial fit.
The η value of a virtual gold particle levitating at the height h in the sheath is provided by $\eta_{\mathrm{Au}}(h)$. This allows for the direct comparison between a measured particle of the material of interest, and a virtual gold reference particle levitating at the same height. When forming the ratio between the η values of the grain of interest (GOI) and the reference curve, the space charge density drops out and the floating potential ratio Y remains:

$$\frac{\eta_{\mathrm{GOI}}}{\eta_{\mathrm{Au}}(h_{\mathrm{GOI}})} = \frac{\Phi_{\mathrm{f,GOI}}}{\Phi_{\mathrm{f,Au}}} =: Y. \tag{4.4}$$

As the charging conditions and the EEDF, which influence the sticking coefficient of the GOI particles, can vary with the position on the plasma sheath, a variation of Y with h is expected and can be observed in the experimental data. Based on the Measurements in [AM2], the values of Y for SiO_2 are in the range of 0.62 to 0.71 with an uncertainty $\Delta Y < 0.083$. Therefore, there has to be a significant difference in the charging process between gold and SiO_2 surfaces at low electron energies. Building upon this result, the sticking coefficient of SiO_2 is quantitatively determined, as shown in the following section.

4.3 Calculation of the sticking coefficient

As argued initially, the floating potential Φ_{f} of a dust particle is sensitive to the average electron sticking coefficient $\tilde{s}$ of its surface. The connection between Φ_{f} and $\tilde{s}$ is made using the steady state charging current balance:

$$\tilde{s} I_{\mathrm{e}}(x) + I_{\mathrm{i}}(x) = 0 \tag{4.5}$$

$$\Rightarrow \tilde{s} = -\frac{I_{\mathrm{i}}(x)}{I_{\mathrm{e}}(x)}, \tag{4.6}$$

where $x = -e\Phi_{\mathrm{f}}/(k_{\mathrm{B}}T_{\mathrm{e}})$ is the reduced floating potential. Eq. 4.6 can be solved for $\tilde{s}$, given that the terms for $I_{\mathrm{e}}(x)$ and $I_{\mathrm{i}}(x)$ are known. Different charging models lead to different terms for I_{e} and I_{i}, and potentially to additional parameters governing the charging currents. Two such models will be discussed later in this section, the standard OML model [93] as a first approximation, and a modified version accounting for the directed motion of the ions in the sheath, which is used for the quantitative evaluation. The choice of model has to reflect the conditions in the experiment as accurate as possible, otherwise systematic errors of the sticking coefficient are introduced.
To make use of the results of the relative measurement scheme, the following steps are taken: First, Eq. 4.6 is solved for x using the known sticking coefficient $\tilde{s}_0$ of the reference material and the chosen charging current model, yielding the reduced floating potential x_0 of the (virtual) reference particle. In this case, the reference material is gold, and $\tilde{s}_0$ is set to 1, because the electron emission yield in the expected energy range $\leq 10\,\mathrm{eV}$ is

very close to zero. In the second step, the floating potential x of the material of interest is written as

$$x = x_0 Y, \tag{4.7}$$

where Y is the measured floating potential ratio between the grain of interest and the virtual reference particle. Using Eq. 4.6, the sticking coefficient $\tilde{s}$ of the material of interest is then calculated. This evaluation is done for each grain of interest, allowing for a potentially high number of repeated measurements given enough particles of the material of interest.
To conduct this evaluation in practice, knowledge about three aspects (in addition to the experimental data) is needed:

1. A value for $\tilde{s}$ of the reference material in the respective energy range is needed. As argued above, gold is expected to have $\tilde{s} \approx 1$ for the energy range up to ca. $10\,\mathrm{eV}$.

2. Expressions for I_e and I_i are needed. To this end, a charging model has to be chosen.

3. Depending on the charging model, additional parameters such as electron and ion densities and temperatures, or the electric field are required to calculate I_e and I_i. *Particle-in-cell* (PIC) simulations are employed to obtain information about these parameters.

The first point has already been discussed above. In the following, the latter two points will be addressed, beginning with the charging model, before a short description of the used PIC simulation is given. The evaluation procedure is then summarized at the end of the section, and in Fig. 4.2.

4.3.1 Models for the charging currents

In order to obtain expressions for I_e and I_i, a charging model has to be chosen. One of the most fundamental charging models is the OML model [93]. In the OML model, electrons and ions are approaching the dust particle from infinity on collisionless trajectories. Only the electrostatic force of the dust particle on the electrons and ions is considered, which generates a situation analogous to Rutherford scattering. A critical impact parameter is formulated based on the ion or electron velocity and the potential of the dust particle, giving rise to an expression for the cross-section for charge collection. Based on this cross-section, expressions for the ion and electron currents are then found. More in-depth illustrations of the OML model are given in plasma physics textbooks [54, 55]. Despite being based on several assumptions which are discussed below, a central result of the OML model is that the floating potential of a dust particle is independent of its size, which is used in the η calibration curve introduced in Section 4.2.

The initial charge predictions by Bronold et al. [1] were made using the OML model. Using the well-known expressions for the OML charging currents [54, 55, 93], Eq. 4.6 takes the following form:

$$\tilde{s} = \frac{e^x}{\varepsilon\sqrt{\mu\tau}}(1 + \tau x). \tag{4.8}$$

The only parameters governing the charging process in the OML model are the temperature ratio $\tau = T_\mathrm{e}/T_\mathrm{i}$ of electrons and ions, their mass ratio $\mu = m_\mathrm{i}/m_\mathrm{e}$, and the ratio

$$\varepsilon = \frac{\langle n_\mathrm{e} \rangle}{n_\mathrm{i}}. \tag{4.9}$$

Here, $\langle n_\mathrm{e} \rangle$ is the electron density averaged over one oscillation cycle of the rf voltage of ca. $73.7\,\mathrm{ns}$, which is multiple orders of magnitude faster than typical particle charging times. The usage of only the time-averaged value for n_e is therefore justified.
However, the OML model bases on several assumptions. For one, it considers a collisionless situation, which is only valid at low pressures [146, 147]. The experiment is operated at $7.5\,\mathrm{Pa}$, so approximating the plasma as collisionless in the vicinity of the dust particles would be justified. However, in the standard OML model, the electron and ion velocities both follow Maxwell distributions. This may be justified for an isotropic situation such as in the plasma bulk, but it does not hold for the plasma sheath where the dust particles are trapped. While the Maxwell distribution may be appropriate for the electrons due to their high thermal velocity, the ions in the plasma sheath are drastically accelerated by the sheath electric field. The isotropy is broken, and it has to be concluded that the OML model is not valid in the plasma sheath.
To remedy this, a new expression for the ion charging current I_i is developed. The complete calculation is presented in the supplemental material of [AM2] alongside a comparison to the OML model, but the most important steps will be elaborated here.
In the following, the z-axis is parallel to the direction of the sheath electric field, so that the x- and y-axis are perpendicular to it. Simulations [148] of low-pressure gas discharges comparable to the *StickingCube* experiment indicate that the ion velocity components perpendicular to the sheath electric field $\vec{E}$ (x and y direction) are distributed according to a normal (Gaussian) distribution (as in the OML model), while the component parallel to $\vec{E}$ (z direction) follows a half-normal distribution, agreeing with the constant-collision-cross-section model formulated by Lampe et al. [149]. These distribution functions are visualized in Fig. 4.1 (a) and (b). The distribution $f_\mathrm{z}(v_\mathrm{z})$ of the z component v_z of the ion velocity introduces a new parameter, the drift velocity

$$v_\mathrm{drift} = \sqrt{\frac{2e|\vec{E}|}{\pi m_\mathrm{i} n_\mathrm{n} \bar{\sigma}}}, \tag{4.10}$$

which depends on the electric field $\vec{E}$, the neutral gas density n_n, and the namesake constant collision cross-section $\bar{\sigma}$, and determines the width of f_z. The distributions $f_\mathrm{x}(v_\mathrm{x})$ and $f_\mathrm{y}(v_\mathrm{y})$ are parametrized by an effective temperature $T_{\mathrm{i},\perp}$. For the anisotropic model using the constant-σ ion distribution, two parameters are needed: The ratio between electron temperature and effective ion temperature perpendicular to the electric field, $\bar{\tau} = T_\mathrm{e}/T_{\mathrm{i},\perp}$, and the parameter $\beta = 2k_\mathrm{B}T_{\mathrm{i},\perp}/(\pi m_\mathrm{i} v_\mathrm{drift}^2)$, which relates the kinetic energy of the ion motion parallel to the electric field to their mean thermal energy in the perpendicular directions. In the case of the OML model, the effect of electron and ion velocity distributions was described by the single parameter $\tau = T_\mathrm{e}/T_\mathrm{i}$.

In the next step, the distribution function $f_\mathrm{i}(v_\mathrm{i})$ for the absolute value $v_\mathrm{i} = |\vec{v_\mathrm{i}}|$ of the ion velocity is found by integrating over the distribution functions of the individual ion

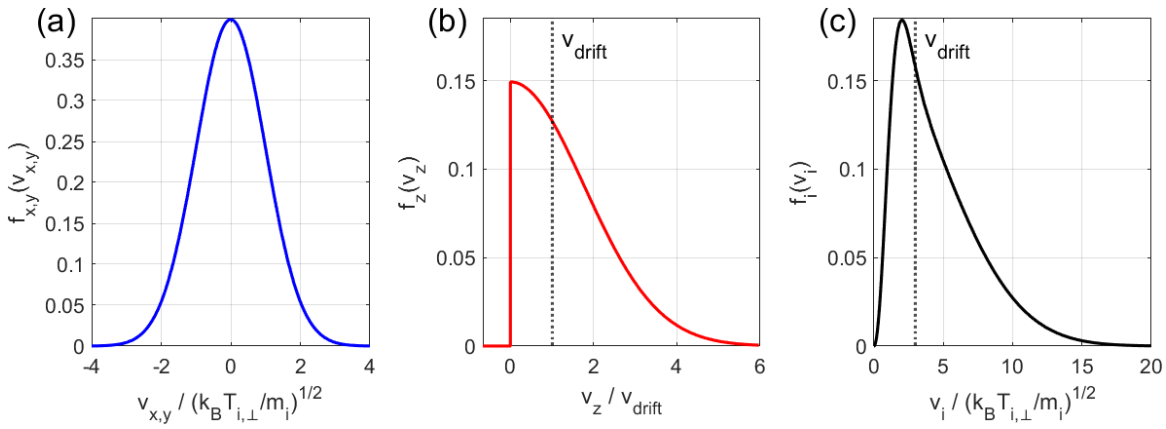

Figure 4.1: Visualization and comparison of the different distribution functions for the ion velocity. (a) Maxwell distribution $f_{\mathrm{x,y}}(v_{\mathrm{x,y}})$ of the x and y component of the ion velocity, perpendicular to $\vec{E}$. The same distribution applies for the y direction. The velocities are normalized to the standard deviation $\sqrt{k_{\mathrm{B}}T_{\mathrm{i},\perp}/m_{\mathrm{i}}}$ of the Gaussian. (b) Distribution $f_{\mathrm{z}}(v_{\mathrm{z}})$ of the z component of the ion velocity, parallel to $\vec{E}$. The velocity axis is given in units of the characteristic drift velocity v_{drift} in the constant-σ model [149]. (c) Distribution function $f_{\mathrm{i}}(v_{\mathrm{i}})$ for the absolute value v_{i} of the ion velocity computed via Eq. 4.11 using a typical value of $\beta = 0.035$, which corresponds to $v_{\mathrm{drift}} \approx 3\sqrt{k_{\mathrm{B}}T_{\mathrm{i},\perp}/m_{\mathrm{i}}}$. The velocity axis is the same as in (a), with v_{drift} indicated as a reference.

velocity components.

$$f_{\mathrm{i}}(v_{\mathrm{i}}) = \int_{\mathbb{R}^3} \delta\left(v_{\mathrm{i}} - \sqrt{v_{\mathrm{x}}^2 + v_{\mathrm{y}}^2 + v_{\mathrm{z}}^2}\right) f_{\mathrm{x}}(v_{\mathrm{x}}) f_{\mathrm{y}}(v_{\mathrm{y}}) f_{\mathrm{z}}(v_{\mathrm{z}})\, d^3\vec{v}. \tag{4.11}$$

Solving this integral in spherical coordinates yields the following expression for the ion velocity distribution $f_{\mathrm{i}}(v_{\mathrm{i}})$:

$$f_{\mathrm{i}}(v_{\mathrm{i}}) = \frac{4A\sqrt{B}}{\sqrt{\pi}\sqrt{A-B}} \cdot v_{\mathrm{i}} \cdot e^{-Bv_{\mathrm{i}}^2} \cdot D_+\left(\sqrt{A-B} \cdot v_{\mathrm{i}}\right), \tag{4.12}$$

with $A = m_{\mathrm{i}}/(2k_{\mathrm{B}}T_{\mathrm{i},\perp})$, $B = (\pi v_{\mathrm{drift}}^2)^{-1}$, and D_+ is the *Dawson* function [150].
This distribution function is plotted in Fig. 4.1 (c). The calculation of the ion current is done with f_{i} from Eq. 4.11 in place of the Maxwellian distribution used in the OML model. The result is an ion current that generally depends on the parameters β and $T_{\mathrm{i},\perp}$ in addition to the ion mass and density.
In the final step, this ion current, alongside the OML electron current, is inserted in Eq. 4.6, which becomes

$$\tilde{s} = \frac{e^x}{\varepsilon\sqrt{\mu\bar{\tau}}}\left[J_1(\beta) + J_2(\beta)\bar{\tau}x\right], \tag{4.13}$$

where $J_1(\beta)$ and $J_2(\beta)$ are integral expressions given in [AM4]. $J_1(\beta)$ and $J_2(\beta)$ are numerically calculated over a range of plausible values (10^{-2} to 10^{-1}) for β. In addition to β, Eq. 4.13 is parametrized by the density ratio ε introduced in Eq. 4.9, and the ratio

$\bar{\tau} = T_\mathrm{e}/T_{\mathrm{i},\perp}$.
With the formula given in Eq. 4.13, the sticking coefficient $\tilde{s}$ of the material of interest can now be calculated from the reduced floating potential of the particle, and the parameters $\varepsilon(h)$, $\bar{\tau}(h)$ and $\beta(h)$. To make a direct connection between floating potential and sticking coefficient, the latter three quantities need to be known.

4.3.2 PIC simulation

In order to have spatially resolved values for $\varepsilon(h)$, $\bar{\tau}(h)$ and $\beta(h)$ available, the PIC simulation code XPDP1 [151–153] was used. The built-in Monte-Carlo collision model was modified to use the ion collision cross sections given by Phelps [154] in place of the original ones.
The principle of PIC simulations was first formulated by Harlow et al. in 1955 [155], and a few yers later applied to plasmas [156]. The advantage of PIC codes for plasma simulations lies in their ability to consider the high number of plasma particles by combining them into a much lower number of *superparticles*, which are allowed to move continuously in the phase space. The number of real particles making up a super particle is allowed to fluctuate. Quantities like electromagnetic fields, on the other hand, are considered on a discretized grid. Collisions within the system are often considered using a Monte-Carlo approach. This overall straightforward principle has made PIC simulations a successful and widely used computational tool in plasma physics.
As an *1d3v* code, XPDP1 considers only one discretized spatial dimension for the coordinates of superparticles, but three dimensions for their velocities. The simulated system is therefore similar to an infinitely expanded parallel-plate reactor, which is a suitable analogon for a real-world parallel-plate discharge. As a single micrometer-sized dust particle like in the experiment presents no significant influence on the discharge as a whole, the dust particles are neglected in the simulation. After running the simulation until it equilibrates at a constant number of superparticles, it is advanced for enough time to cover one rf period (approx. $73.7\,\mathrm{ns}$). For each timestep during the rf period, data for electron and ion positions and velocities are recorded. The local electric field strength for each grid cell is also stored. The densities $n_\mathrm{e}(h)$ and $n_\mathrm{i}(h)$ are calculated for each timestep from the electron and ion positions, respectively, and then averaged over the rf cycle to yield spatial profiles. $T_\mathrm{e}(h)$ is obtained from the distribution of the electron velocities, and $T_{\mathrm{i},\perp}(h)$ is obtained from the distribution of the ion velocity components in x and y direction. $\varepsilon(h)$ and $\bar{\tau}(h)$ are calculated from these results. The drift velocity v_drift appears in the half-normal distribution that describes the distribution of the z component of the ion velocity, and can be obtained for example from the distribution's FWHM (*full width at half maximum*):

$$f_\mathrm{z}(v_\mathrm{z}) \propto \Theta(v_\mathrm{z}) \exp\left(-\frac{v_\mathrm{z}^2}{\pi v_\mathrm{drift}^2}\right), \tag{4.14}$$

where Θ denotes the Heaviside step function. According to the constant-σ model by Lampe et al. [149], v_drift is related to the constant collision cross-section $\bar{\sigma}$ via

$$v_\mathrm{drift}^2 = \frac{2e|\vec{E}|}{\pi m_\mathrm{i} n_\mathrm{n} \bar{\sigma}}, \tag{4.15}$$

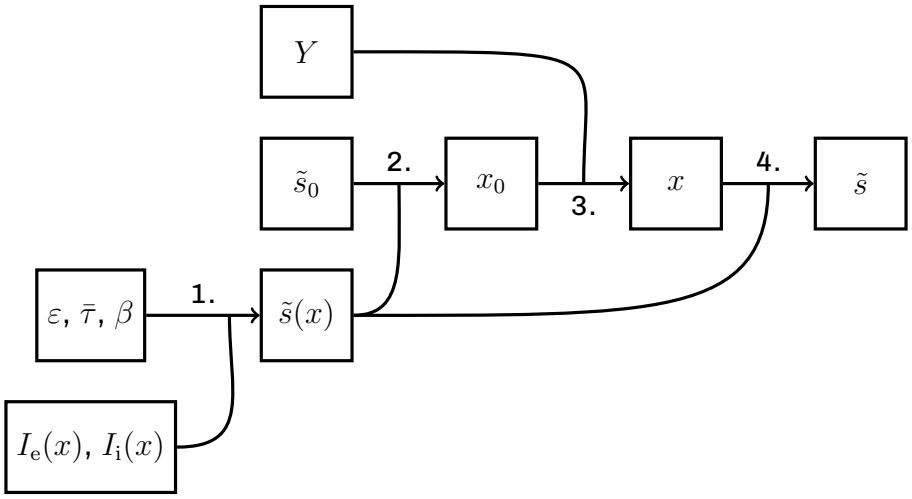

Figure 4.2: Schematic illustration of the evaluation process. The numbers correspond to the steps enumerated in the text. The following quantities and relations are shown: The experimentally determined floating potential ratio Y between the particle of interest and the interpolated reference particle, the sticking coefficients $\tilde{s}_0$ and $\tilde{s}$ of the reference particle and the particle of interest, respectively, the reduced floating potentials x_0 and x of the reference particle and the particle of interest, respectively, the parameters ε, $\bar{\tau}$ and β obtained from the PIC simulation, the expressions $I_\mathrm{e}(x)$ and $I_\mathrm{i}(x)$ for the charging currents in dependence of the reduced floating potential, and the relation $\tilde{s}(x)$ between sticking coefficient and reduced floating potential.

where n_n is the neutral gas density, which is calculated from the neutral gas temperature T_n (about room temperature, ca. $300\,\mathrm{K}$) and the measured pressure p in the reactor approximating argon as an ideal gas. The original value $\bar{\sigma} = 6 \times 10^{-19}\,\mathrm{m}^2$ given by Lampe et al. agrees very well with the results of the simulation for the z component of the ion velocities and the electric field. The parameter $\beta(h)$ is therefore calculated from the electric field $|\vec{E}|(h)$ using $\bar{\sigma}$ and the values for $T_{\mathrm{i},\perp}(h)$. Using the results of the simulation, the determination of the sticking coefficients is now possible.

In conclusion, the aspects needed for the determination of the sticking coefficient from the measured floating potential ratio have been elaborated. To recapitulate the evaluation scheme, the sequence of the evaluation is illustrated in Fig. 4.2, which is as follows:

1. Using the parameters ε, $\bar{\tau}$ and β obtained from the simulation, and the models for the charging currents $I_\mathrm{e}(x)$ and $I_\mathrm{i}(x)$, the relation $\tilde{s}(x)$ between sticking coefficient and reduced floating potential x is found.

2. Using $\tilde{s}(x)$ and the literature value $\tilde{s}_0$ for the sticking coefficient of the reference material, the reduced floating potential x_0 of the reference particle is obtained.

3. The reduced floating potential x of the particle made of the material of interest is found using x_0 and the experimentally obtained floating potential ratio Y (see Eq. 4.7).

4. The sticking coefficient $\tilde{s}$ of the material of interest is finally found using the reduced

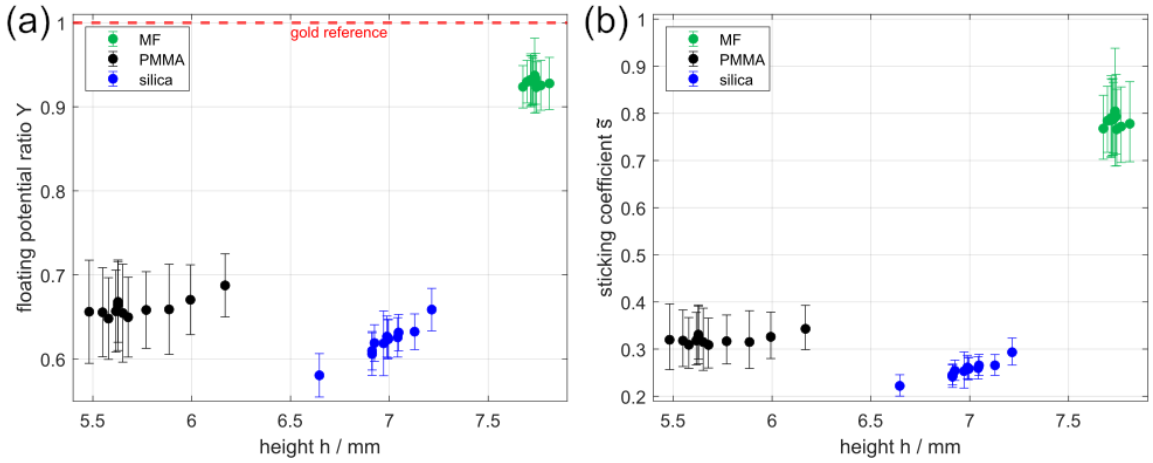

Figure 4.3: (a) Experimental results for the floating potential ratio relative to the gold reference curve, for spherical particles made of MF (green), PMMA (black), and SiO_2 (blue), plotted over the respective levitation height of the particle. The gold reference lies at 1 and is marked by a dashed red line. (b) Results for the averaged electron sticking coefficient $\tilde{s}$ of MF, PMMA and SiO_2. *Reproduced from I. König et al., Phys. Plasmas* ***32****, 024501 (2025)* [AM3] *with the permission of AIP Publishing.*

floating potential x of the material of interest, and the expression for $\tilde{s}(x)$ found in step 1.

4.4 Results for SiO_2

Using the measurement and evaluation scheme described above (see Fig. 4.2), the averaged electron sticking coefficient $\tilde{s}_{SiO_2}$ of SiO_2 was determined. The resulting values were reproducible within the uncertainty margin for particles roughly at the same height h. Even with the improved model for the ion current, it is still apparent that the resulting $\tilde{s}_{SiO_2}$ slightly increases with the levitation height h. This is attributed to the variation of T_e with h due to the varying conditions in the plasma sheath, which in turn changes the energy distribution of the electrons impinging on the particle surface. The majority of values for $\tilde{s}_{SiO_2}$ lie in the interval 0.18 to 0.34 with a mean uncertainty of ± 0.07, significantly below 1 and also below the theoretical prediction of ca. 0.66 [1]. The difference in the electron sticking coefficient between silica and gold is therefore even more pronounced than the difference in floating potential. The floating potential ratio Y between silica and gold is the first experimental proof of a charging difference between conductive and dielectric materials in dusty plasmas, which could not be resolved in earlier investigations [157]. Moreover, the resulting sticking coefficients confirm the effect predicted by Bronold et al. [1].

4.5 Measurements for additional materials

Additional measurements in the StickingCube II chamber were conducted with PMMA and MF particles, and silica particles as a comparison to the experiments in StickingCube I mentioned in Section 4.4, following the same exact scheme. The results are presented in Fig. 4.3. The values for SiO_2 lie roughly between 0.22 and 0.3 with an average uncertainty of ± 0.03, agreeing well with the previously presented results. As before, they are exhibiting a slight increase with h. Interestingly, the results for the polymers appear to be approximately constant in the respective range of levitation heights. The average values for the polymers are $\tilde{s}_{\mathrm{PMMA}} = 0.32 \pm 0.06$ and $\tilde{s}_{\mathrm{MF}} = 0.78 \pm 0.08$. The result for PMMA agrees quite well with the expectations set by the extrapolation of experimentally obtained SEE yields made by Dapor et al. [158] using the Lin & Joy law [159]. For $E \approx 5$ to $10\,\mathrm{eV}$, a SEE yield $\delta \approx 0.6$ is estimated, which would correspond to a sticking coefficient of about 0.4, close to the result obtained here.
In contrast to materials like SiO_2, MgO and Al_2O_3, no similar theoretical predictions for the sticking coefficient of MF or PMMA exist, as their electronic structure is not sufficiently understood. Despite this, the vast majority of laboratory dusty plasma experiments employing microparticles has so far been conducted with particles made of either of the two polymers. Therefore, knowledge of the sticking coefficients of these materials promises new insights, as the electron sticking coefficient of these materials was usually assumed to be 1. A more in-depth discussion of the possible impact of these results on dusty plasma research, for example on studies of binary dusty plasmas or Janus particles, is given in Chapter 6.

4.6 Possible limitations of the method

It should be noted that conditions exist where additional considerations are needed to reliably determine electron sticking coefficients.
One such situation arises when the dust particles in question have very high friction coefficients, for example at higher pressures. In that case, the determination of γ using PEOM or PRRM can become much less accurate due to the limited sampling rate available with the camera.
The influence of the ion drag force is another potential source of errors. For spherical particles with radii in the micrometer range, the ion drag force can usually be estimated as negligible using the models of Hutchinson and Khrapak, which are discussed in the textbook by Melzer [55]. However, the ion drag force becomes more influential for smaller particles. If the ion drag force becomes non-negligible, it influences the force balance of the trapped particle. As a consequence, a portion of the restoring force resulting in the driven oscillations would be due to the ion drag instead of the electric field. The measured eigenfrequency ω_0 is then also dependent on the ion drag, introducing a systematic error for the floating potential estimation that scales with the particle size. This implies that the comparison between particles with large size disparities, or large differences in how much they are affected by the ion drag, may introduce a systematic error to the method.

Moreover, it is still an open question how exactly the impinging ions interact with the particle surface, apart from changing the particle charge by a positive elementary charge. If the ion-surface interaction entails the recombination with an electron from the particle surface, it is unclear where the released energy of about $16\,\mathrm{eV}$ per ion (for argon) is deposited. Previous investigations show a heating of dust particles to temperatures of 300 to $500\,\mathrm{K}$, which is attributed to recombination at the surface [160–162]. In the case of a temperature-dependence of the electron sticking coefficient this needs to be considered.
Moreover, it has been postulated that ions may be bound in orbit states close to the surface [163–166]. As this has not been experimentally verified, an influence of this effect on the Sticking Machine is unlikely but possible. In this case, it could then be necessary to include an (effective) *ion* sticking coefficient into the evaluation, complicating the matter.
Despite these limitations, the Sticking Machine promises to be a suitable setup for the determination of electron sticking coefficients. This is mainly due to the relative measurement scheme: if a previously unconsidered effect affects the measurements of the auxiliary quantity η for both compared materials to the same extent, it cancels out in the ratio between the η values of the two materials. Thus, the measurement scheme is quite robust with respect to additional, minor effects.

5 Extending the method to non-spherical particles

This chapter presents the results of the publication in Ref. [AM4]*, and provides additional context on how to extend the measurement scheme presented in Chapter* 4 *to non-spherical particles.*

The measurement scheme established in Chapter 4 is capable of measuring the averaged low-energy electron sticking coefficients of materials available as spherical microparticles. However, many materials of technological interest are crystalline, such as Al_2O_3 (sapphire), MgO or ZnO, which is why grains made of these materials are not perfectly spherical. In order to extend the measurement scheme to non-spherical particles and therefore a wider array of technologically relevant materials, the models for spherical particles need to be generalized to non-spherical geometries. Three points are central to this generalization:

1. It has to be assessed how to assign a floating potential to a non-spherical particle.
2. A relation between the particle charge and floating potential is needed. This ultimately comes down to generalizing the spherical capacitor model to non-spherical particle geometries.
3. The non-spherical geometry can lead to additional effects altering the measured sticking coefficient.

These three points shall be discussed in the following sections, respectively. The focus of the investigations of the contribution [AM4] is the second point.

5.1 Floating potential of non-spherical particles

The simplest situation in a dusty plasma is a single, spherical particle embedded in a perfectly isotropic plasma. For example, the OML model [93] for the particle charging considers such a situation. Due to the perfect spherical symmetry of the system, the electric potential at the particle surface has to be uniform [78], bar some minimal statistic fluctuations [167]. In such a case, it is justified to call the spatially constant value of the surface potential the floating potential Φ_f. The usefulness of the floating potential lies in the fact that it is, in contrast to the total charge q of the particle, independent from the particle size, which is one of the main results of the OML theory. This fact is the basis for the reference curve used in Chapter 3.
However, one can think of several situations where the symmetry is broken, and the surface potential does not necessarily have to be uniform on the particle surface.
For one, particles in laboratory dusty plasma systems are often confined in the lower

plasma sheath, in which a strong electric field accelerates ions towards the lower electrode. This directed ion motion was already subject of considerations regarding the total charging current (see Section 4.3.1). In a more detailed picture, this leads to a more intensive ion flux towards the upper side of the particle, and an attenuated ion flux towards the lower side. For particles with a sufficiently high surface conductivity, the charge carriers at the surface are able to continuously redistribute themselves to form an equipotential surface. This is due to the conductive surface being a Faraday cage, and also holds for non-spherical particles with conductive surfaces. In contrast, an ideally non-conductive particle surface is fundamentally different, as it is not able to redistribute the charge carriers on it. Consequentially, incoming charges are assumed to stay at the point of impact. It has been discussed that this could lead to a spinning motion of insulating particles in electric fields [168], such as the sheath electric field, or magnetic fields [169, 170]. This would lead to a potentially much more homogeneous surface potential by compensating the charging asymmetry. To my best knowledge, there are however no reported observations of such a spinning particle motion of single, spherical dust particles. This is intuitive, because microparticles are usually detected as a bright spot of reflected laser light captured by a video camera. The lack of spatial resolution does not permit the observation of a rotation of the uniformly looking particle surface. In the experiments done with non-spherical particles, only a rotation around the vertical axis could be observed [171], agreeing with the observations made within the experiments conducted for this work and hinting at the absence of the spin instability. Investigations of the stability of the alignment of rod-like particles in the plasma sheath have also not shown such an effect [172–177].
Computational investigations furthermore indicated that inhomogeneous potential structures can form on the surface of elongated insulating dust particles larger than the electron Debye length λ_{De} in ion flows, due to the ion wake [178, 179].
On the other hand, certain areas of the surface of concave particles can be partially shadowed from the incoming electron and ion fluxes. This effect can also lead to inhomogeneous surface potentials on dielectric surfaces in anisotropic plasma environments, and is considered by simulation techniques such as *OML_LOS* (*orbital motion limited - line-of-sight approximation*) [180].
In general, the available literature offers no clear indication on whether the surface of insulating dust particles is an equipotential surface. On the contrary, the principle of the Faraday cage implies that all conducting particle surfaces are equipotential surfaces, justifying the use of the uniform surface potential value as the floating potential.

However, the context of the Sticking Machine allows for some simplifications. First of all, all particles investigated in this project had dimensions in the range of about 5 to $50\,\mu\mathrm{m}$, significantly below typical electron Debye lengths (ca. $500\,\mu\mathrm{m}$ to a few millimeters). The effects of the ion wake on the surface potential should therefore be negligible. Secondly, and most importantly, only the total charge on the particle is measured via PRRM or PEOM (see Chapter 2), and is available in the evaluation. Dipole- or higher moments of the multipole expansion of the surface charge distribution do not change the total charge of the particle, even though they can lead to a torque [182]. The electric potential distribution in the space around the particle is furthermore extremely well approximated by the potential distribution around a point charge carrying the total charge

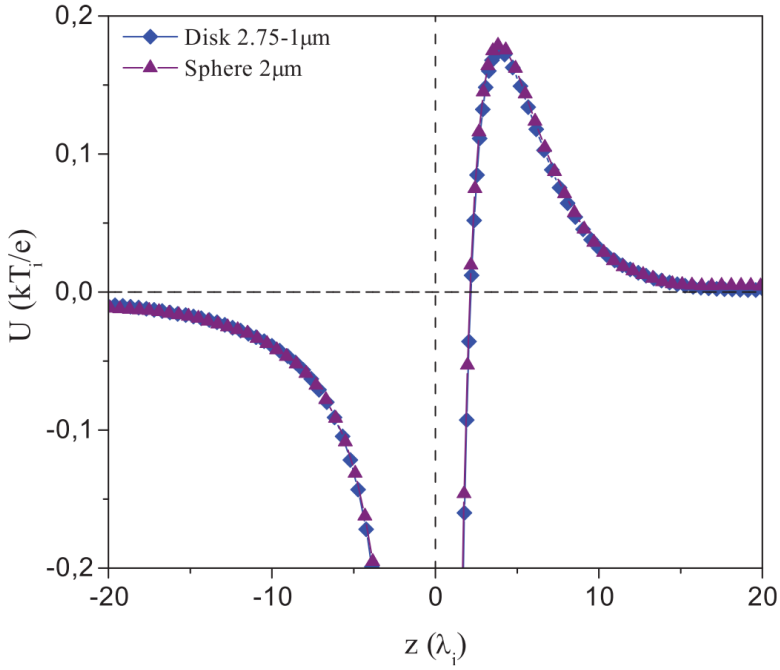

Figure 5.1: Comparison between the potential (denoted U) around two particles with equal capacities, in dependence of the vertical coordinate z. z is given in units of the ion Debye length, and the z-Axis is parallel to the direction of the external electric field. The blue diamond markers correspond to a disk with radius $2.75\,\mu\mathrm{m}$ and a thickness of $2\,\mu\mathrm{m}$, while the purple triangle markers correspond to a sphere with radius $2\,\mu\mathrm{m}$. The shape of the potential does not differ between the differently shaped particles. *Reproduced from: G. I. Sukhinin et al., Contrib. Plasma Phys.* ***59*** *(2019), 201800153* [181]. *©John Wiley and Sons. Reproduced with permission. All rights reserved.*

(monopole approximation) [182, 183]. An effective floating potential $\Phi_{\mathrm{f,eff}}$ can therefore be assigned to a dielectric particle using the capacitance C of the particle geometry:

$$q = C\Phi_{\mathrm{f,eff}} \Leftrightarrow \Phi_{\mathrm{f,eff}} = \frac{q}{C}. \tag{5.1}$$

Numerical simulations show that non-spherical particles with the same capacitance also show the same potential distribution in the space further than an ion Debye length from the particle center [181, 184] (see also Fig. 5.1). In terms of electrostatics sufficiently far away, a particle with potentially inhomogeneous surface potential is therefore equivalent to a particle with uniform surface potential $\Phi_{\mathrm{f,eff}}$ with the same charge and capacitance.

In the following, the term "floating potential" refers to the actual floating potential for conductive surfaces, as well as the effective floating potential $\Phi_{\mathrm{f,eff}}$ for any particle with a potentially non-homogeneous surface potential, i.e. dielectric particles. It should be mentioned that this is also implied for the spherical dielectric particles in Chs. 3 and 4.

5.2 Generalization of the capacitor model

In the context of particle charging of dust particles in plasmas, the floating potential Φ_f of the particle arises from the balance of the charging currents. To access the charge q, which is the parameter accessible in the experiment and governing the dynamics of the dust, a relation between q and Φ_f is needed. Traditionally, this is done using the capacitor model [54, 55, 94], treating the particle as a spherical capacitor. For spherical particles, the expression for the capacitance only depends on the particle radius a (compare Eq. 4.1).

$$q = C\Phi_\mathrm{f} = 4\pi\varepsilon_0 a \Phi_\mathrm{f}. \tag{5.2}$$

For investigations using spherical particles, the capacitor model is widely used and generally accepted as the truth, despite the approximation of the surrounding plasma as a vacuum.
A similar relation $q = C\Phi_\mathrm{f}$ should also be valid for non-spherical particles, given that their capacitance is known. To enable a consistent treatment of spherical and non-spherical particles in the Sticking Machine measurement scheme, it is desirable to reduce each non-spherical geometry to an equivalent sphere with the same capacitance. That way, Eq. 5.2 holds also for non-spherical particles when using the radius $R_\mathrm{C} = C/(4\pi\varepsilon_0)$ in place of a. Thus the floating potential can be accessed using the measured charge and the capacitance derived from the particle's shape.
In practice, however, the calculation of the capacitance is not trivial. Analytical expressions exist only for simple shapes like cylindrical discs and rods [185], ellipsoids [186], and sphere doublets [187]. Numerical calculations are possible for moderately complex structures, but can become computationally expensive for more intricate shapes. Also, this is only possible if the full 3D structure of the particle is known. In experiments, usually only a finite number of 2D images of the particle is available. The particle shape then has to be reconstructed from these, which does not necessarily produce unambiguous or sufficiently detailed 3D structure information and is also potentially computationally expensive. Moreover, repeated measurements, as intended for the Sticking Machine in the long term, would require the reconstruction for every single particle, as their shape is expected to differ among each other.

In order to remedy this, it is advantageous to use purely geometrical approximations for R_C. Two such approximation models have been compared to the true capacitance in this work, the *smallest enclosing sphere* model (SES) suggested by Asnaz et al. [112], and the *orientation-averaged equivalent sphere* model (OAES) first applied to dusty plasmas by Matthews et al. [183]. Their advantage lies in the comparatively easy computation of the respective characteristic radius used to approximate R_C. Until today, the discussion which model describes the charge of non-spherical dust particles best is not concluded, which is a question this work aims to answer for the situation in the plasma sheath.

5.2.1 Geometrical approximation models for the capacitance

In the following, a short characterization of the SES and OAES models chall be given.
The SES model states that the charge of a non-spherical particle scales with its maxi-

mum extent, which is given by the radius R_E of the smallest enclosing sphere. Mathematically, the smallest enclosing sphere is the *minimum bounding sphere* of all surface points of the particle. Finding the minimum bounding sphere of a set of points in an arbitrary number of dimensions is a common problem appearing for example in computer graphics, statistics and operations research. Due to this, a number of algorithms able to obtain the minimum bounding sphere, or approximate it, have already been developed. These can be readily applied to the non-spherical particle geometry and offer an efficient way to obtain R_E. If the SES model is valid, R_C can be approximated by R_E.
The OAES model, on the other hand, states that the particle charge scales with the projected area of the particle. The projected area generally varies depending on the orientation of the projection plane with respect to the particle. Therefore, the mean projected area PA, obtained from the average over all projection plane orientations, is used. PA can be numerically calculated using the algorithm provided by Gopalakrishnan et al. [188]. According to the OAES model, R_C is approximated by the radius

$$R_\sigma = \sqrt{\frac{PA}{\pi}} \tag{5.3}$$

of a circle with area PA.

5.2.2 Experiments and simulation for sphere aggregates

For this study, monodisperse, non-intersecting sphere aggregates are chosen as an easy to model non-spherical particle class. Sphere aggregates consist of a number N of spherical monomers forming one coherent structure. In contrast to polydisperse sphere aggregates, the monomers of monodisperse aggregates all have the same radius a_m. Furthermore, in all aggregates considered here, there were no significant intersections between monomers, which justifies the assumption that connected monomers are tangent to each other (*non-intersecting aggregates*). In general, a sphere aggregate with N monomers can be fully defined by N position vectors $\vec{c}_i$ and N monomer radii a_i ($1 \leq i \leq N$). Monodisperse aggregates are characterized by only one radius a_m for all monomers.
Sphere aggregates are often employed to describe agglomeration processes of spherical monomers, for example in process plasmas [189] or astrophysical situations, primarily protoplanetary discs [180, 183, 190–194]. They can furthermore be used to model the fractal-like behavior of granular matter systems [195], and intersecting aggregates allow for the approximation of many other non-spherical geometries [196].
Regarding the computation of R_E and R_σ, monodisperse sphere aggregates massively simplify the calculations. R_E can simply be obtained from the minimal bounding sphere of all monomer centers (instead of all surface points) plus the monomer radius. For the calculation of R_σ, only the monomer centers need to be projected to a plane for each orientation, also saving computation time. The calculation of the true capacitance, and hence R_C, is done using the numerical *finite element* method. R_C, R_E and R_σ are computed for each aggregate observed in the experiment or used in the simulation, as well as a set of aggregates generated to cover a variety of possible structures (see below).

The investigations on non-spherical particles done in the framework of this project can be divided into three parts:

- Firstly, the radius a_{eq} of a spherical particle with the same charge is experimentally determined for aggregates of 2-4 gold-coated microspheres levitated in the plasma sheath. This radius is compared to R_{C}, R_{E} and R_{σ}.

- Secondly, simulations using the OML_LOS scheme [180] were used to calculate the charge on perfectly dielectric aggregates of 13-27 monomers in the plasma bulk. The radius a_{eq} of an equivalently charged sphere is also obtained for these aggregates and compared to R_{C}, R_{E} and R_{σ}.

- Lastly, the approximation of R_{C} by R_{σ} is improved by formulating an empirical correction formula for monodisperse sphere aggregates using the available data for R_{C} and R_{σ}.

In the experimental studies, aggregates of 2-4 gold-coated microspheres were observed. These had already occasionally occurred during the recording of the reference curve for $\eta(h)$ (cf. Chapter 4). Their rate of appearance was sufficient to obtain a total of 17 doublets, 8 triplets and 6 quadruplets. To obtain the radius a_{eq} of a virtual, spherical conductive particle with the same charge as an aggregate, a relative measurement scheme related to the one presented in Chapter 4 was used. Again, a reference curve for the quantity $\eta(h) = \Phi_{\mathrm{f}}(h)\rho_{\mathrm{q}}(h)$ was recorded using gold-coated spherical particles of different sizes. A related auxiliary quantity $\kappa \propto q_{\mathrm{ns}}\rho_{\mathrm{q}}(h)$ was calculated for each aggregate using its eigenfrequency ω_0 and mass m, where q_{ns} is the charge of the non-spherical aggregate.
ω_0 was measured using the PEOM. In contrast to spherical particles, the mass density could not be obtained from the damping rate γ, as the simple Epstein friction model is only applicable for spheres [107] or cylinders [112, 197]. To avoid extensive computational effort in order to solve the momentum balance on the aggregate surface, the mass density of single spherical particles with the same nominal radius as the aggregate monomers was instead used. These mass densities differed between nominal sizes, as the coating thickness also varied between them. The measurements done for the reference curve $\eta(h)$ provided the damping rates γ and the radii a necessary to compute the average mass densities for each nominal radius, which in turn allowed to determine the aggregate masses. It was assumed that all experimentally observed aggregates are approximately monodisperse because their monomers all had the same nominal radius.
Three considerations now allow for the determination of a_{eq}:

- The capacitor model for spherical particles is valid, i.e. $q = 4\pi\varepsilon_0 a\Phi_{\mathrm{f}}$,

- the (effective) floating potential for particles of the same surface material (i.e. the same electron sticking coefficient $\tilde{s}$) should be the same irrespective of size or shape,

- and the charge density $\rho_{\mathrm{q}}(h)$ cancels out of the fraction $\kappa/\eta(h)$ when h is the levitation height of the aggregate.

Using this relative measurement scheme, a_{eq} is determined for all experimentally observed aggregates, and compared to the characteristic radii predicted for the respective aggregate structure. To simplify the comparison, a_{eq}, R_{C}, R_{E} and R_{σ} are normalized to the monomer radius a_{m}. An equally excellent agreement with the true capacitance, as well as the OAES model is found. The predictions of the SES model, however, are significantly outside the uncertainty limits.

The approach using the simulated data is very similar. OML_LOS simulations [180] of 108 monodisperse aggregates with 13-27 monomers were conducted, yielding their individual total charges. The simulated situation differed slightly from the experimental one: Firstly, the aggregates in the simulation were situated in an isotropic plasma akin to the laboratory plasma bulk, justifying the use of an OML charging approach. Secondly, the impinging charges (electrons, or holes created by recombination of ions with electrons at the surface) were assumed to stay at their point of arrival, mimicking a perfectly insulating particle. The floating potential of these grains was then computed from the electron and ion temperatures and densities imposed by the simulation. Again using the spherical capacitor model, the radius a_{eq} of an equally charged spherical grain was determined for each simulated aggregate. The findings were then normalized to a_{m} for the comparison with R_{C}, R_{E} and R_{σ}. As with the experimental data, an excellent agreement with the capacitance is found, and the SES predictions do not agree with a_{eq}. The capacitance generally appears to be the best description irrespective of the monomer count, the charging conditions or the conductivity of the particle surface material. Interestingly, the OAES prediction is now ca. 10% below the capacitance and a_{eq}. It has to be assumed that the OAES model approximates grains with only a few monomers very well, but gets more inaccurate with higher values of N.

Motivated by this observation, a large study comparing the capacitance and the OAES model is conducted. It utilizes the calculations done for the experimentally observed aggregates as well as those from the OML_LOS simulations. Additionally, the results of calculations for a number of simple structures, as well as a multitude of randomly generated monodisperse aggregates are considered in order to cover the largest variety of structures possible. All these structures can be characterized two parameters, the monomer count N, and the compactness factor Φ_{σ}. Φ_{σ} was defined by Paszun et al. [190] and describes to what extent the volume of a particle fills the sphere with the radius R_{σ} given by the OAES model. By fitting a model function to the deviation of R_{σ} from R_{C} in dependence of N and Φ_{σ}, an empirical correction factor $F(\Phi_{\sigma}, N)$ is found. Using F, even the capacitance of aggregates with a very low compactness (ca. 0.19) can be approximated with the corrected OAES model within 5% accuracy.

These findings lead to the conclusion that the capacitance is, unsurprisingly, the best suited expression to describe the relation between dust particle charge and floating potential. Furthermore, it can be approximated by the OAES radius R_{σ} for very compact aggregates ($\Phi_{\sigma} \geq 0.6$), or for less compact, monodisperse aggregates using the empirical correction F.

5.3 Additional effects of non-spherical geometries

When considering non-spherical particles, additional effects can arise from more complex geometries that may need to be considered in the determination of the sticking coefficient $\tilde{s}$. Two such effects will briefly be discussed below.

5.3.1 Re-sticking and possible correction

Re-Sticking is an effect expected for concave particles with a surface with substantial electron emission yield, such as dielectrics. The situation bears similarities to a dust particle on a substrate [198]. When a primary electron hits the particle surface, electron emission (reflection or emission of a true secondary) can occur. On concave surfaces, it is possible for the emitted electron to collide with the particle surface again, even multiple times, each time having a finite chance to stick at the surface. The effective electron sticking coefficient $\tilde{s}_{\mathrm{eff}}$ is therefore higher than the actual electron sticking coefficient $\tilde{s}$ which considers only a single interaction of the incoming electron with the particle surface.
In future measurements of dielectric, concavely shaped particles, this effect has to be accounted for. Theoretical or computational investigations of the number of surface contacts of electrons impinging on a given particle geometry are expected to provide a mathematical connection between the measured effective sticking coefficient $\tilde{s}_{\mathrm{eff}}$, and the actual sticking coefficient $\tilde{s}$ with respect to a single surface contact. However, this would require sufficient knowledge of the 3D geometry of the particle when applying this approach to experimental studies.

5.3.2 Transmission through thin walls

Throughout this work, the investigated dust particles had quite solid structures, meaning that any particle surface element sat on a substantially thick bulk of solid material. In more intricate structures such as *multiscale aeromaterials*, electron transmission is expected to affect the charging behavior.

Multiscale aeromaterials are an exotic type of materials investigated in collaborations between the working groups of F. Greiner and R. Adelung. These highly porous materials consist of an interconnected network of hollow tetrapods [199–203]. While the length of the connections is on the order of micrometers, the thickness of their walls is in the nanometer range, hence the descriptor "multiscale".

A central topic of the aforementioned research collaboration is the interaction between the highly porous aeromaterials and plasmas. First experiments conducted in the framework of the master thesis of K. Hansen [204] have dealt with plasmas ignited in reactors where the space between the electrodes is filled with *aeroglass* (t-SiO_2).
To achieve a better understanding between the plasma electrons and aeromaterials, it would be desirable to investigate chunks of the material levitated in the plasma sheath, preferably similarly sized as the microparticles examined so far. This would enable the use of the powerful methods for the investigation of particle charging developed in this work to examine the charging behavior of aeromaterials. However, preliminary tests

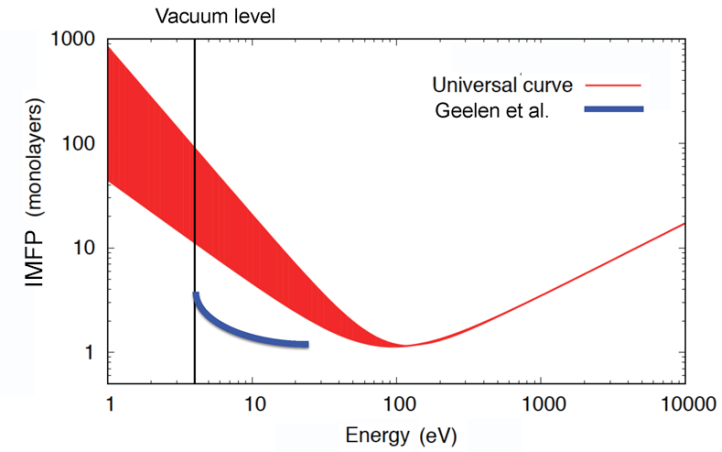

Figure 5.2: Illustration of the electron inelastic mean free path (IMFP, given in monolayers) as a function of the electron energy. The red curve corresponds to the universal curve, while the blue line represents the results for graphene [206]. *Image Credit: W. S. M. Werner/Vienna University of Technology. Reproduced from* [207] *with permission.*

done in the framework of I. König's master thesis [205] show that the very low mass density of these materials leads to the aeromaterial chunks levitating very high in the lower sheath, close to the transition to the plasma bulk. For comparison, a circa $40\,\mu\mathrm{m}$ aeroglass chunk levitated as high as a gold-coated MF particle of $4.13\,\mu\mathrm{m}$ diameter, the smallest size used in the experiments. The high charge-to-mass ratio is additionally indicated by very large values of the eigenfrequency ω_0 measured using PEOM.

While the overall non-spherical structure of an aeromaterial chunk can be described using the models for the equivalent radius presented in Section 5.2 and the considerations on re-sticking given before (see Section 5.3.1), the effect of the nanometer-thin walls needs additional consideration. In contrast to the comparatively massive microparticles, the thin walls in aeromaterials potentially allow for the transmission of electrons, which is expected to lower the effective electron sticking coefficient.
To quantify this effect, the electron *inelastic mean free path* (IMPF) of materials is considered. Simulation codes for the calculation of the closely related stopping power of electrons in different materials exist, but are limited to the enrgy range above a few hundred electronvolt [208, 209]. Historically, the electron IMPF was conjectured to follow a universal, material-independent law [210] only depending on the electron energy, while more recent results strongly hint at a more pronounced material dependence of the electron IMFP [206, 207]. Fig. 5.2 compares the conjectured universal curve to recent results for the electron IMFP in graphene [206], which do not follow the curve. Based on the universal curve, it can be expected that an electron with an energy of $5\,\mathrm{eV}$ is able to transmit through up to 100 monolayers on average. For materials not following the universal curve, this effect has a different extent. Overall, this would imply a substantial transmission probability through aeromaterial chunks of several tens of micrometers in size.
To factor this effect into the evaluation of future measurements on aeromaterial grains,

the expected transmission probability through the grain has to be estimated based on the material making up the aeromaterial, and the grain dimensions. The actual sticking coefficient in this case could then be reconstructed from the measured, effective sticking coefficient with a similar approach as for the re-sticking (see Section 5.3.1).

6 Conclusion

6.1 Results

As stated in the introduction (Chapter 1), the primary goal of this work and the Sticking Machine project was the determination of low-energy electron sticking coefficients using microparticles confined in a plasma. To this end, several steps had to be taken, each yielding results directly finding application in the Sticking Machine, as well as results of interest for a broader field of research.
The first step was the design and benchmarking of the PEOM as a new particle-resonance method that would ultimately be used to measure the charge-to-mass ratio of the particles in the Sticking Machine. Detailed consideration of technical aspects of experiment and analysis, such as the excitation waveform and the influence of the coupling network, made the PEOM a fast, precise and minimally perturbative diagnostic. The precision is on par with the PRRM [80], which is a standard method in dusty plasma experiments due to its precision. Concurring with the requirements of the Sticking Machine, the PEOM is able to operate on single particles regardless of their shape or material, without significantly altering the plasma parameters, and with a time resolution of $1\,\mathrm{s}$ per measurement, which is about 2 orders of magnitude faster than the PRRM. Moreover, it can be used to measure the ohmic plasma resistance, which was effectively inaccessible with the PRRM and classical RM.

In the next step, the relative measurement scheme of the Sticking Machine was developed. With the PEOM and long distance microscopy as primary diagnostics and using an interpolation approach, the floating potential ratio between spherical silica and gold reference particles could be measured. As the potentially height-dependent plasma parameters were eliminated in the evaluation, the floating potential ratio is attributed to the difference of surface material. Using an improved version of the OML charging model attributing for the sheath anisotropy and auxiliary PIC simulations, the low-energy electron sticking coefficient $\tilde{s}_{\mathrm{SiO_2}}$ of silica could be determined to be around 0.24. Although $\tilde{s}_{\mathrm{SiO_2}}$ was expected to be smaller than 1 at the outset of the Sticking Machine project based on theoretical calculations for crystalline silica [1], this was (to my best knowledge) the first time this charging difference in the dusty plasma context was measured. The implications for plasma physics are numerous, and are discussed in detail in Section 6.3.

With this new technique at hand, measuring the sticking coefficients of other materials available as microspheres promised to be a worthwhile task. The majority of dusty plasma experiments have been conducted with spherical MF or PMMA polymer particles, motivating investigations of these materials' sticking coefficients. Measurements in an improved experimental setup confirmed the results for silica obtained before,

and yielded the sticking coefficients of MF and PMMA. PMMA shows a low sticking coefficient of $\tilde{s}_{\mathrm{PMMA}} = 0.32 \pm 0.06$ at the respective energies. Interestingly, the sticking coefficient of MF, $\tilde{s}_{\mathrm{MF}} = 0.78 \pm 0.08$, is much higher than that of PMMA, even though they are both polymers and therefore expected to be dielectric.
As of now, the electronic structures of polymers like MF and PMMA are not understood sufficiently enough to theoretically estimate their sticking coefficients as done with SiO_2, MgO and Al_2O_3 [1]. The results for MF and PMMA, as well as future results for other polymers, offer experimentally determined values that can be used to benchmark future theoretical studies.

The last step taken in this work was the validation of the capacitor model for non-spherical particles, and investigating which of the approximation models proposed in the literature are suitable. A combined study using experimental results as well as simulations considering sphere aggregates was conducted, confirming the validity of the capacitor model for non-spherical particles, regardless of their charging conditions. Of the approximations, only the OAES model is a suitable approximation for smaller aggregates. Using the empirically obtained correction factor, it can however also be applied to larger aggregates. With regard to the Sticking Machine, these results enable the application of the scheme developed for spherical particles to non-spherical particles, given the particle geometry can be reconstructed. The OAES approximation, however, can also be calculated when the exact particle geometry is not known. This is expected to significantly simplify the consideration of the particle shape in future measurements on non-spherical particles.

6.2 Perspectives for the Sticking Machine

Based on the foundation laid by this work, the Sticking Machine is already operational for materials available as spherical particles for a fixed mean energy. To further test and extend the functionality of the Sticking Machine, the following investigations and improvements are suggested for the next steps in this line of research.

6.2.1 Application to non-spherical particles

As stated at the outset of this work, a significant incentive for this project was the technological relevance of dielectrica like MgO and Al_2O_3. In contrast to SiO_2, these are not occurring as spheres, but rather as crystalline grains, which mandates the treatment as non-spherical particles. The relative measurement scheme for the determination of the low-energy electron sticking coefficient is given in [AM2], and can be applied to non-spherical particles using the findings of [AM4]. The only requirement for the latter is a certain degree of knowledge of the particle shape. A future measurement of the sticking coefficients of crystalline dielectrics will require a sufficiently accurate experimental determination of either the 3D particle shape, or of the orientation-averaged projected area, where the latter is expected to be easier to achieve in terms of the experiment. Also, the levitation height of the dielectric grains needs to lie in a region covered by the gold reference curve used for the relative measurement, which may

require minor experimental adjustments.
The results for MgO and Al_2O_3 could then directly be compared to the predictions of Bronold et al. [1]. Furthermore, measuring the sticking coefficient of ZnO would allow for the re-assessment of the experiments by Asnaz et al. [112], see below in Section 6.3.1.

To support studies on plasma catalysis, recent investigations on aeromaterials [199–203] (see also Section 5.3.2) and *metallo-organic frameworks* (MOFs) [211–213] have already been conducted. These were concerned with the conditions necessary to ignite a plasma inside an aeromaterial block [204], and the stability of MOFs subject to heating and atmospheric pressure plasma [214]. Another important property of both aeromaterials and MOFs with respect to plasma catalysis is their charging behavior in the plasma, which can also be investigated using the Sticking Machine. For this, adequately sized (supposedly non-spherical) grains of the respective material are needed which are stable for a long enough time to conduct the sticking measurements. The speed of the PEOM is an important factor for the latter requirement, as it significantly reduces the required lifetime of the grains in the plasma. With respect to the aeromaterials, the considerations regarding the transmission of electrons (Section 5.3.2) play an important role to correctly evaluate the acquired data. Of particular interest would be single, hollow tetrapods of aeromaterial, as they could be compared to the solid tetrapods already investigated [205], possibly yielding insights about electron transmission.

6.2.2 Auxiliary simulation

The PIC code used to gain values for the parameters needed in the calculation of the sticking coefficients in [AM2] and [AM3] was rather simple, as it only considered a 1D situation similar to an infinitely expanded parallel plate discharge. However, the experimental plasma is generated in a tight space ($34\,\mathrm{mm}$ electrode separation, $30\,\mathrm{mm}$ electrode diameter), and the lower electrode contains a cavity. Therefore, it is conceivable that boundary effects may arise that are not considered in the simulation.
To remedy this, more accurate simulations are desirable. Different two-dimensional successor codes to XPDP1 have been developed [215–217] and are available on the website of the *plasma theory and simulation group* at Michigan State University [218]. The particular advantage of these codes is the incorporation of the external circuitry, which is why the results are expected to be close to reality [152]. Optimally, one would use a fully three-dimensional code to account for the complete geometry of the reactor, including the cavity in the lower electrode, boundary effects and possibly even the grounded walls of the vacuum vessel.
It should be noted that the usage of simulations, although widespread in the plasma physics community, implicitly introduces the assumption that the simulation is accurate to reality in the respective parameter range. Therefore, simulation codes should be ideally benchmarked with experimental data, or alternatively by code-to-code verification [219]. For an experimental benchmarking, electron density measurements using techniques such as plasma oscillation probes [220, 221] or microwave cavity resonance spectroscopy (MCRS) [222–225] are suitable.

6.2.3 Electron energy variation

As of now, the measured electron sticking coefficients are averaged over the EEDF at the particle position in the sheath, which is characterized by the local electron temperature $T_\mathrm{e}(h)$. For measurement campaigns using many sizes of particles of interest, for example the silica particles in Refs. [AM2, AM3], the size-dependent levitation height introduces a slight energy variation with the levitation height. In the height range of 5.5 to $8\,\mathrm{mm}$ above the electrode, where the examined particles levitated, the simulated electron temperature varies between ca. 2.2 and $2.5\,\mathrm{eV}$.
To investigate the behavior of $\tilde{s}$ during larger variations of T_e, the electron temperature needs to be adjustable. The easiest way to achieve this is by varying the neutral gas pressure. This can be understood by looking at a simple *uniform density* global model [2] for the bulk plasma as a first-order approximation. In this model, T_e is determined by the balance between electron losses at the plasma boundaries and volume ionization in the plasma bulk. The latter scales with the density of neutral gas that can be ionized. Increasing the neutral gas pressure (and therefore its density) decreases the electron temperature [2]. One needs to keep in mind that the damping rate γ of the particle oscillations utilized in PEOM, PRRM etc. is directly proportional to the pressure, which has to be anticipated when choosing experimental parameters such as the excitation amplitude of the PEOM or the frequency range of the PRRM. Using this, the EEDF over which the sticking coefficient is averaged can be changed, allowing for studies of the electron energy dependence of $\tilde{s}$. However, to attribute sticking coefficients measured at a certain pressure to a mean electron energy or electron temperature, either precise, spatially resolved measurements or simulations of the plasma sheath are necessary.

6.3 Perspectives regarding systems featuring plasma-solid interfaces

As argued in the introduction of this dissertation, plasma-surface interactions are featured in a multitude of situations from basic research to application. With the results obtained in this work regarding the interaction of low-energy electrons with surfaces, implications for several fields of plasma physics research arise. These are presented below.

6.3.1 Dusty plasmas/dust in plasma

The field of dusty plasmas (and dust in plasma) is connected to this research in a special way, as the experimental setup of the Sticking Machine is itself built around a dust-in-plasma situation. The most immediate implications therefore concern topics of dusty plasma research.

Charging difference between conducting and dielectric materials

One prominent question inherently present in the field of dusty plasmas is the difference between metallic and isolating particles in terms of particle charge. As argued in

Section 5.1, the mobility of charge carriers on the particle surface marks an important difference between isolating and conductive particles, which was discussed early on by Manweiler et al. [226]. However, most laboratory studies treated even the isolating polymer particles used in the experiments as conducting, assuming the incoming currents to deposit charges evenly across the particle surface. This point has been discussed in detail in Section 5.1.
Another difference not regarded until now is the difference in electron sticking probability between typical isolating materials, like polymers, ceramics or glass, and metals as typical conductors. Due to the lack of better knowledge, the sticking probability at every dust particle surface was assumed to be constant unity, mimicking the behavior of a perfect absorber. Prior to this work, the bachelor thesis of F. Haase [157] found that an influence of the conductivity of a dust particle on its charge is very likely. The approach was closely related to the one chosen in this work, and used a relative measurement scheme to compare polymer, silica, and gold-coated particles. The height dependence of electron and ion densities and temperatures could however not be considered, so that a quantitative determination of the difference in floating potential was not possible. The uncertainty for the silica particle was furthermore very large, obscuring the low sticking coefficient of silica found in [AM2] and [AM3]. With the Sticking Machine, the floating potential ratio Y was now determined quantitatively and without assumptions about plasma parameters, showing a significant difference between silica and gold particles. The subsequent measurements on polymers also found significant differences to gold particles [AM3]. With these results, it is now apparent that future quantitative evaluations of dusty plasma experiments conducted with polymer, ceramic and other isolating particles should consider the reduced floating potential with respect to metals like gold.

Revisiting previous measurements of the Ersatz capacitor

In 2018, Asnaz et al. [112] reported measurements comparing the charge of PMMA spheres and ZnO tetrapods levitating in the sheath of an Argon rf plasma. Assuming the two materials to have the same sticking coefficient, their results gave rise to the *smallest enclosing sphere* (SES) model, an idea that was later picked up by van Minderhout et al. [102] for the charging of small sphere aggregates in the plasma afterglow. The new results presented in [AM3] shed new light on the results of Asnaz et al., as the sticking coefficient of PMMA is significantly different from 1. The sticking coefficient of the tetrapod's ZnO surface is not known yet, but as ZnO is a semiconductor and has a bulk resistivity of ca. $0.024\,\Omega\,\mathrm{cm}$ [227], it is expected to behave more like a metal (resistivities $\sim 10^{-6}$ to $10^{-5}\,\Omega\,\mathrm{cm}$ [76]) than a dielectric (resistivities $\sim 10^{16}$ to $10^{18}\,\Omega\,\mathrm{cm}$, for typical ceramic materials [76]). Resistivities for ZnO thin films were reported to be in the same order of magnitude as for bulk ZnO [228].
In the framework of I. König's master thesis [205], the charge-equivalent radius a_{eq} of different tetrapods has been determined for different assumptions about the sticking coefficient of ZnO, which is illustrated in Fig. 6.1. When assuming that ZnO and PMMA have the same sticking coefficient, the results of Asnaz et al. are reproduced, in the way that a_{eq} seems to coincide with the SES radius. When assuming a sticking coefficient close to 1 for ZnO, however, the values for a_{eq} agree better with the capacitance,

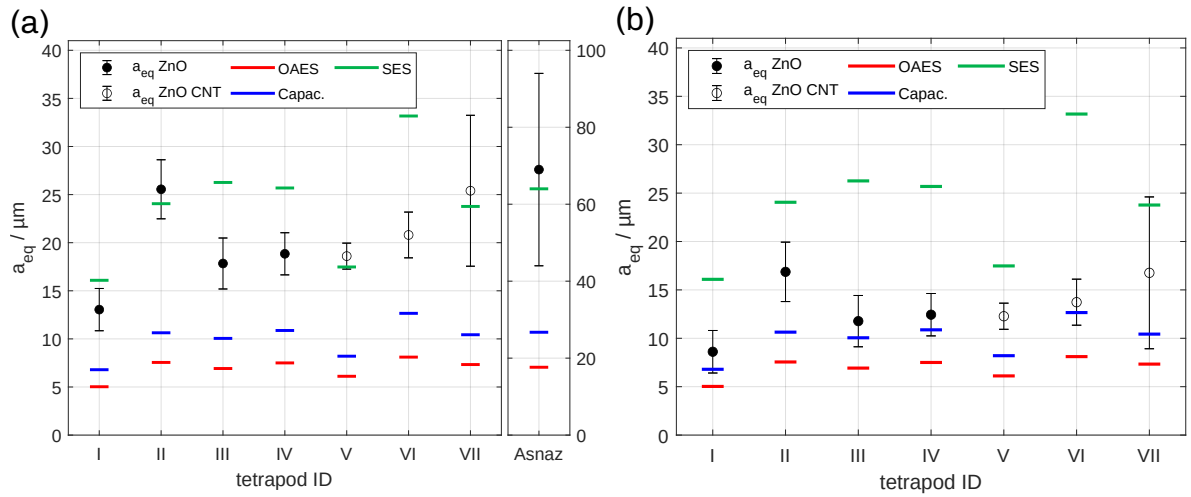

Figure 6.1: Measured radii a_{eq} of a sphere with equivalent charge for uncoated ZnO tetrapods (solid black circles), and ZnO tetrapods coated with carbon nano tubes (hollow circles). The predictions for a_{eq} based on the capacitance (blue markers), OAES model (red markers) and SES model (green markers) are also shown. In (a), the sticking coefficient of ZnO is assumed to be the same as that of PMMA found in [AM3]. For comparison, the data for the tetrapod investigated by Asnaz et al. [112] is also shown in (a); Note the different y axis there. In (b), the evaluation of the same data is shown, but it is assumed that ZnO has the same sticking coefficient as gold, which is expected to be 1. For details on the predictions for a_{eq}, refer to Chapter 5 and [AM4]. *From* [205], reproduced with permission.

which would be in line with the general result of [AM4] that the capacitance is the best description of the equivalent radius. Based on this, it can be conjectured that ZnO has a sticking coefficient close to 1, which could be assessed in detail with future measurements of the sticking coefficient of ZnO.
This is an important example how the consideration of the sticking coefficient impacts the interpretation of dusty plasma experiments, as the choice of assumption about the sticking coefficient of ZnO fundamentally changes the interpretation of the measured data.

Janus particles

Janus particles are special particles with one hemisphere or side featuring a different surface material than the other [229]. For dusty plasma experiments, they are usually fabricated by coating one hemisphere of a polymer particle with a noble metal such as Au or Pt. Plasma crystals containing these particles can exhibit highly complex behavior [230, 231]. It is reasonable to conjecture that their unique, two-sided character plays a role in this complex behavior. When the respective hemisphere surface materials have different electron sticking coefficients, the formation of an electric dipole is expected even in isotropic plasma conditions, giving rise to potentially complicated

dynamics especially in the sheath electric field or in the interaction with other dust particles, similar to observations of interactions between rodlike particles leading to chaotic oscillations reported by Udrea et al. [177].

Binary dusty plasmas

Plasma crystals formed from two or more different particle species, so-called *binary dusty plasmas*, gained research interest as a realization of a binary mixture over the last few years [232–238]. Oftentimes, 2D systems are desired, which requires precise tuning of the levitation height of both particle species relative to each other. Even a slight mismatch in the charge-to-mass ratio q/m can lead to phase separation, inhibiting the preparation of a truly mixed system [233–235, 237]. In practice, one uses one inert particle species, typically SiO_2, and another species of particles subject to mass loss in the plasma [64, 108–110, 118–120, 145], usually PMMA or MF. In the case of MF, the mass loss requires a small oxygen admixture. This allows for a potentially long-lived binary system by switching off the oxygen flux once the levitation heights are matched. When predicting the size and/or charge ratio between the particle species, it is often assumed that both species have the same electron sticking coefficient of unity [234]. As these happen to be the exact same materials the electron sticking coefficients have been measured for here, the predictions can now be improved by using the values for $\tilde{s}$ acquired in an extremely similar experimental context [AM2, AM3]. Furthermore, descriptions of the collective behavior in such systems benefit from more accurate values for the particle charges and the charge ratio between the species. Combined with knowledge about the electron and ion densities and the electric field in the sheath, even predictions of particle levitation heights are expected to be possible.

Electron-depleted dusty plasmas

In dusty plasma systems with dense dust clouds, both astrophysical [57, 239] and laboratory plasmas featuring nanometer-sized dust [58, 59, 91], the electron collection by the dust surface can lead to an electron depletion in the surrounding plasma, which is known as the *Havnes effect*. The Havnes parameter P characterizes the degree of electron depletion [56, 59, 240], with values greater than 1 indicating the occurrence of electron depletion. In the case of electron depletion, the majority of the plasma electrons is bound on the dust particles. Up to today, theoretical descriptions of particle charge in the context of the Havnes effect always assumed perfectly electron-absorbing dust particles [59, 91]. However, the Havnes effect is often investigated on plasmas with nanoparticles grown from silane, methane, or acetylene. Common resulting particle materials, such as amorphous hydrocarbons (a:C-H) or silicon compounds, are more likely to exhibit the characteristics of a dielectric than that of a metal. It is therefore expected that they also feature sticking coefficients below 1, lowering their ability to absorb electrons from the plasma. In turn, this means their charge is significantly lower than expected when assuming perfectly absorbing dust, and the Havnes effect should be less pronounced for these dielectric particles.
To aid future investigations of electron depletion, the sticking coefficients of the relevant materials can now be measured using the Sticking Machine. As the particle growth

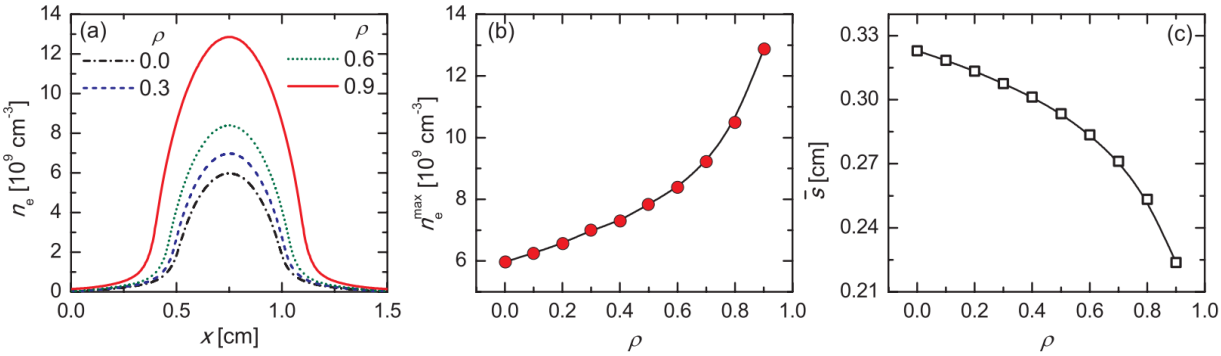

Figure 6.2: Influence of the electron reflection coefficient $\rho = 1 - s$ on the electron density profile of a parallel-plate discharge. (a) Spatial electron density profile for different ρ; (b) Maximum electron density n_e^{max} in the discharge; (c) Sheath width $\bar{s}$. Higher reflection coefficients generally correspond to a denser plasma with a slightly smaller sheath width. *Reproduced from I. Korolov et al., Plasma Sources Sci. Technol.* ***25****, 015024 (2016)* [34] *with permission of IOP Publishing, Ltd. Permission conveyed through Copyright Clearance Center, Inc.*

process results in spherical particles, the simpler measurement scheme for spherical particles is applicable. While particles growing beyond a certain size cannot be trapped anymore in most experiments, particle radii up to a few micrometers can be reached under certain experimental conditions [241, 242]. The particle size of a few micrometers is necessary to allow for a sufficiently precise radius determination using long distance microscopy. The sufficiently large grown particles could then be extracted from the reactor in which they were grown, for example using an electrostatic extractor [243], and introduced into the Sticking Machine. The results for the sticking coefficients of these grown particle materials could then help improve the modeling and evaluation of laboratory, electron-depleted plasma experiments.

6.3.2 Plasma diagnostics

Electrical probes, such as classical Langmuir probes [134, 135] or emissive probes [244], are another prime example of surfaces in contact with plasmas. Surface modification and contamination of the probe affects the results of the measurements [245]. Therefore, knowledge of the sticking coefficients of differently contaminated probe materials could improve the accuracy of measurements using electrical probes.

6.3.3 Reactor design

The loss of electrons at walls and electrodes has a significant influence on the plasma density profile in a plasma reactor. Simulations by Korolov et al. [34] indicate that the electron sticking coefficient of the electrodes impacts the shape of the density profile, in particular the maximum density as well as the sheath width, which is also

shown in Fig. 6.2. As the energies of electrons impinging on the electrodes of typical parallel-plate rf reactors are in the range of a few eV, these sticking coefficients are in the energy range accessible by the Sticking Machine. Determining electron sticking coefficients of typical electrode or dielectric barrier materials therefore helps the accuracy of simulations as well as the estimation of plasma parameters in experiments. When the electrodes feature different electron sticking coefficients, a dc self bias can arise [34]. In double-frequency driven process plasmas, this is beneficial as it allows tuning of the ion properties, namely the ion flux and mean ion energy, by intensifying the *electrical asymmetry effect* [34, 246, 247]. A similar effect is found for different ion-induced secondary electron emission coefficients of the electrodes [31, 32, 248]. A computationally assisted approach to determine the ion-induced SEE coefficient has been presented recently by Masheyeva et al.[36]. Schulze et al. [35] have proposed a similar approach using a symmetric discharge, yielding the ion-induced secondary electron emission coefficient of electrode materials, as well as an effective electron reflection coefficient.
A comparison between electron sticking coefficients obtained from measurements with the Sticking Machine, and from the electron reflection coefficients measured with the technique of Schulze et al. [35] could yield further insights into the influence of electron emission and reflection at the electrodes on the plasma density profiles.

6.4 Summary

The focus of this work was the development of the Sticking Machine, a novel setup able to measure low-energy electron sticking coefficients of arbitrary materials. The low electron energies of only a few eV were achieved by using a low-pressure plasma with single microparticles of the materials of interest trapped in the lower sheath. For this, a new, fast high-precision measurement method for the determination of the particle charge-to-mass ratio q/m was developed, the PEOM. It is based on the damped driven oscillation of the dust particles in the harmonic trap created by gravity and the linear sheath electric field. Using the PEOM, a relative measurement scheme was established and used to prove a significant charging difference between silica and gold indicated by a different floating potential. With auxiliary simulations and an extended model for the anisotropic ion current in the sheath, the electron sticking coefficient of silica could be calculated for single-digit-eV energies, which was significantly below 1. Further investigations yielded the sticking coefficients of the polymers PMMA and MF, which are widely used in dusty plasma physics. Their sticking coefficients are also significantly below 1. Both the results for silica and the polymers are expected to have an impact on future laboratory dusty plasma research. Finally, the extension of the Sticking Machine measurement scheme to non-spherical particles was discussed. It was found that a non-spherical geometry is equivalent to a spherical Ersatz capacitor, whose radius is directly related to the electrical capacitance of the geometry. Two geometrical approximation models for the capacitance have been discussed, showing that the OAES model may be used as an approximation under certain circumstances, while the SES model is not to be used as an approximation.

With the Sticking Machine as a new measurement method for electron sticking coefficients now operational, perspectives for different topics of plasma physics have been illustrated, and future investigations using and improving the Sticking Machine have been proposed.

Scientific Contributions

List of own publications

[AM1] A. Mengel, M. Artz, and F. Greiner, “Pulse excited oscillation: A new high-precision excitation method for the charge-to-mass ratio determination of microparticles in plasma and comparison to stepwise excitation and the phase-resolved resonance method”, Physics of Plasmas **30**, 123704 (2023).

[AM2] A. Mengel, F. X. Bronold, and F. Greiner, “Evidence of different charging behavior of conductive and dielectric materials in low-temperature plasmas and a new diagnostic for low-energy electron absorption”, Physical Review Letters **133**, 185301 (2024).

[AM3] I. König, A. Mengel, and F. Greiner, “Electron sticking coefficients of dusty plasma relevant materials”, Physics of Plasmas **32**, 024501 (2025).

[AM4] A. Mengel, I. König, L. S. Matthews, and F. Greiner, “Approximation formula for the capacitance of a non-spherical particle in a low-pressure plasma”, Physics of Plasmas **32**, 033703 (2025).

Declaration of own contribution to the publications

The following section will delineate my contribution to the publications that constitute this cumulative dissertation.

Pulse excited oscillation: A new high-precision excitation method for the charge-to-mass ratio determination of microparticles in plasma and comparison to stepwise excitation and the phase-resolved resonance method

I designed and built the experimental setup, and made sure it was operational. Additional programs necessary for the operation were written by me. First tests of the PEOM were done together with M. Artz during the work for his bachelor thesis [249] under my instruction and supervision. I then planned the experimental procedure for a larger scale investigation, and conducted the experiments according to it. I wrote the scripts utilized in the evaluation of the data. M. Artz conducted the simulations for the accuracy of the PEOM under my instruction. The paper itself was written by me, with proofreading and advisory comments by F. Greiner.
The accompanying erratum corrects a typesetting error and can be found as

[AM1a] A. Mengel, M. Artz, and F. Greiner, “Erratum: “Pulse excited oscillation: a new high-precision excitation method for the charge-to-mass ratio determination of microparticles in plasma and comparison to step-wise excitation and the phase-resolved resonance method””, Physics of Plasmas **31**, 129902 (2024).

The article and the erratum have been reprinted from [AM1] and [AM1a], respectively, with the permission of AIP Publishing.

Evidence of Different Charging Behavior of Conductive and Dielectric Materials in Low-Temperature Plasmas and a New Diagnostic for Low-Energy Electron Absorption

The basic concept of the relative measurement scheme was initially described by F. Greiner and F. X. Bronold in the project proposal [77]. After preliminary studies, I improved upon the scheme by using multiple sizes of gold-coated reference particles instead of a continually etched polymer particle, as well as a more accurate description for the relation between charge and sticking coefficient. The same experimental setup as in [AM1] was used, with the addition of a long-distance microscope, which I installed on the setup. The experiments were planned and conducted by me, and I also did the evaluation. The article was written by me, with proofreading and advisory comments by F. Greiner and F. X. Bronold. In the first revision, additional considerations regarding the ion current were suggested, for which I developed a new model described in the accompanying supplemental material. The XPDP1 simulation data was provided by F. Greiner.
The publication has been reprinted from [AM2] with the permission of the American Physical Society.

Electron sticking coefficients of dusty plasma relevant materials

This publication bases on experiments done in the framework of the master thesis of I. König [205]. I designed the improved experimental setup and helped making it operational. I provided the programs for the operation of the experiment as well as most of the evaluation scripts. The experimental procedure was the same I already developed for [AM2]. The experiments and their evaluation were done together with I. König under my instruction and supervision. The concept of the paper was drafted and discussed by F. Greiner and me. It was then written by F. Greiner and proofread by me and I. König.
The paper has been reprinted from [AM3], with the permission of AIP Publishing.

Approximation formula for the capacitance of a non-spherical particle in a low-pressure plasma

This publication also partially bases on experiments done in the framework of the master thesis of I. König [205], which were done at the same setup as [AM3]. The experimental procedure was developed by me, and the experiments and their evaluation were conducted together with I. König under my instruction and supervision. The numerical

calculation of the capacitances, projected areas and bounding spheres was conducted by me, as well as the derivation of the correction factor F. The simulation data for the larger aggregates was provided by L. S. Matthews, and further evaluated by me. The overall evaluation was done by me. The article was written by me, with edits by L. S. Matthews and I. König. Proofreading and advisory comments were done by F. Greiner and L. S. Matthews.
This article has been reprinted from [AM4], with the permission of AIP Publishing.

Physics of Plasmas ARTICLE pubs.aip.org/aip/pop

Pulse excited oscillation: A new high-precision excitation method for the charge-to-mass ratio determination of microparticles in plasma and comparison to stepwise excitation and the phase-resolved resonance method

Cite as: Phys. Plasmas **30**, 123704 (2023); doi: 10.1063/5.0181035
Submitted: 13 October 2023 · Accepted: 28 November 2023 ·
Published Online: 15 December 2023

Armin Mengel,[a] Maurice Artz,[b] and Franko Greiner[c]

AFFILIATIONS

Institute of Experimental and Applied Physics, Kiel University, 24118 Kiel, Germany

[a]Author to whom correspondence should be addressed: mengel@physik.uni-kiel.de
[b]Electronic mail: stu209234@mail.uni-kiel.de
[c]Also at: Kiel Nano, Surface and Interface Science KiNSIS, Kiel University, Germany. Electronic mail: greiner@physik.uni-kiel.de

ABSTRACT

The charge-to-mass ratio of microparticles confined in the sheath of an RF plasma is the key parameter for the understanding and theoretical description of dusty plasmas. Standard techniques, like the resonance method (RM) and the phase-resolved resonance method (PRRM) based upon the harmonic oscillator model of the microparticle, are used to determine the charge-to-mass ratio. However, if high precision is required, these methods become relatively slow. In this work, we present two transient response-based methods, the step excited oscillation method, adapted and modified from Meijaard *et al.* [Phys. Plasmas **28**, 083502 (2021)], and the new pulse excited oscillation method (PEOM). A careful comparison to the PRRM and others is presented. The PEOM offers a significant increase in speed while maintaining a precision comparable to that of the PRRM.

I. INTRODUCTION

The systems commonly used to study dusty plasmas are microparticles confined in the sheath of an RF plasma.[1,2] Aside from the utilization of plasma crystals as a model system for strongly coupled systems, individual particles increasingly find application as minimally perturbative probes,[3] for example, as diagnostics for the sheath potential shape,[4–7] impulse flux in ion beams,[8,9] or as thermal probes.[10] Other methods like the rotating electrode method (REM) employ microparticles to access particle properties such as the charge as well as plasma parameters like the Debye length.[11] To understand the behavior of the particle and its interaction with the surrounding plasma, knowledge of the particle properties is essential. One such property is the particle's charge-to-mass ratio q/m. Shortly after the successful generation of plasma crystals in the laboratory,[12–14] the first resonance method for q/m determination was presented.[15] Since then, multiple methods to determine q/m have been developed that rely on the modeling of the trapped particle as a harmonic oscillator. Instead of an electrostatic excitation as in the RM, the particle can also be excited by applying radiation pressure with a laser beam.[16] An improvement over the resonance method, the phase-resolved resonance method (PRRM)[17] allows for high-precision measurements of the eigenfrequency ω_0 and neutral drag coefficient γ of the particle and was successfully used to show the degeneration of plastic microparticles inside of the plasma sheath.[18] This method, which can be called the "working horse" of high precision determination of q/m, has so far been successfully applied to the investigation of several research questions, such as the ion wake,[19] charging of non-spherical particles,[20] the mass- and density change of polymer particles in the plasma,[18,21] and for the determination of q/m in binary mixtures of microparticles.[22] Unfortunately, the high precision of the PRRM is associated with a large time requirement, which is detrimental for time-critical processes like plasma-inherent etching[21,23–25] of polymer particles. Recently, it was shown that q/m can in principle also be obtained with a stepwise modulation of the RF power.[26] This causes an attenuated oscillation

motion of the particle, which can then be analyzed. Related methods have been used to examine particle pairs and their interaction potential[27,28] or the shape of the electric potential in the sheath.[7] In all these approaches, the excitation consists of a singular, practically instantaneous event, which causes a transient state of the particle as an oscillator to occur. The trajectory during this transient response is then evaluated according to the individual method. These methods are therefore called transient response methods. In contrast, the data of the RM and PRRM stems from a multitude of individual steady states arising from single-frequency sinusoidal excitation. The resulting resonance curve is a compound of all this information. Transient response approaches have the potential to be much faster than the PRRM and RM, because there is no need to vary the driving frequency of the driver, which is time-consuming because the resolution depends on the chosen frequency steps and the decay of transients. Instead, the step function (or a signal with similarly abrupt changes) used as an excitation signal contains theoretically all possible frequencies in its spectrum. The transient response methods can therefore also be called multi-frequency excitation methods, in contrast to the single-frequency excitation methods or steady-state response methods RM and PRRM.

In this work, we present a precise and fast method based on a pulsed excitation of single dust particles and critically compare it to the PRRM and stepwise excitation methods. Section II will cover the theoretical background, the concept of the different methods, and the necessary model functions for the evaluation of each method's data. After describing the experimental setup and the measurement and analysis procedures in Sec. III, the findings will be presented and thoroughly discussed in Sec. IV, before a final conclusion is drawn in Sec. V.

II. MEASUREMENT CONCEPT AND CONSIDERATIONS

A. Forces on the microparticle

A dust microparticle in the sheath of an RF plasma attains a large negative charge q_d of several 10^3–10^4 elementary charges.[1,2] As there is no cloud of other dust particles, there is first no interaction with other particles, and second the plasma suffers no electron depletion due to the Havnes effect.[29,30]

The particle is subjected to multiple forces, which scale differently with the particle radius a. Of these, the gravitational ($\propto a^3$), electrostatic ($\propto a$), and neutral drag forces ($\propto a^2$) are dominant. Other forces are the thermophoretic force ($\propto a^2$), which can be neglected because there is no measurable temperature gradient in the experiment, and the ion drag force ($\propto a^2$), which is estimated using the models by Hutchinson and Khrapak as detailed in the textbook by Melzer.[1] Using typical values for the sheath ($k_B T_e = 3\,\mathrm{eV}$, $k_B T_i = 30\,\mathrm{meV}$, $a = 3.7\,\mu\mathrm{m}$, and $n_i = 1.2 \times 10^{14}\,\mathrm{m}^{-3}$), the ion drag is calculated to be at least one order of magnitude weaker than the gravitational and electrical force and therefore neglected in this work.

In mechanical equilibrium, the particle levitates at a height z_0 determined by the balance between the gravitational force $F_g = m \cdot g$ and the electrostatic force $F_{el}(z) = q_d \cdot E(z)$. In motion, the particle's movement is attenuated by the neutral drag force $F_{nd} = -\gamma \cdot \dot{z}$. For spherical particles, this is described by the Epstein friction[31] with

$$\gamma = \delta \frac{4}{\pi} \frac{p}{a \rho_m \hat{v}_{th,n}}. \tag{1}$$

Here, ρ_m is the mass density of the particle material and $\hat{v}_{th,n}$ is the thermal velocity of the ambient neutral gas. δ is a geometric coefficient, which value was shown to be 1.44 for microparticles in typical laboratory circumstances.[17] Finally, the dust grain can be accelerated by an arbitrary external driving force $F_{ext}(t)$. This system may be treated as a driven harmonic oscillator for small vertical displacements from the equilibrium position z_0, because the potential is still parabolic, while nonlinear effects arise at higher amplitudes.[32] This leads to the well-known equation of motion for the driven harmonic oscillator

$$\ddot{z} + 2\gamma\dot{z} + \omega_0^2 z = \frac{1}{m} F_{ext}(t). \tag{2}$$

Assuming that the height dependence of the particle charge is much smaller than that of the electrical field in the sheath, the eigenfrequency ω_0 of this system can be written as

$$\omega_0 = \sqrt{\frac{q_d \rho_q}{m \varepsilon_0}}. \tag{3}$$

ρ_q is the absolute charge density at the position of the particle in the sheath. (The index q is chosen to avoid confusion with the mass density ρ_m.) The RM and PRRM utilize this by evaluating the system's (in the case of PRRM complex) resonance curve $A(\omega)$ resulting from excitation with a sinusoidal frequency sweep to obtain the parameters ω_0 (eigenfrequency) and γ (see also Fig. 4). Another characteristic frequency worth mentioning is the resonance frequency $\omega_r = (\omega_0^2 - 2\gamma^2)^{\frac{1}{2}}$. It marks the maximum of the amplitude's absolute value $|A(\omega)|$ in the resonance curves of the RM and PRRM. On the other hand, the stepwise excitation method (called SEOM for step-excited oscillation method below), as well as the method presented in this work, the pulse-excited excitation method (PEOM), utilizes the response of the particle to a step- or (rectangle-) pulse-shaped excitation signal directly in the time domain. This response is a damped oscillation (see Secs. II B and II C) with a characteristic frequency $\omega_d = (\omega_0^2 - \gamma^2)^{\frac{1}{2}}$, the damped eigenfrequency. It is important to differentiate between ω_d and ω_r, as they are slightly different.

B. Excitation mechanisms

There are multiple ways to generate an electrical excitation (driving force) to this system, of which those two will be focused on that are found to be most practical in the laboratory situation. Both rely on distorting the sheath by a small extent and with it the equilibrium position z_0. The first way, labeled as "modulated," is by amplitude-modulating the RF power that generates the plasma with an additional low-frequency signal. This changes the spatial extent of the plasma and thus the equilibrium position of the levitating microparticle. One can reasonably assume that the signal modulation and the change in the plasma occur quasi-instantly relative to the timescale of the particle motion, which has a damped eigenfrequency of around 10 Hz. Thus, the resulting driving force is directly proportional to the modulation signal. The second way, labeled "bias" below, is by adding the excitation signal as a bias voltage to the driven electrode. This adds the need to incorporate a filter network (shown in Fig. 1) into the experimental setup in order to protect the hardware generating the low-frequency excitation signal against the RF voltage. The effect of this filter network

Physics of Plasmas ARTICLE pubs.aip.org/aip/pop

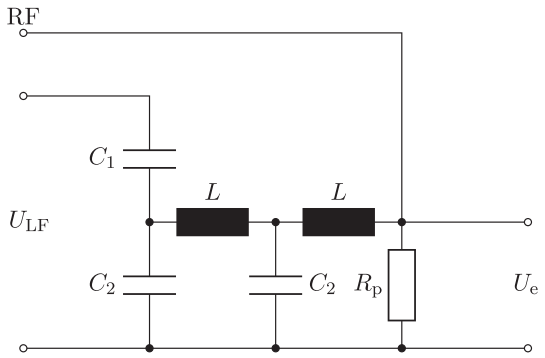

FIG. 1. Circuit diagram of the filter used to shield the signal generation hardware from the RF voltage. The capacitors have the values $C_1 = 1\,\mu$F and $C_2 = 4.7$ nF, and the inductivities both have the value $L = 40\,\mu$H. R_p represents the Ohmic resistance of the plasma, which changes with the discharge parameters.

has to be incorporated into the model. Regarding the RF signal, the filter network acts as a fourth-order low-pass filter. Because the considered excitation signals are low-frequency signals, the impedance of the inductivities $Z_L(\omega) = i\omega L$, which vanishes in the limit of low frequencies, can be neglected, as the impedance of the capacitors $Z_C(\omega) = 1/(i\omega C)$ dominates for low ω. There are multiple ways to determine the effect of the filter on the incoming signal. For periodic signals, this is usually done by determining the system's frequency-dependent transfer function $H(\omega)$, which can be easily written by looking at the filter network as a voltage divider as follows

$$H(\omega) = \frac{U_e}{U_{LF}} = \left(1 + \frac{2C_2}{C_1} + \frac{\omega_g}{i\omega}\right)^{-1}, \tag{4}$$

where $\omega_g = 1/(R_p C_1)$ is the system threshold frequency, and R_p is the Ohmic plasma resistance, which depends on the discharge parameters such as RF power and pressure. While this approach is well suited for methods like the PRRM[17] that employ periodic signals, it is difficult to apply to the step- and pulse signals used in SEOM and PEOM. In this case, the system's Green's function is a much easier way to determine U_e from U_{LF}. By analyzing the circuit diagram with Kirchhoff's circuit laws, one can first derive a first-order ordinary differential equation for the in- and output voltages U_{LF} and U_e,

$$\left[\frac{d}{dt} + \nu\right] U_e = c\dot{U}_{LF}, \tag{5}$$

with $c = (1 + 2C_2/C_1)^{-1}$ and $\nu = c/(R_p C_1)$. ν is related to ω_g as $\nu = c \cdot \omega_g$. Because the plasma resistance R_p contained in ν is the only unknown variable of the filter network, ν is introduced as a fit parameter into the fit models for the bias methods. Because the capacities C_1 and C_2 are known, R_p can then be calculated.

In Eq. (5), only the derivative $\dot{U}_{LF} = \frac{dU_{LF}}{dt}$ of the input voltage $\dot{U}_{LF}$ appears, so the filter acts as an analog differentiator for low-frequency signals. Using the Fourier transform of Eq. 5 and the residue theorem, one can easily write Green's function G_f for the differential operator in Eq. (5) as

$$G_f(t - t') = \theta(t - t') \cdot e^{-\nu(t-t')}. \tag{6}$$

This allows us to calculate the response to any input signal $U_{LF}(t)$ as

$$U_e(t) = \int_{-\infty}^{\infty} G_f(t - t') \cdot c\dot{U}_{LF}(t')dt'. \tag{7}$$

In particular, we can use this to model the driving force $F_{ext}(t) \propto U_e(t)$ and obtain the particle's response to $F_{ext}(t)$ using Green's function G_p of the particle as a harmonic oscillator (which is routinely derived in many mathematical textbooks[33])

$$G_p(t - t') = \theta(t - t') \cdot e^{-\gamma(t-t')} \cdot \frac{\sin(\omega_d(t - t'))}{\omega_d}. \tag{8}$$

This response function can then be used as a fit function $z(t)$ to extract the parameters ω_d and γ, among others.

C. Model functions

In addition to the PRRM, which will act as a reference method, there are three closely related excitation methods examined in this work. Their characteristic excitation signal shapes, particle responses, and the corresponding behavior of the plasma RF voltage are shown in Fig. 2.

1. Modulated SEOM (moduSEOM)

Meijaard *et al.*[26] introduced the SEOM with a power modulation in the form of a Heaviside step function $\theta(t)$. For a single step excitation, the cycle-averaged RF power P_{RF} is modeled as

$$P_{RF}(t) = P_i \pm \theta(t) \cdot \Delta P, \tag{9}$$

where P_i is the initial power, and ΔP is a power step-up- or downward occurring at $t = 0$, resulting in a power of $P_e = P_i \pm \Delta P$. In the experiment, this is realized by applying a slow square signal ($T = 2$ s) and evaluating the response to each slope. One has to consider that the

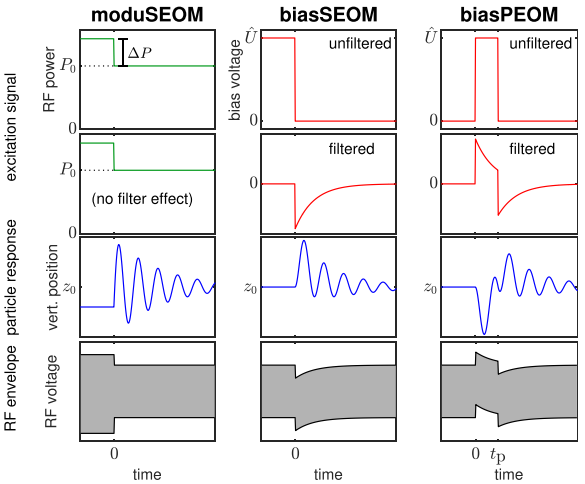

FIG. 2. Overview of the three different excitation types in this work. Notice that the excitation signal for the modulated SEOM is displayed as the change in RF power (green), while the excitation signals of the bias methods are shown as voltages (red). The LF envelope of the RF signal at the lower electrode is displayed in gray.

oscillator parameters obtained are those corresponding to the RF power after the slope, as the plasma parameters and particle charging take place on timescales < 0.5 ms, which is about three orders of magnitude faster than the particle oscillation ($T \approx 100$ ms). We can then assume that the change in z_0 can be reasonably treated as instantaneous, and the external driving force on the particle can be written as

$$F_{\mathrm{ext}}(t) = B \cdot \theta(t), \tag{10}$$

with B being the resulting amplitude of the force step. The particle response can then be modeled with the following fit function:[34]

$$z(t) = z_0 + D \cdot e^{-\gamma t} \cdot \sin(\omega_d t), \tag{11}$$

where D is the initial amplitude containing the direction of the slope and the resulting initial motion in its slope.

2. Bias-SEOM (biasSEOM)

As discussed above, the filter necessary in experimental setups with bias excitation distorts the excitation voltage signal U_{i}. For a Heaviside-step $U_{\mathrm{i}}(t) = U_{\mathrm{b}} \cdot \theta(t)$, the resulting driving force is easily calculated [because $\dot{U}_{\mathrm{i}}(t) \propto \delta(t)$] using Eq. (7) and is written as

$$F_{\mathrm{ext}}(t) = B \cdot e^{-\nu t} \cdot \theta(t). \tag{12}$$

Using the oscillator's Green's function [Eq. (8)], one can obtain the particle's response

$$z(t) = z_0 + D \cdot \left[e^{-\gamma t} \sin(\omega_{\mathrm{d}} t - \phi) + b \cdot e^{-\nu t}\right], \tag{13}$$

with the quantities $b = \left(1 + (\nu - \gamma)^2/\omega_{\mathrm{d}}^2\right)^{-1/2}$ and $\phi = \arctan(\omega_{\mathrm{d}}/(\nu - \gamma))$. This is a damped oscillation superimposed with an exponential decaying offset due to the filter network. A sufficient oscillation amplitude can be reached with a far smaller perturbation of the plasma, as the input excitation amplitude $\hat{U}_{\mathrm{b}}$ is only 1 V compared to the peak-to-peak RF voltage of about 60 V and the self-bias of roughly -50 V. The slope direction still influences the resulting parameters but not nearly as strongly as in the modulated case.

3. Bias-PEOM (biasPEOM)

The next improvement consists of using a rectangle pulse with a duration t_{p} instead of a single step as an excitation as follows:

$$U_{\mathrm{i}}(t) = U_{\mathrm{b}} \cdot (\theta(t) - \theta(t - t_{\mathrm{p}})). \tag{14}$$

Exploiting linearity, we can construct our driving force

$$F_{\mathrm{ext}}(t) = B \cdot (e^{-\nu t} \cdot \theta(t) - e^{-\nu(t-t_{\mathrm{p}})} \cdot \theta(t - t_{\mathrm{p}})) \tag{15}$$

and particle response from the biasSEOM case

$$z(t) = z_0 + D \cdot \Big[e^{-\gamma t} \sin(\omega_{\mathrm{d}} t - \phi) + b e^{-\nu t} - e^{-\gamma(t-t_{\mathrm{p}})} \sin(\omega_{\mathrm{d}}(t - t_{\mathrm{p}}) - \phi) - b e^{-\nu(t-t_{\mathrm{p}})}\Big]. \tag{16}$$

From the resulting fit parameters, the eigenfrequency can be calculated as

$$\omega_0 = \sqrt{\omega_{\mathrm{d}}^2 + \gamma^2}. \tag{17}$$

While the precision for ω_0 is mathematically dependent on both ω_{d} and γ, it can be easily verified using the basic error propagation that it is primarily given by the precision of ω_{d} for $\gamma \ll \omega_{\mathrm{d}}$. Under the experimental circumstances in this work, $\gamma < 0.09\omega_{\mathrm{d}}$ was found, and it is thus assumed that the uncertainty in γ has only a small influence on the uncertainty of the calculated ω_0.

The pulse duration t_{p} can be chosen deliberately. In this work, we conducted the biasPEOM with pulse durations of 10, 50, and 100 ms. A simple consideration regarding this is that the amplitude should reach its maximum when the acceleration takes place, while the velocity is at its maximum and in the same direction as the acceleration. The second slope should thus occur after roughly half a period T_{d} of the particle's oscillation, so that the external pulse acceleration is approximately in phase with the particle's oscillation. This leads to a criterion for the pulse duration $t_{\mathrm{p,opt}}$ with the maximum resulting amplitude

$$t_{\mathrm{p,opt}} \approx \frac{T_{\mathrm{d}}}{2} = \frac{1}{2f_{\mathrm{d}}} = \frac{\pi}{\omega_{\mathrm{d}}}. \tag{18}$$

The particles used in this work had damped oscillation frequencies close to 10 Hz, so $t_p = 50$ ms was chosen as an optimal pulse duration. The shorter and longer pulse durations were chosen for comparison to assess the validity of the criterion Eq. (18).

III. EXPERIMENTAL PROCEDURE

A. Setup

The measurements are conducted in the *StickingCube* plasma chamber (shown in Fig. 3), a capacitively coupled RF discharge operated with argon at a pressure of 5.5–10 Pa. A flow controller is used to adjust the pressure in the vacuum vessel. The plasma setup consists of two circular electrodes with a diameter of 30 mm and a distance of

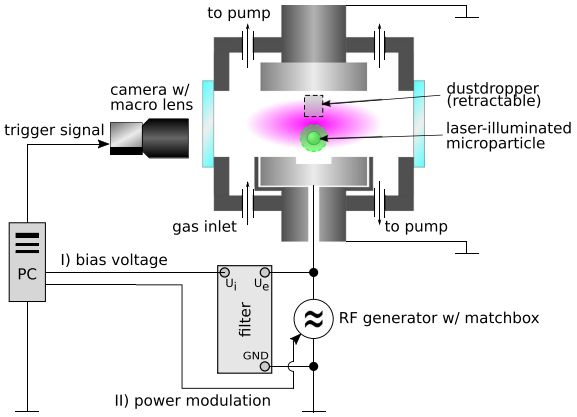

FIG. 3. Schematic, not-to-scale depiction of the experimental setup. The laser illuminates the particle from in front of the drawing plane, while the dustdropper can be retracted behind the drawing plane. The PC interface generates and coordinates the excitation and camera trigger signals. Both excitation mechanisms are incorporated into the electrical setup (lower portion of the picture): In case I), the excitation is generated as a voltage signal U_{i} at the input of the filter, resulting in an additional bias voltage at the driven electrode. In that case, the RF power is kept constant (no modulation). In case II), the RF power is modulated with the excitation signal. In that case, the input U_{i} of the filter is disconnected, preventing an influence of the filter in this case. In both cases, the lower electrode is capacitively separated from the ground and thus attains a negative self-bias voltage.

Physics of Plasmas ARTICLE pubs.aip.org/aip/pop

34 mm, and the RF-driven lower electrode features a cylindrical cavity with a diameter of 10 mm and a depth of 2 mm. This cavity geometry produces an electric field component in the radial direction in the sheath, which confines the negatively charged microparticles horizontally above the center of the electrode. The upper electrode is grounded, while the lower electrode is driven by an RF generator outputting 1.5 W. The RF power can be modulated with an analog input connected to a computer interface. Additionally, a low-frequency bias voltage signal can be applied to the lower electrode via the aforementioned filter network. The total RF signal between the electrodes is monitored with an oscilloscope. Between the bias and modulated configuration, the self-bias voltage U_{sb} and the amplitude $\hat{U}_{RF}$ of the RF voltage do not change. However, while the power is raised to 1.9 W in the modulated case, the self-bias drops from about -50 to -55 V, and the RF voltage amplitude rises from circa 60 V peak-to-peak to almost 70 V peak-to-peak. During the bias excitation, no difference in U_{sb} or $\hat{U}_{RF}$ could be observed within a resolution of 0.4 V. SiO_2 microspheres ($2a = 7.38 \pm 0.24\,\mu$m according to the manufacturer) are individually introduced into the plasma sheath via a retractable dustdropper. SiO_2 is chosen as the particle material because it is practically unaffected by plasma-inherent etching, unlike other common materials like melamine formaldehyde (MF) or polymethyl methacrylate (PMMA).[24] A computer interface allows for analog and digital in- and outputs and is controlled via National Instruments LabVIEW[35] for automated data acquisition. It outputs all the required excitation and timing signals and is used to monitor the pressure, RF amplitude, and RF self-bias voltage. The excitation signals for PRRM, moduSEOM, biasSEOM, and biasPEOM are generated by a LabVIEW program and coupled into the discharge as either a modulation of the RF power or an additional bias voltage signal at the lower electrode after passing the filter network. A high-speed camera with a macro lens is triggered by a digital output signal. The camera has a resolution of 1440×1080 pixel (16 megapixel) on a $4.97 \times 3.73\,\text{mm}^2$ CMOS sensor, with a pixel size of 3.45 μm. For the PRRM, the trigger occurs four times per period of the excitation signal, while the other time series for the other methods are recorded at 200 frames per second. The particle is illuminated by a green laser ($\lambda = 532$ nm) with 250 mW that is expanded to circa. 9 mm diameter using a beam expander optic, in order to illuminate the whole area in which the particle oscillates. A mirror configuration allows for adjustment of the illuminated area. The LabVIEW program automatically detects the particle's position on the camera image and saves it together with the corresponding timestamp. Using an image of a scale between the electrodes before or after the measurement, the pixel position of the particles is calibrated to the absolute height above the lower electrode, with a distance of 1 pixel corresponding to 4.74 μm.

B. Evaluation

Each of the 13 single particles was examined individually at 5.5, 7.5, and 10 Pa using all the methods (moduSEOM, biasSEOM, and biasPEOM with $t_p = 10, 50,$ and 100 ms) consecutively before switching to the next pressure. For each particle and pressure, two PRRM curves were acquired, as well as at least 20 repetitions of each other method. The resulting data for the PRRM were evaluated according to the standard procedure,[17] and the corresponding results are shown in Fig. 4. For the other methods, the corresponding fit function (see Sec. II C) was fitted to the data using a nonlinear least squares algorithm.

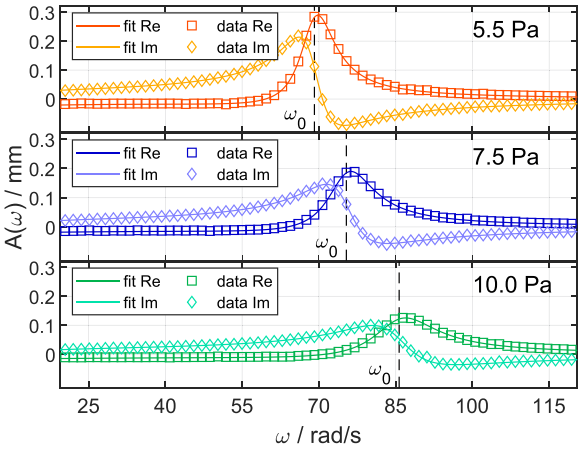

FIG. 4. Exemplary PRRM resonance curves for varying pressure; the complex amplitude $A(\omega)$ is plotted against the driving angular frequency ω. The data points and the corresponding fit are shown for real and imaginary parts, respectively. One can easily see that the eigenfrequency ω_0 shifts toward higher frequencies with rising pressure, and that the resonance peak broadens, which means that γ also increases with pressure.

The position data were then translated from pixel to millimeters, using a calibration with a scale as mentioned in Sec. III. Exemplary curves for every method are shown in Fig. 5. The eigenfrequency ω_0 could then be computed from the damping γ and the resonance frequency ω_d using Eq. (17). Thus, these results are directly comparable to those of the PRRM.

IV. RESULTS

A. Statistical comparison

The results for ω_0 and γ are statistically analyzed and compared to the PRRM results. The ratio between each method's results and the corresponding PRRM result is calculated and shown in Fig. 6. This normalization to the results of the PRRM is needed to eliminate the influence of the particle size distribution, as the particle radius a affects the particle charge and damping (see Sec. II). This size distribution stems from the small uncertainty with which the microparticles are produced by the manufacturer; see Sec. III for the exact numbers. The same information as in Fig. 6 is presented in Table I to show the exact numbers. In the following, it is important to differentiate the terms accuracy and precision: accuracy is the ability to obtain the true value of the measured quantity, which we assume the PRRM value to be, while precision describes the magnitude of the uncertainty arising while measuring the quantity.

The (relative) systematic deviation R_{sys} presented in Table I is (for a given method and pressure) given as

$$R_{sys} = \frac{\bar{\gamma} - \gamma_{PRRM}}{\gamma_{PRRM}}, \tag{19}$$

where $\bar{\gamma}$ is the mean value a given method yields at a given pressure. R_{sys} is used as a measure for the accuracy of the method. On the other hand, the relative statistical uncertainty R_{stat} measures the precision of a method and is given by

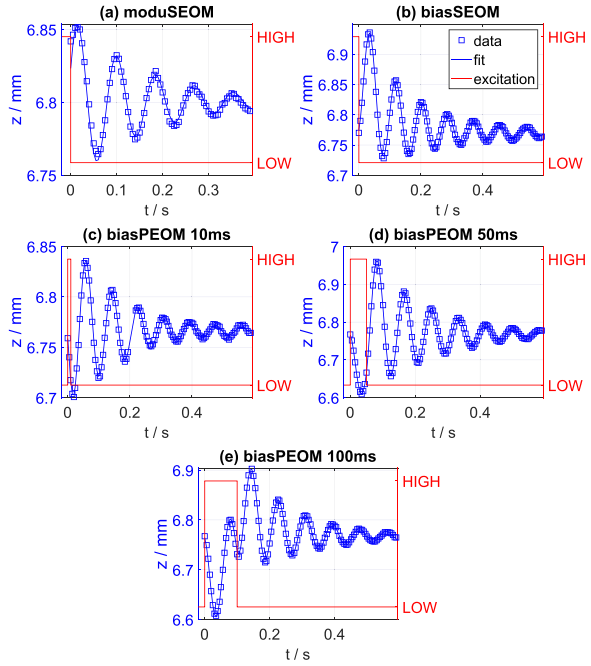

FIG. 5. Exemplary particle position data (blue squares) with fitted model function (blue line) for the different measurement types. All curves were recorded at 7.5 Pa. The excitation signal is also plotted in red. LOW and HIGH mean the RF power in the modulated case [(a)] and the external bias voltage in the bias cases [(b)–(e)].

$$R_{\mathrm{stat}} = \frac{\sigma_\gamma}{\gamma_{\mathrm{PRRM}}}. \tag{20}$$

σ_γ is the standard deviation of all values the given method yields at a given pressure. Both these values are first determined for each given combination of pressure, method, and individual particle and then averaged over all individual particles. The corresponding values of R_{sys} and R_{stat} for ω_0 are calculated in the same way. Generally, the uncertainty for ω_0 is about one order of magnitude smaller than that of γ. All methods but the moduSEOM (which overestimates ω_0 by circa 4%) are capable of reproducing the PRRM result for ω_0 very precisely (with deviations from the PRRM reference of at most 0.5%). The quality of the results seems to also be not dependent on the pressure. As a first finding, all bias methods deliver extremely accurate results for ω_0, with the 50 ms-biasPEOM offering the best precision, with uncertainties of about 0.2%. The overall picture is similar for γ: the moduSEOM overestimates γ significantly. However, the biasSEOM and the 100 ms-biasPEOM underestimate γ by ca. 7%. The 10- and 50 ms-biasPEOM are accurate with a deviation from the PRRM values of $\leq 2\%$. Of those two, the 50 ms-variant is decidedly more precise. This is likely due to the worse signal-to-noise ratio in the data from the 10 ms-biasPEOM because of the lower oscillation amplitude.

To further assess the plausibility of these results, Monte Carlo simulations using synthetic data[36] for the 50 ms-PEOM were conducted, and predicted uncertainties on the order of 0.1% for ω_0 and

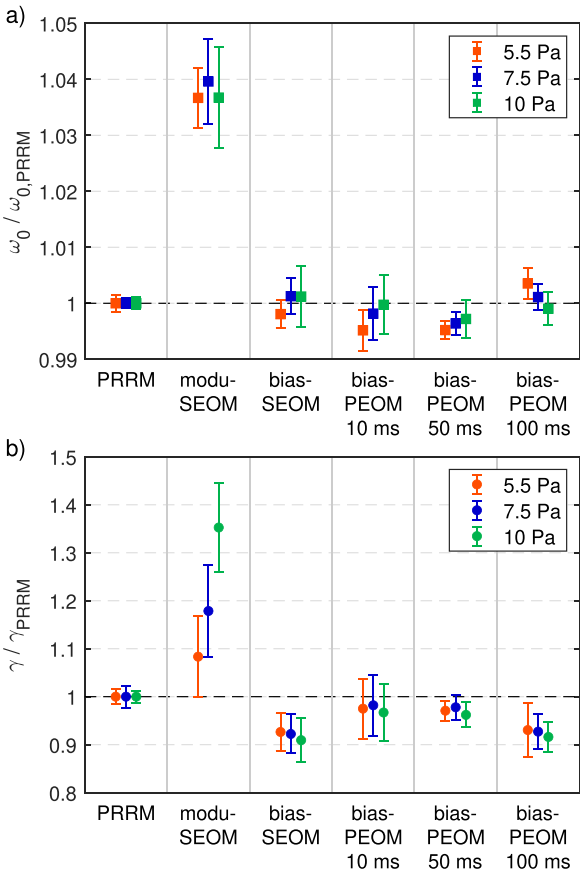

FIG. 6. Comparison of the different methods' results for (a): ω_0 and (b): γ, respectively, to those of the PRRM. The ratio between each method's result and the PRRM result is displayed for the different methods and operating pressures. The values are each the average over the multiple particles used and the repetitions of the respective method for each individual particle, while the error bars show the corresponding standard deviation. Note that the y-axes have a different scaling.

1% for γ, agreeing well with the experimental results. These theoretical uncertainties are extremely close to those of the PRMM also acquired via synthetic data.[18]

Interestingly, the moduSEOM results for γ seem to be dependent on the pressure, from which the rest of the methods are largely independent. There are two possible explanations: first, the moduSEOM presumably produces more noise in the data by the strong perturbation of the plasma (especially in the relatively small plasma reactor) and has a slightly smaller oscillation amplitude than the bias methods. This unfavorable signal-to-noise makes the accurate determination of gamma difficult. Another reason lies in the concept of excitation via modulation itself: Meijaard *et al.*[26] stated that the stepwise method (corresponding to the moduSEOM in this work) is sensitive to the delayed charging effect (DCE) proposed by Pustylnik *et al.*[37] The DCE basically adds another term to the Epstein friction coefficient in Eq. (2),

Physics of Plasmas ARTICLE pubs.aip.org/aip/pop

TABLE I. Results of the statistical analysis, equivalent to the data in Fig. 6. For each method and pressure, the relative systematical deviation R_{sys} and statistical uncertainty R_{stat} are presented. R_{sys} corresponds to the vertical position of the data points in Fig. 6, while R_{stat} corresponds to the size of the error bars.

ω_0	5.5 Pa		7.5 Pa		10 Pa	
Method	R_{sys}	R_{stat}	R_{sys}	R_{stat}	R_{sys}	R_{stat}
	in %					
PRRM	…	±0.16	…	±0.09	…	±0.10
mSEOM	+3.7	±0.54	+4.0	±0.75	+3.7	±0.90
bSEOM	−0.19	±0.24	+0.13	±0.32	+0.12	±0.54
bPEOM 10 ms	−0.48	±0.36	−0.18	±0.48	−0.03	±0.53
bPEOM 50 ms	−0.48	±0.16	−0.36	±0.21	−0.28	±0.34
bPEOM 100 ms	+0.35	±0.28	+0.11	±0.23	−0.10	±0.30
γ	5.5 Pa		7.5 Pa		10 Pa	
Method	R_{sys}	R_{stat}	R_{sys}	R_{stat}	R_{sys}	R_{stat}
	in %					
PRRM	–	±1.5	–	±2.3	–	±1.3
mSEOM	+8.3	±8.5	+18	±9.6	+35	±9.3
bSEOM	−7.4	±3.9	−7.8	±4.1	−9.1	±4.6
bPEOM 10 ms	−2.5	±6.3	−1.8	±6.3	−3.3	±6.0
bPEOM 50 ms	−2.9	±2.1	−2.2	±2.7	−3.8	±2.6
bPEOM 100 ms	−7.0	±5.6	−7.3	±3.7	−8.4	±3.1

$$\gamma = \gamma_{eps} + \gamma_{DCE}. \tag{21}$$

This term γ_{DCE} is, among others, dependent on the pressure. Should this effect be of non-negligible magnitude, it could explain why γ is measured as so much higher by the moduSEOM than the other methods, as well as its apparent pressure dependence.

B. Optimal pulse duration

Regarding the criterion in Eq. (18), it can be said that the 50 ms-biasPEOM, satisfying the criterion, indeed delivers the highest overall oscillation amplitude using the same excitation amplitude and thus the best signal-to-noise ratio. The criterion for the pulse duration is therefore regarded as reasonable. Looking at Fig. 5(e), one can see that a very complicated trajectory arises when the criterion is grossly violated and the excitation is in antiphase with the particle oscillation. Such trajectories can be harder to evaluate or yield less precise results. It should be noted that to fulfill the criterion, an estimate of ω_d is needed. This can be, for example, based on a very coarse manual frequency sweep with a sinusoidal excitation and a high exposure time of the camera, similar to the classical resonance method (RM) or simply from experience.

C. PEOM supporting PRRM, access to plasma resistance R_p

Another advantage of the bias methods is that they also provide access to the plasma resistance R_p via the fit parameter ν, which is usually difficult to obtain accurately with the PRRM due to the weak dependency of the resonance curve on it. This, combined with the time resolution (1–2 s per measurement) of these methods, allows for another way of monitoring the plasma state, e.g., to ensure the reproducibility of experiments. It would also be possible to use the PEOM as a quick diagnostic before conducting a PRRM measurement: The results for γ and ω_0 would help define the frequency range of the PRRM measurement, and the result for ν could be used to improve the PRRM fit: the PRRM fit contains the fit parameter ω_g as the critical frequency of the filter in the frequency domain. This parameter is, due to the aforementioned weak effect on the shape of the resonance curve, difficult to determine via a PRRM fit. ω_g is related to ν as

$$\omega_g = \nu \cdot \left(1 + \frac{2C_2}{C_1}\right). \tag{22}$$

Thus, from the PEOM result for ν, one can get a very good estimate for the parameter ω_g in the PRRM fit. It could be incorporated as a fixed value for ω_g, as a well-defined start value, or to set bounds for the fit parameter.

D. Determination of the charge-to-mass ratio q_d/m

Equation (3) allows us to determine the charge-to-mass ratio q_d/m of a dust particle from its eigenfrequency ω_0 when the absolute charge density ρ_q in the sheath is known. Using typical values (ion density $n_i = 1.2 \times 10^{14}\,\mathrm{m}^{-3}$, electron duty factor $n_e/n_i = 0.3$), the charge density is $\rho_q = 8.4 \times 10^{13}\,\mathrm{e/m^3} \approx 1.35 \times 10^{-5}\,\mathrm{C/m^3}$. Table II shows the resulting charge-to-mass ratio and the charge of an exemplary particle ($2a = 7.38\,\mu$m) for different discharge pressures.

E. Final assessment

Taking into account all these findings, the biasPEOM is deemed the optimal method among those examined in this work. This is attributed to the following qualities:

- The excitation with an additional bias voltage is only a very small distortion of the plasma (especially in comparison to the excitation via an RF power modulation).
- The rectangle-pulse shape of the excitation signal is also beneficial, as choosing a pulse duration according to the criterion in Eq. (18) further aids in obtaining low-noise data for the particle trajectories.
- The incorporation of the filter characteristics into the fit model yields an extremely good agreement between data and fit model and also allows to gain access to the plasma resistance R_p.
- As a result of the last three arguments, the biasPEOM is comparable to the PRRM in terms of precision and reproduces its results with a

TABLE II. Variation of the charge-to-mass ratio and the charge of an exemplary ($2a = 7.38\,\mu$m) particle with the discharge pressure. The values for ω_0 from the PEOM measurements were used. The mass density of SiO_2, $\rho_m = 1850\,\mathrm{kg/m^3}$ is needed to compute the particle charge.

Pressure p/Pa	Eigenfrequency $\omega_0/\mathrm{rad \cdot s^{-1}}$	Charge-to-mass ratio $\frac{q_d}{m}/10^{-22}\,\mathrm{Ckg^{-1}}$	Charge q_d/e
5.50	68.48	4.94	7560
7.50	75.46	6.00	9180
10.0	85.17	7.65	11 700

high accuracy. It also outperforms the biasSEOM with its slightly simpler step-excitation in regard to the uncertainties in γ.

V. CONCLUSION

A high-precision method, the biasPEOM, for the determination of ω_d and γ of a trapped microparticle was developed, thoroughly tested, and compared with existing, similar methods like the moduSEOM (stepwise excitation). The rectangle-pulse signal shape and the excitation with a bias voltage in conjunction with the incorporation of the filter network in the model allow for a very precise analysis of the data. The high time resolution potentially allows for better monitoring of time-dependent processes, for example, the etching of polymer microparticles in argon or argon–oxygen plasmas. Additionally, the ability to determine the plasma resistance R_p can be used to monitor the plasma state. It also qualifies as a supplement to PRRM measurements. Furthermore, the biasPEOM operates with precision comparable to the PRRM and reproduces its results reliably with good accuracy, also justifying the use as a stand-alone diagnostic for ω_0 (via ω_d) and γ that is much faster than the PRRM.

ACKNOWLEDGMENTS

We gratefully acknowledge financial support from the German Research Foundation (DFG) in Project GR1608/9-1 (Project No. 443791209).

AUTHOR DECLARATIONS

Conflict of Interest

The authors have no conflicts to disclose.

Author Contributions

Armin Mengel: conceptualization (equal); data curation (lead); formal analysis (lead); investigation (lead); methodology (equal); project administration (equal); software (lead); validation (lead); visualization (lead); writing—original draft (lead); and writing—review and editing (equal). **Maurice Pascal Artz:** formal analysis (supporting) and investigation (supporting). **Franko Greiner:** conceptualization (equal); funding acquisition (lead); methodology (equal); project administration (lead); resources (lead); software (supporting); supervision (lead); and writing—review and editing (equal).

DATA AVAILABILITY

The data that support the findings of this study are available from the corresponding author upon reasonable request.

REFERENCES

[1]A. Melzer, *Physics of Dusty Plasmas- An Introduction*, 1st ed. (Springer Nature Switzerland AG, 2019).
[2]A. Piel, *Plasma Physics—An Introduction to Laboratory, Space, and Fusion Plasmas*, 2nd ed. (Springer, 2017).
[3]H. R. Maurer, V. Schneider, M. Wolter, R. Basner, T. Trottenberg, and H. Kersten, "Microparticles as plasma diagnostic tools," Contrib. Plasma Phys. **51**, 218–227 (2011).
[4]V. Schneider and H. Kersten, "On the use of optically trapped dust particles as micro-probes in process plasmas," Probl. At. Sci. Technol. **83**(1), 164–167 (2013).
[5]V. Schneider and H. Kersten, "An optical trapping system for particle probes in plasma diagnostics," Rev. Sci. Instrum. **89**, 103505 (2018).
[6]J. Schleitzer, V. Schneider, and H. Kersten, "Investigations of the sheath in a dual-frequency capacitively coupled rf discharge by optically trapped microparticles," Phys. Plasmas **28**, 083506 (2021).
[7]E. B. Tomme, B. M. Annaratone, and J. E. Allen, "Damped dust oscillations as a plasma sheath diagnostic," Plasma Sources Sci. Technol. **9**, 87–96 (2000).
[8]V. Schneider, T. Trottenberg, I. Teliban, and H. Kersten, "An experiment for the investigation of forces on microparticles in ion beams," Rev. Sci. Instrum. **81**, 013503 (2010).
[9]T. Trottenberg, A. Spethmann, V. Schneider, M. Stahl, M. Giesenhagen, and H. Kersten, "Non-electrostatic diagnostics for ion beams," Contrib. Plasma Phys. **52**, 584–592 (2012).
[10]H. Maurer, R. Basner, and H. Kersten, "Measuring the temperature of microparticles in plasmas," Rev. Sci. Instrum. **79**, 093508 (2008).
[11]J. Carstensen, F. Greiner, and A. Piel, "Determination of dust grain charge and screening lengths in the plasma sheath by means of a controlled cluster rotation," Phys. Plasmas **17**, 083703 (2010).
[12]H. Thomas, G. E. Morfill, V. Demmel, J. Goree, B. Feuerbacher, and D. Möhlmann, "Plasma crystal: Coulomb crystallization in a dusty plasma," Phys. Rev. Lett. **73**, 652 (1994).
[13]J. H. Chu and I. Lin, "Direct observation of Coulomb crystals and liquids in strongly coupled rf dusty plasmas," Phys. Rev. Lett. **72**, 4009 (1994).
[14]Y. Hayashi and K. Tachibana, "Observation of Coulomb-crystal formation from carbon particles grown a methane plasma," Jpn. J. Appl. Phys., Part 2 **33**, L804 (1994).
[15]A. Melzer, T. Trottenberg, and A. Piel, "Experimental determination of the charge on dust particles forming Coulomb lattices," Phys. Lett. A **191**, 301 (1994).
[16]A. Homann, A. Melzer, and A. Piel, "Measuring the charge on single particles by laser-excited resonances in plasma crystals," Phys. Rev. E **59**, R3835–R3838 (1999).
[17]H. Jung, F. Greiner, O. H. Asnaz, J. Carstensen, and A. Piel, "Resonance methods for the characterization of dust particles in plasmas," J. Plasma Phys. **82**, 615820301 (2016).
[18]J. Carstensen, H. Jung, F. Greiner, and A. Piel, "Mass changes of microparticles in a plasma observed by a phase-resolved resonance method," Phys. Plasmas **18**, 033701 (2011).
[19]H. Jung, F. Greiner, O. H. Asnaz, J. Carstensen, and A. Piel, "Exploring the wake of a dust particle by a continuously approaching test grain," Phys. Plasmas **22**, 053702 (2015).
[20]O. H. Asnaz, H. Jung, F. Greiner, and A. Piel, "Charging of an irregularly shaped particle in the sheath of an rf plasma," Phys. Plasmas **25**, 073702 (2018).
[21]O. H. Asnaz, H. Jung, F. Greiner, and A. Piel, "Size and density evolution of a single microparticle embedded in a plasma," Phys. Plasmas **24**, 083701 (2017).
[22]F. Wieben, J. Schablinski, and D. Block, "Generation of two-dimensional binary mixtures in complex plasmas," Phys. Plasmas **24**, 033707 (2017).
[23]S. Wohlfahrt, C. Wirtz, and D. Block, "Non-linear etch process of MF particles embedded in an rf plasma with oxygen admixture," Phys. Plasmas **29**, 123702 (2022).
[24]N. Kohlmann, F. Wieben, O. H. Asnaz, D. Block, and F. Greiner, "High-precision *in-situ* size measurements of single microparticles in an RF plasma," Phys. Plasmas **26**, 053701 (2019).
[25]L. Schepers, J. Beckers, and W. L. IJzerman, "Determination of microparticle characteristics in an etching plasma," Contrib. Plasma Phys. **58**, 985–994 (2018).
[26]P. Meijaard, T. J. A. Staps, and J. Beckers, "Step-wise excitation for the determination of the resonance frequency of a microparticle confined in a low pressure plasma," Phys. Plasmas **28**, 083502 (2021).
[27]J. Kong, T. W. Hyde, B. Harris, K. Qiao, and J. Carmona-Reyes, "Measurement of the vertical nonuniformity of the plasma sheath in a complex plasma," IEEE Trans. Plasma Sci. **37**, 1620–1625 (2009).
[28]Z. Zhang, K. Qiao, J. Kong, L. Matthews, and T. Hyde, "Simple method to measure the interaction potential of dielectric grains in a dusty plasma," Phys. Rev. E **82**, 036401 (2010).
[29]O. Havnes, T. K. Aanesen, and F. Melandsù, "On dust charges and plasma potentials in a dusty plasma with dust size distribution," J. Geophys. Res. **95**, 6581–6585, https://doi.org/10.1029/JA095iA05p06581 (1990).
[30]A. Petersen, O. H. Asnaz, B. Tadsen, and F. Greiner, "Decoupling of dust cloud and embedding plasma for high electron depletion in nanodusty plasmas," Commun. Phys. **5**, 308 (2022).

Physics of Plasmas ARTICLE pubs.aip.org/aip/pop

[31]P. S. Epstein, "On the resistance experienced by spheres in their motion through gases," Phys. Rev. **23**, 710 (1924).
[32]C. Zafiu, A. Melzer, and A. Piel, "Nonlinear resonances of particles in a dusty plasma sheath," Phys. Rev. E **63**, 066403 (2001).
[33]Ş. S. Bayin, *Mathematical Methods in Science and Engineering* (John Wiley & Sons, Ltd, Hoboken, 2006).
[34]A. Omran and B. Newman, "Analytical response for the prototypic nonlinear mass-spring-damper system," in *ASME 10th Biennial Conference on Engineering Systems Design and Analysis* (ASMEDC, Istanbul, Turkey, 2010), Vol. 5, pp. 43–52.
[35]National Instruments, see https://www.ni.com/en-us/shop/labview.html for "What is LabVIEW? Graphical Programming for Test & Measurement."
[36]W. H. Press, S. A. Teukolsky, W. A. Vetterling, and B. P. Flannery, *Numerical Recipes: The Art of Scientific Computing*, 3rd ed. (Cambridge University Press, Cambridge, 2007).
[37]M. Y. Pustylnik, N. Ohno, S. Takamura, and R. Smirnov, "Modification of the damping rate of the oscillations of a dust particle levitating in a plasma due to the delayed charging effect," Phys. Rev. E **74**, 046402 (2006).

Physics of Plasmas ERRATUM pubs.aip.org/aip/pop

Erratum: "Pulse excited oscillation: A new high-precision excitation method for the charge-to-mass ratio determination of microparticles in plasma and comparison to step-wise excitation and the phase-resolved resonance method" [Phys. Plasmas 30, 123704 (2023)]

Cite as: Phys. Plasmas **31**, 129902 (2024); doi: 10.1063/5.0247530
Submitted: 7 November 2024 · Accepted: 8 November 2024 ·
Published Online: 17 December 2024

Armin Mengel,[a] Maurice Artz,[b] and Franko Greiner[c]

AFFILIATIONS

Institute of Experimental and Applied Physics, Kiel University, 24118 Kiel, Germany

[a]**Author to whom correspondence should be addressed:** mengel@physik.uni-kiel.de
[b]**Electronic mail:** stu209234@mail.uni-kiel.de
[c]**Also at:** Kiel Nano, Surface and Interface Science KiNSIS, Kiel University, Germany.
Electronic mail: greiner@physik.uni-kiel.de

https://doi.org/10.1063/5.0247530

In our recent publication[1] published on December 15, 2023, an error occurred. Due to a missing factor, $2m$, the neutral drag force was incorrectly introduced in the text above Eq. (1), in the sentence starting with "In motion, the particle's…" on page 2, Sec. II A. It should have been $F_{\mathrm{nd}} = -2m\gamma\dot{z}$ instead of $F_{\mathrm{nd}} = -\gamma\dot{z}$. The quality and truth of the rest of the paper are unaffected by this, but this could have produced confusion when compared to the equation of motion in Eq. (2).

[1]A. Mengel, M. Artz, and F. Greiner, "Pulse excited oscillation: A new high-precision excitation method for the charge-to-mass ratio determination of microparticles in plasma and comparison to stepwise excitation and the phase-resolved resonance method," Phys. Plasmas **30**, 123704 (2023).

PHYSICAL REVIEW LETTERS 133, 185301 (2024)

Evidence of Different Charging Behavior of Conductive and Dielectric Materials in Low-Temperature Plasmas and a New Diagnostic for Low-Energy Electron Absorption

Armin Mengel,[1,*] Franz X. Bronold,[2,†] and Franko Greiner[1,3,‡]
[1]Institute of Experimental and Applied Physics, Kiel University, 24118 Kiel, Germany
[2]Institute of Physics, University Greifswald, 17489 Greifswald, Germany
[3]Kiel Nano, Surface and Interface Science KiNSIS, Kiel University, Germany

(Received 25 April 2024; revised 31 July 2024; accepted 25 September 2024; published 28 October 2024)

In any physical system where a surface is hit by electrons, the sticking probability s of the electrons is a central parameter governing, for example, the charging of the surface. For dielectrics, it could previously only be measured for high energies (> 100 eV), while it is well-known for metals even at energies of only a few eV. Recent theoretical investigations concerning dielectrics such as silica predict values for s significantly below 1. With precision charge measurements on microparticles in the sheath of a low-pressure plasma, a difference in charge between silica and gold-coated particles is found, challenging the long-standing assumption in dusty plasma physics that dielectric and metallic particles charge in the same way for the first time. Based on the measured charging difference, the low-energy sticking coefficient of silica is obtained, validating the theoretical predictions and offering a new diagnostic for the otherwise quasi-inaccessible low-energy electron sticking of dielectric materials.

DOI: 10.1103/PhysRevLett.133.185301

The phenomenon of static electricity has been known to humankind since antiquity, with the first documented observation often attributed to Thales of Miletus around 600 BCE [1]. While much has been learned about the interaction of charged objects since then, charging processes are, as of yet, not nearly fully understood. Even the most mundane charging process, the triboelectric effect that was already known to Thales, can still only be explained on a very basic level [2]. For most modern applications of electricity in general, the focus of research was on the discharging dynamics of the respective objects, while charging processes often proved difficult to describe accurately. A prominent example for such an application are plasmas, in particular, low-temperature plasmas (LTPs) with electron temperatures $T_e \leq 10$ eV, which are the basis for manufacturing a vast portion of modern technology [3]. While the dynamics and interactions of their constituents (mainly electrons and ions) are quite well understood, the interaction of LTPs with surfaces proved to be a very complex topic. One of the most basic and central questions in this context is how an electron from the plasma hitting the surface in question behaves. Does it enter the surface and stay there, charging the surface in the process, or is it reflected? Or does it enter but release other electrons from the surface instead? These basic processes are usually quantified via the electron sticking coefficient s and the secondary electron emission coefficient δ, which are material constants of the surface. For high electron energies ($E_e > 100$ eV), these can be measured using an electron beam directed at a target in ultrahigh vacuum, given a degree of conductivity of the target material [4,5]. For highly conductive materials like noble metals, these measurements can even be carried out for electron energies down to the order of the Fermi energy. However, the plasma-facing surfaces in many technologically relevant LTP configurations, like microwave discharges and dielectric barrier discharges, are dielectrics, e.g., MgO or Al_2O_3. The performance of plasma catalysis reactors, for example, depends on the buildup of surface charges on the electrodes [6,7]. The quality of electrical probe measurements also depends on the electron absorption at its surface [8]. Furthermore, the accuracy of simulations of plasma systems benefits from knowledge of the sticking and secondary electron emission at the surfaces involved.

Despite this clear need for the low-energy sticking coefficients of dielectrics, no successful measurements have been reported besides an older, inconclusive study [9]. A recent theoretical approach predicts values for the low-energy electron sticking of SiO_2, MgO, and Al_2O_3 significantly below 1 [10]. In contrast, the electron sticking of metal surfaces at such energies is nearly 1. Because of the lack of suitable experimental techniques, low-energy sticking coefficients of electrode materials can only be indirectly determined by matching measured plasma density profiles to simulations with varying s [11]. A related

*Contact author: mengel@physik.uni-kiel.de
†Contact author: bronold@uni-greifswald.de
‡Contact author: greiner@physik.uni-kiel.de

approach is able to yield the ion-induced secondary electron emission coefficient [12].

The goal of this Letter is to establish a new measurement scheme that offers an opportunity to measure the low-energy sticking coefficient of silica as an example dielectric. To this end, single, micrometer-sized spheres made of silica and gold-coated polymer are introduced into a low-pressure plasma with electron energies on the order of 5 eV, forming a "dusty plasma." In the study of dusty plasmas, the charging difference between metallic and dielectric particles has been an open question for a long time, which can also be answered using the findings of this Letter. The sticking coefficient $\tilde{s}_{SiO_2}$ of silica is then derived from the charging difference between gold and silica.

In a typical laboratory dusty plasma situation [13,14], one or more usually spherical particles are confined in the sheath of a plasma. In contrast to astrophysical situations, where photoemission and secondary electron emission from high-energy primaries also play a role, the dominating particle charging mechanism is the collection of charges from the surrounding plasma. The balance between electron and ion current onto the particle determines the floating potential (or surface potential) Φ_f of the particle,

$$I_e(\Phi_f) + I_i(\Phi_f) = 0. \tag{1}$$

If the probability s for electron sticking is below 1, the electron current is attenuated and Φ_f differs from the perfect absorber case above. In essence, the floating potential of a particle is sensitive to the electron sticking probability at the surface, implying that there should also be a measurable difference in floating potential between particles with conducting and dielectric surfaces.

In this Letter, we aim to carve out that difference by measuring and comparing the charges of dielectric and metal-coated particles. The particle charge q is usually determined from a spherical capacitor model [13] and is proportional to both Φ_f and the particle radius a,

$$q = 4\pi\varepsilon_0 a\Phi_f. \tag{2}$$

Typical charges of a microparticle with 10 μm diameter are of the order of -10^3 to -10^4 elementary charges. The electrical field in the lower sheath of the plasma exerts an upward pointing force on the particle, compensating gravity and vertically confining the particle in a locally harmonic potential at an equilibrium levitation height. Other forces on the particle can be neglected under these circumstances, as there is no temperature gradient present to enable thermophoresis, and the ion wind has been estimated to be negligible in comparison to gravity and electrical force (for details on these forces, see the textbook of Melzer [14]). Vertical oscillations of the particle can be excited electrically, whose eigenfrequency ω_0 contains the charge-to-mass ratio (q/m) of the particle as well as the absolute charge density ρ_q at the particle position,

$$\omega_0^2 = \frac{q}{m}\frac{\rho_q}{\varepsilon_0}. \tag{3}$$

From the initial proposal of such a resonance method [15], high-precision methods for the determination of the eigenfrequency of single microparticles have been developed. In this Letter, the phase-resolved resonance method (PRRM) [16] and the pulse excited oscillation method (PEOM) [17] are applied. These methods also yield the neutral gas friction coefficient γ, which is given by the model of Epstein [18] as

$$\gamma = \delta\frac{4}{\pi}\frac{p}{a\rho_m\hat{v}_{th,n}}. \tag{4}$$

The coefficient δ differentiates between specular and diffuse reflection of gas atoms or molecules at the particle surface and has been shown to be 1.44 ± 0.05 in the dusty plasma context [16]. Apart from the gas pressure p and the mean thermal velocity $\hat{v}_{th,n}$ of the gas atoms and molecules (which are assumed to be at room temperature), γ depends on the size and mean mass density ρ_m of the microparticle. The particle radius is independently measured *in situ* using images obtained with a long distance microscope (LDM), allowing for the calculation of the particle mass using Eq. (4). To access the floating potential, Eqs. (2) and (3) are combined into an auxiliary quantity η,

$$\eta := \frac{m\omega_0^2}{4\pi a} = \Phi_f(h)\rho_q(h). \tag{5}$$

This quantity links the otherwise inaccessible floating potential and sheath charge density to the measurable eigenfrequency, gas friction coefficient (via the mass m), and particle radius. Because of the spatially varying conditions [densities $n_e(h)$, $n_i(h)$ and mean energies $\bar{E}_e(h)$, $\bar{E}_i(h)$ of electrons and ions] in the sheath, both Φ_f and ρ_q are generally height-dependent. To circumvent the unknown dependency of the floating potential on the charge density in the sheath, a relative determination schema is used, which is as follows: η is measured for a series of particles with either dielectric or metallic surfaces. In this Letter, commercially available [19] microparticles were used: SiO_2 microspheres were used as dielectric particles, while gold-coated melamine formaldehyde particles were used as particles with a metallic surface. The coating thickness of a few 100 nm ensures that the particle has the surface properties of a metallic solid. Particles with nominal diameters in a range from 7.00 to 9.36 μm (SiO_2) and 5.95 to 11.87 μm (Au) were introduced into a capacitively coupled parallel plate discharge driven at radio frequency ($f_{rf} = 13.56$ MHz, $P_{rf} = 1.5$ W) in argon at 7.5 Pa. A schematic view of the setup, including the

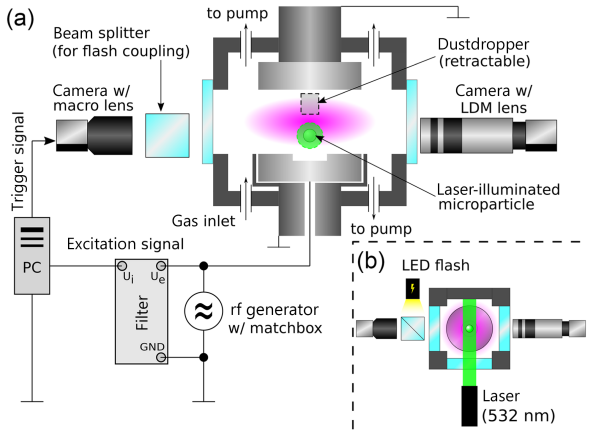

FIG. 1. Schematic setup as a side view (a) of a cut through the plasma chamber, and a top view (b) showing the optical setup. The lower electrode is driven, while the upper electrode is grounded. The confined microparticle is illuminated with a green laser ($\lambda = 532$ nm) and tracked using the macro lens during the PRRM and PEOM measurements. Trigger and excitation signals are generated with a computer interface, and the latter is coupled into the system via a filter network. For the size measurements with the LDM lens, the laser is turned off, and the particle is repeatedly illuminated with an LED flash coupled into the optical path via a beam splitter.

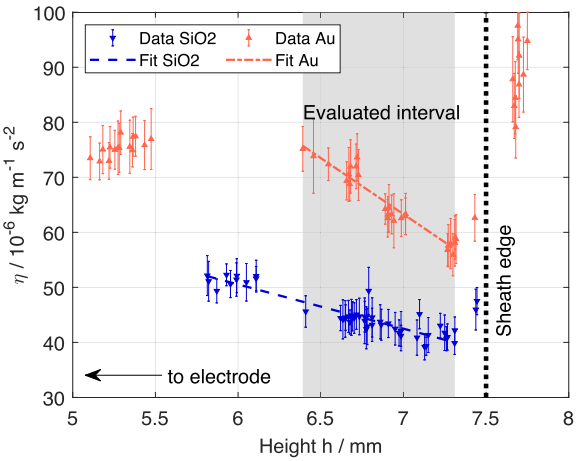

FIG. 2. Values for η obtained from the particle measurements as a function of levitation height h above the electrode. In addition to the particle data points, linear fits to the data are drawn as dashed (SiO_2 particles) and dash-dotted lines (Au particles). The evaluated interval is marked in gray. The evaluated interval only includes the region where linear fits to both datasets are justified simultaneously. The bold dotted black line designates the approximate sheath edge position as determined by the glow intensity of the plasma.

instruments required for PRRM, PEOM, and LDM is shown in Fig. 1. The particles were each introduced individually into the plasma at the same conditions (pressure, rf power, dc self-bias voltage). The relative fluctuations over the course of the measurements were $\pm 1.8\%$ for the self bias, $\pm 4.3\%$ for the rf amplitude, and $\pm 0.16\%$ for the pressure. In addition to the PRRM and PEOM measurements, multiple LDM images were taken, and the equilibrium levitation height h above the electrode was recorded. From these data, η was calculated for each particle and plotted over the levitation height of the particle in Fig. 2. From the η values for a SiO_2 and a Au particle levitating at the same height h, the ratio Y of the particles' floating potentials is produced, as the height-dependent charge density $\rho_q(h)$ drops out,

$$\frac{\eta_{SiO_2}(h)}{\eta_{Au}(h)} = \frac{\Phi_{f,SiO_2}(h)}{\Phi_{f,Au}(h)} =: Y(h). \tag{6}$$

However, only by chance two particles of different materials levitated at the exact same height, so $\eta(h)$ has to be interpolated via a linear fit. The evaluation is restricted to the region in the sheath where a linear trend is justifiable for the data of both materials (see the "evaluated interval" marked in Fig. 2). Thus, every η value from a particle in this height region can be compared against an interpolated value corresponding to a virtual particle of the respective other material levitating at the exact same height.

The resulting data for the floating potential ratio at identical charge density, Y, is displayed in Fig. 3, indicating values mainly in the range between 0.62 and 0.71. The apparent variation of Y with the height is attributed to its dependency on the vertically varying densities and mean energies of

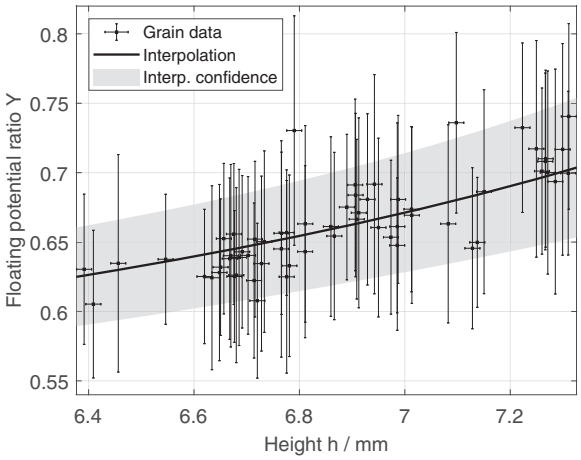

FIG. 3. Results for the floating potential ratio $Y = \Phi_{f,SiO_2}/\Phi_{f,Au}$ as a function of levitation height h. The distinct data points are calculated using the η value of each grain and the interpolated η of the other material at the same height h. The black line shows Y obtained from the ratio of both interpolated curves. The confidence interval for the latter is shaded in gray.

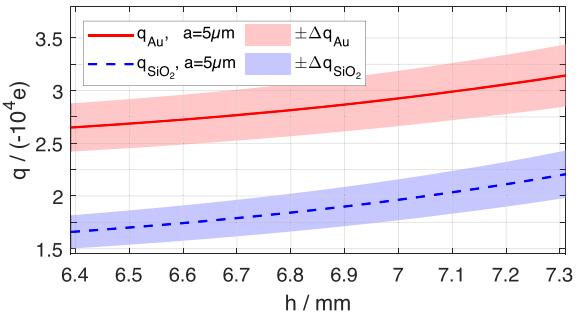

FIG. 4. Calculated charge q of hypothetical gold and silica particles depending on their position in the evaluated interval. The particles were assumed to have a radius of $a = 5$ μm. The shaded areas indicate the uncertainty of the result for q. The difference in charge despite the otherwise same conditions is clearly visible.

ions and electrons. This result clearly shows a significant difference between the charging of gold-coated and SiO_2 particles. If the charging was identical, the ratio of the floating potentials should be unity irrespective of the height. For a more demonstrative depiction of the charging difference, the charge of a 5 μm SiO_2 and gold microparticle is shown in Fig. 4. The needed $\rho_q(h)$ values were taken from experiment related particle-in-cell simulations using XPDP1 [20–22] modified for the Phelps argon collision cross sections [23]. For details on the simulation, see the Supplemental Material [24].

In the following, the results for Y shall be used for a closer look at the electron-surface interaction of silica. The most likely reason for the floating potential difference is the electron sticking probability at the SiO_2 surface, which is expected to be around 0.66 according to theoretical predictions [10] (see above). In contrast, effectively every electron sticks to a clean gold surface, as the electron emission yield there (which includes reflection) is close to zero for electron energies up to 5 eV [5]. A charging model for a dust particle in the plasma sheath is employed to obtain the angle- and energy-averaged sticking coefficient of SiO_2 from the floating potential ratio Y measured before. The sticking-corrected current balance formulated in [10] is rearranged to yield $\tilde{s}$ as a function of the reduced floating potential $x = -e\Phi_f/k_B T_e$,

$$\tilde{s}(x) = \frac{I_i(x)}{I_e(x)}. \tag{7}$$

Note that I_e is the electron current arriving at the particle surface before any sticking processes occur. I_e is expressed using Maxwell-Boltzmann distributed electron velocities, resulting in the term used in the orbital motion limit theory [28]. For the ions in the plasma sheath, the orbital motion limit approximation is not applicable. Instead, a refined model for I_i is used that considers the directed motion of

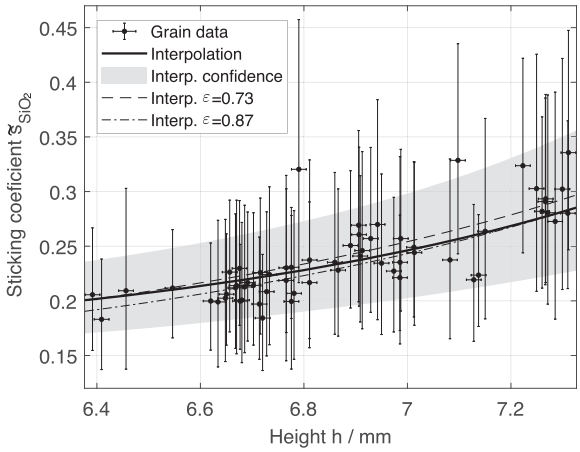

FIG. 5. Results for $\tilde{s}_{SiO_2}$ using Eq. (8) and simulation data for $\varepsilon(h)$. The data are obtained from the Y values shown in Fig. 3, and marked similarly. Data using Y from the comparison of both interpolation curves and constant values for ε corresponding to the minimum ($\varepsilon = 0.73$, dashed) and maximum ($\varepsilon = 0.87$, dash-dotted) ε in the evaluated interval are also displayed to show the influence of ε on the result for $\tilde{s}_{SiO_2}$.

the ions in the sheath electric field [24]. Solving Eq. (7) for x in the case $\tilde{s} = \tilde{s}_{Au} = 1$ (reasonably modeling gold as a perfect absorber) yields the reduced floating potential x_{Au} of a gold particle. Substituting $x = x_{Au}Y$ in Eq. (7) gives a formula for the determination of $\tilde{s}_{SiO_2}$ for the silica surfaces as a function of the measured floating potential ratio Y,

$$\tilde{s}_{SiO_2}(Y) = \frac{I_i(x_{Au}Y)}{I_e(x_{Au}Y)}. \tag{8}$$

The currents I_e and I_i depend on parameters such as the density and mass ratio of electrons and ions, the ion drift velocity, and the shape parameters of their velocity distributions [24]. These parameters (except for the mass ratio, which is $\mu = m_i/m_e = 7.28 \times 10^4$ for the argon plasma used here) are generally height-dependent and are obtained from the aforementioned particle-in-cell simulation with XPDP1. The most effective parameter is the density ratio $\varepsilon(h) = n_e(h)/n_i(h)$. Figure 5 shows the estimated sticking coefficient. In addition, the curve for two constant $\varepsilon(h)$ values (maximum and minimum value of ε in the evaluated interval) are shown. The effect of a height dependence of ε is marginal. The remaining height dependency is likely the result of the varying electron energy distribution over the range of the evaluated interval, as $\tilde{s}$ is generally dependent on the energy of the impinging electrons.

All uncertainties presented here are obtained from subsequent basic error propagation of the measured quantities (ω_0, γ, a, h) and δ from [16]. The radius determination contributed the largest relative uncertainty of all the measured quantities. The uncertainties for $\tilde{s}_{SiO_2}$ are obtained by

calculating $\tilde{s}_{SiO_2}(Y \pm \Delta Y)$. The uncertainty of the simulation data could not be exactly quantified, but the dependence of the evaluation on the simulation results is estimated based on a variation of ε. Over all evaluated particles, a mean value of $\tilde{s}_{SiO_2} = 0.239 \pm 0.037$ is obtained. The values from single particles are between $\tilde{s}_{SiO_2,min} = 0.183$ and $\tilde{s}_{SiO_2,max} = 0.336$, and the uncertainty of a single value is ± 0.069 on average. These results clearly indicate that the sticking coefficient of SiO_2 is decidedly lower than 1, and significantly different from that of gold at the same mean plasma electron energy.

It was shown for the first time that the floating potentials of dielectric (SiO_2) and metallic (gold) particles confined in the plasma sheath differ significantly, with a ratio $Y = \Phi_{f,SiO_2}/\Phi_{f,Au}$ of 0.62 to 0.71. This indicates a fundamentally different charging behavior of the two surface materials. By identifying the different electron sticking probabilities as the dominant cause for this difference, an estimation for the electron sticking coefficient $\tilde{s}_{SiO_2}$ of SiO_2 is made based on a charging model, simulation data, and the known value of $\tilde{s}_{Au}$. The electron sticking coefficient of SiO_2 for low electron energies is much smaller than 1 and also below the theoretical prediction of $\tilde{s}_{SiO_2} = 0.66$ [10]. The residual height dependence most likely stems from the dependence of $\tilde{s}_{SiO_2}$ on the varying electron energy in the plasma sheath and will be addressed in future work.

The treatment of dielectric surfaces as perfect absorbers at low electron energies is not justified. The experimental method presented here is a new, direct way of determining electron sticking coefficients, particularly for dielectric materials at electron energies below 10 eV. The resulting sticking coefficients are of importance in various technological applications, as indicated in the introduction of this Letter. Theoretical calculations of sticking coefficients will also benefit from the exact experimental determination.

Acknowledgments—A. M. and F. G. acknowledge the support from the Deutsche Forschungsgemeinschaft (DFG) in Project No. GR 1608/9-1 (Project No. 443791209). F. X. B. acknowledges support by the DFG through Project No. BR 1994/4-1 (Project No. 495729137). The authors would like to thank Peter Manz for his valuable comments, which enhanced the significance of the manuscript.

[1] D. Laertius and R. D. Hicks, *Lives of the Eminent Philosophers—Book I* (Harvard University Press, Cambridge, MA, 1925).

[2] S. Pan and Z. Zhang, Fundamental theories and basic principles of triboelectric effect: A review, Friction **7**, 2 (2019).

[3] K.-D. Weltmann, J. F. Kolb, M. Holub, D. Uhrlandt, M. Šimek, K. Ostrikov, S. Hamaguchi, U. Cvelbar, M. Černák, B. Locke, A. Fridman, P. Favia, and K. Becker, The future for plasma science and technology, Plasma Process. Polym. **16**, 1800118 (2019).

[4] A. Chvyreva and A. J. M. Pemen, Experimental investigation of electron emission from dielectric surfaces due to primary electron beam: A review, IEEE Trans. Dielectr. Electr. Insul. **21**, 2274 (2014).

[5] L. A. Gonzalez, M. Angelucci, R. Larciprete, and R. Cimino, The secondary electron yield of noble metal surfaces, AIP Adv. **7**, 115203 (2017).

[6] K. M. Bal, S. Huygh, A. Bogaerts, and E. C. Neyts, Effect of plasma-induced surface charging on catalytic processes: Application to CO_2 activation, Plasma Sources Sci. Technol. **27**, 024001 (2018).

[7] A. D. Lele, Y. Xu, and Y. Ju, Modelling the effect of surface charging on plasma synthesis of ammonia using DFT, Phys. Chem. Chem. Phys. **26**, 9453 (2024).

[8] V. I. Demidov, S. F. Adams, I. D. Kaganovich, M. E. Koepke, and I. P. Kurlyandskaya, Measurements of low-energy electron reflection at a plasma boundary, Phys. Plasmas **22**, 104501 (2015).

[9] C. J. Cook and W. J. Fredericks, Interaction of slow electrons with insulating crystals. I. Absorption coefficient for cleaved alkali halides; Experimental techniques, J. Appl. Phys. **32**, 860 (1961).

[10] F. X. Bronold and H. Fehske, Microscopic theory of electron absorption by plasma-facing surfaces, Plasma Phys. Controlled Fusion **59**, 014011 (2017).

[11] I. Korolov, A. Derzsi, Z. Donkó, E. Schüngel, and J. Schulze, The influence of electron reflection/sticking coefficients at the electrodes on plasma parameters in particle-in-cell simulations of capacitive radio-frequency plasmas, Plasma Sources Sci. Technol. **25**, 015024 (2016).

[12] C. Schulze, Z. Donkó, and J. Benedikt, A computationally assisted technique to measure material-specific surface coefficients in capacitively coupled plasmas based on characteristics of the ion flux-energy distribution function, Plasma Sources Sci. Technol. **31**, 105017 (2022).

[13] A. Piel, *Plasma Physics—An Introduction to Laboratory, Space, and Fusion Plasmas*, 2nd ed. (Springer, New York, 2017).

[14] A. Melzer, *Physics of Dusty Plasmas- An Introduction*, 1st ed. (Springer Nature, Switzerland AG, 2019).

[15] A. Melzer, T. Trottenberg, and A. Piel, Experimental determination of the charge on dust particles forming Coulomb lattices, Phys. Lett. A **191**, 301 (1994).

[16] H. Jung, F. Greiner, O. H. Asnaz, J. Carstensen, and A. Piel, Resonance methods for the characterization of dust particles in plasmas, J. Plasma Phys. **82**, 615820301 (2016).

[17] A. Mengel, M. Artz, and F. Greiner, Pulse excited oscillation: A new high-precision excitation method for the charge-to-mass ratio determination of microparticles in plasma and comparison to stepwise excitation and the phase-resolved resonance method, Phys. Plasmas **30**, 123704 (2023).

[18] P. S. Epstein, On the resistance experienced by spheres in their motion through gases, Phys. Rev. **23**, 710 (1924).

[19] microParticles GmbH, microParticles Onlineshop, https://www.microparticles-shop.de.

[20] J. P. Verboncoeur, M. V. Alves, V. Vahedi, and C. K. Birdsall, Simultaneous potential and circuit solution for 1d bounded plasma particle simulation codes, J. Comput. Phys. **104**, 321 (1993).
[21] V. Vahedi, G. DiPeso, C. K. Birdsall, M. A. Lieberman, and T. D. Rognlien, Capacitive RF discharges modelled by particle-in-cell Monte Carlo simulation. I. Analysis of numerical techniques, Plasma Sources Sci. Technol. **2**, 261 (1993).
[22] V. Vahedi, C. K. Birdsall, M. A. Lieberman, G. DiPeso, and T. D. Ronhlien, Capacitive RF discharges modelled by particle-in-cell Monte Carlo simulation. II. Comparisons with laboratory measurements of electron energy distribution functions, Plasma Sources Sci. Technol. **2**, 273 (1993).
[23] A. V. Phelps, The application of scattering cross sections to ion flux models in discharge sheaths, J. Appl. Phys. **76**, 747 (1994).
[24] See Supplemental Material at http://link.aps.org/supplemental/10.1103/PhysRevLett.133.185301 for details on the ion current model and the calculation of the sticking coefficient, and details on the XPDP1 simulation, which includes Refs. [25–27].
[25] M. Lampe, T. B. Röcker, G. Joyce, S. K. Zhdanov, A. V. Ivlev, and G. E. Morfill, Ion distribution function in a plasma with uniform electric field, Phys. Plasmas **19**, 113703 (2012).
[26] A. Piel, H. Jung, and F. Greiner, Molecular dynamics simulations of wake structures behind a microparticle in a magnetized ion flow. II. Effects of velocity spread and ion collisions, Phys. Plasmas **25**, 083703 (2018).
[27] F. W. Olver, *NIST Handbook of Mathematical Functions* (Cambridge University Press, Cambridge and New York and Melbourne, 2010).
[28] J. E. Allen, Probe theory—the orbital motion approach, Phys. Scr. **45**, 497 (1992).

Supplemental material for ,,Experimental evidence of different charging behavior of conductive and dielectric materials in low-temperature plasmas and a new diagnostic for low-energy electron absorption"

Armin Mengel[a],* Franz X. Bronold[b],† and Franko Greiner[a,c‡]
[a] *Institute of Experimental and Applied Physics, Kiel University, 24118 Kiel, Germany*
[b] *Institute of Physics, University Greifswald, 17489 Greifswald, Germany and*
[c] *Kiel Nano, Surface and Interface Science KiNSIS, Kiel University, Germany*
(Dated: November 1, 2024)

Appendix A: Ion velocity distribution and charging current for streaming ions in the plasma sheath

The determination of the floating potential of a microparticle trapped in the plasma sheath requires knowledge of the electron and ion currents onto the particle depending on its electrostatic surface potential. This in turn requires that the distribution function of the absolute value of the velocity of both species is known. The electrons can be modeled with a three-dimensional Maxwell-Boltzmann distribution, yielding the known result used in the OML theory[1–3]. While the classical OML theory assumes that the ions are following an isotropic Maxwell-Boltzmann distribution, this is not the case in the plasma sheath. The strong acceleration of the ions by the electric field $\vec{E}$ of the plasma sheath needs to be considered in the ion velocity distribution function (IVDF). While the ion velocity parallel to the electric field is often modeled as a beam, i.e. a narrow Maxwell-Boltzmann distribution shifted by a constant drift velocity v_{drift}, molecular dynamics simulations[4] show a much better agreement with the *constant collision cross section* model (constant-σ model) proposed by Lampe et al.[5]. The corresponding IVDF is a half-normal distribution with a scale parameter $\sigma_{\mathrm{HN}} = v_{\mathrm{drift}} \cdot \sqrt{\pi/2}$. The drift velocity in this case is given by

$$v_{\mathrm{drift}}^2 = \frac{2e|\vec{E}|}{\pi m_{\mathrm{i}} n_{\mathrm{n}} \bar{\sigma}}, \tag{A1}$$

where n_{n} is the neutral gas density and $\bar{\sigma}$ the constant collision cross section. A value of $\bar{\sigma} = 6 \times 10^{-19}\,\mathrm{m}^2$ was chosen by Lampe et al., and also matches the simulation results of this work. This distribution describes the ion velocity parallel to the electric field in the simulation used in this work very well. Choosing the direction of $\vec{E}$ as the z-axis, the velocity distribution in that direction is given as

$$f_{\mathrm{z}}(v_{\mathrm{z}}) = \frac{2}{\pi v_{\mathrm{drift}}} \cdot \Theta(v_{\mathrm{z}}) \cdot \exp\left(- \frac{v_{\mathrm{z}}^2}{\pi v_{\mathrm{drift}}^2} \right), \tag{A2}$$

with the Heaviside step function Θ. The ion velocities perpendicular to $\vec{E}$ (in x- and y-direction) are distributed thermally.

$$f_{\mathrm{x,y}}(v_{\mathrm{x,y}}) = \sqrt{\frac{m_{\mathrm{i}}}{2\pi k_{\mathrm{B}} T_{\mathrm{i},\perp}}} \cdot \exp\left(- \frac{m_{\mathrm{i}} v_{\mathrm{x,y}}^2}{2 k_{\mathrm{B}} T_{\mathrm{i},\perp}} \right). \tag{A3}$$

The temperature $T_{\mathrm{i},\perp}$ of ca. $0.056\,\mathrm{eV} = 650\,\mathrm{K}$ is obtained from the simulation data. Contrary to usual assumptions, this is about twice room temperature. Using these distribution functions, the distribution of the absolute value of the ion velocity can be calculated.

$$f_{\mathrm{i}}(v_{\mathrm{i}}) = \int_{\mathbb{R}^3} \delta(|\vec{v}| - v_{\mathrm{i}}) f_{\mathrm{x}}(v_{\mathrm{x}}) f_{\mathrm{y}}(v_{\mathrm{y}}) f_{\mathrm{z}}(v_{\mathrm{z}})\, d^3\vec{v}, \tag{A4}$$

with $\vec{v} = \left(v_{\mathrm{x}}, v_{\mathrm{y}}, v_{\mathrm{z}}\right)$. Inserting Eqs. (A2) and (A3) and solving the integral in spherical coordinates yields

$$f_{\mathrm{i}}(v_{\mathrm{i}}) = \frac{4A\sqrt{B}}{\sqrt{\pi}\sqrt{A-B}} \cdot v_{\mathrm{i}} \cdot e^{-B v_{\mathrm{i}}^2} \cdot D_+\left(\sqrt{A-B} \cdot v_{\mathrm{i}}\right), \tag{A5}$$

with $A = m_{\mathrm{i}}/(2k_{\mathrm{B}}T_{\mathrm{i},\perp})$, $B = (\pi v_{\mathrm{drift}}^2)^{-1}$ and D_+ is the *Dawson* function[6].
The total ion current onto the microsphere is then calculated as

$$I_{\mathrm{i}} = n_{\mathrm{i}} e \int_0^\infty \sigma_{\mathrm{c}}(v_{\mathrm{i}}) v_{\mathrm{i}} f_{\mathrm{i}}(v_{\mathrm{i}}) dv_{\mathrm{i}}. \tag{A6}$$

Here, $\sigma_{\mathrm{c}}(v_{\mathrm{i}}) = \pi a^2[1 - 2e\Phi/(m_{\mathrm{i}} v_{\mathrm{i}}^2)]$ is the charge collection cross section of the spherical dust particle. The resulting ion current is

$$I_{\mathrm{i}}(\Phi) = \pi n_{\mathrm{i}} e a^2 \frac{2\sqrt{\beta}}{1-\beta} \sqrt{\frac{8k_{\mathrm{B}}T_{\mathrm{i},\perp}}{\pi m_{\mathrm{i}}}} \times \left[\frac{I_1\left(\frac{1}{1-\beta}\right)}{1-\beta} - I_2\left(\frac{1}{1-\beta}\right) \frac{e\Phi}{k_{\mathrm{B}}T_{\mathrm{i},\perp}} \right]. \tag{A7}$$

The parameter $\beta = B/A = 2k_{\mathrm{B}}T_{\mathrm{i},\perp}/(\pi m_{\mathrm{i}} v_{\mathrm{d}}^2)$ is the ratio between the thermal energy of the ions perpendicular to $\vec{E}$ and the kinetic energy corresponding to their directed motion parallel to $\vec{E}$. The coefficients $I_1(\alpha)$ and $I_2(\alpha)$ are integral expressions, which are calculated numerically:

$$I_1(\alpha) = \int_0^\infty t^2 e^{-(\alpha-1)t^2} D_+(t)\, dt,$$
$$I_2(\alpha) = \int_0^\infty e^{-(\alpha-1)t^2} D_+(t)\, dt. \tag{A8}$$

* mengel@physik.uni-kiel.de
† bronold@uni-greifswald.de
‡ greiner@physik.uni-kiel.de

This expression can then be used in the calculation of the sticking coefficient $\tilde{s}$ of SiO_2. The expression for $\tilde{s}(x)$ (see Eq. (7) in the main publication) then reads

$$\tilde{s}(x) = \frac{e^x}{\varepsilon\sqrt{\mu\bar{\tau}}}\frac{2\sqrt{\beta}}{1-\beta}\left[\frac{I_1\left(\frac{1}{1-\beta}\right)}{1-\beta} + I_2\left(\frac{1}{1-\beta}\right)\cdot\bar{\tau}x\right] \quad \text{(A9)}$$

or, in a more compact form,

$$\tilde{s}(x) = \frac{e^x}{\varepsilon\sqrt{\mu\bar{\tau}}}\Big[J_1(\beta) + J_2(\beta)\cdot\bar{\tau}x\Big], \quad \text{(A10)}$$

where

$$J_1(\beta) = \frac{2\sqrt{\beta}}{(1-\beta)^2}\cdot I_1\left(\frac{1}{1-\beta}\right),$$
$$J_2(\beta) = \frac{2\sqrt{\beta}}{1-\beta}\cdot I_2\left(\frac{1}{1-\beta}\right), \quad \text{(A11)}$$

and $x = -e\Phi_f/(k_B T_e)$ is the reduced floating potential, while $\bar{\tau} = T_e/T_{i,\perp}$ is the ratio of electron temperature and ion temperature perpendicular to $\vec{E}$. The other parameters are the mass ratio $\mu = m_i/m_e = 7.28\times10^4$ (for argon), density ratio $\varepsilon = n_e/n_i$ and β, which relates the shape parameters of the IVDFs parallel and perpendicular to $\vec{E}$ to each other and has been defined below Eq. (A7). The values for β in the evaluated height interval lie between 0.031 and 0.04. The corresponding values for $J_1(\beta)$ and $J_2(\beta)$ vary slightly ($\pm12\%$ for J_1 and $\pm2.7\%$ for J_2) in the evaluated height interval, indicating that the determination of $\tilde{s}_{SiO_2}$ depends weakly on β. μ is only dependent on the species of ions regarded.

Appendix B: Comparison between constant-σ model and OML for the sticking evaluation

The classical *orbital motion limit* (OML) theory is one of the oldest and simplest charging models for electric probes and microparticles in a plasma[1]. It considers a situation in the plasma bulk, where no electric field is present and both electrons and ions have Maxwellian, isotropic velocity distributions with temperatures T_e and T_i, respectively. In the sheath, this premise is clearly violated. For the sake of completeness and as a comparison to another widely used charging model, the sticking calculations have also been done using the OML expressions for ion and electron current. Using those, Eq. (7) in the main publication becomes

$$\tilde{s}(x) = \frac{e^x}{\varepsilon\sqrt{\mu\tau}}(1+\tau x), \quad \text{(B1)}$$

which has a shape similar to Eq. (A10). $\tau = T_e/T_i$ is the ratio between the temperatures of the Maxwellian electrons and ions. The density ratio $\varepsilon \neq 1$ reflects the fact that there is no quasineutrality in this situation. For the evaluation, $\varepsilon(h)$ from the XPDP1 simulation was used,

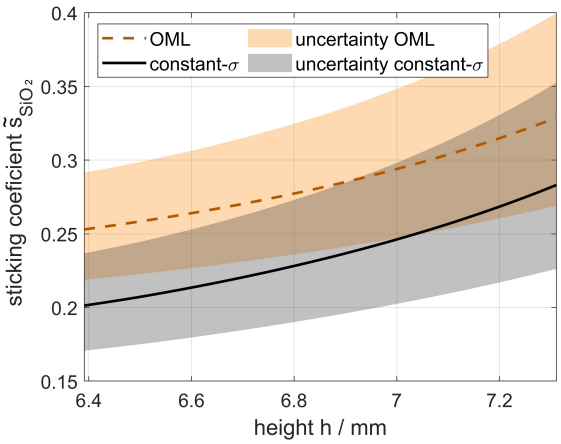

FIG. 1. Results for $\tilde{s}_{SiO_2}$ obtained from the interpolated $Y(h)$ curve using the OML model (orange, dashed line) and the constant-σ model (black, solid line). The corresponding uncertainties are visualized as shaded areas. The OML model yields values for $\tilde{s}_{SiO_2}$ that are on average 0.049 (21%) higher than that of the more refined constant-σ model.

like in the evaluation using the constant-σ model. Because the ions in the simulation could not be assigned a well-defined isotropic temperature considering all components of their velocity, an average value of $\tau = 50$ was used for this comparison. SiO_2 sticking coefficients have been calculated with both charging models using the interpolated $Y(h)$ curve in the evaluated interval (see Fig. 3 in the main publication). The result is shown in Fig. 1. The constant-σ result is visibly (0.049) smaller than that obtained using OML. However, the results using both models are below unity and below the theoretical prediction of ca. 0.66[7]. Using the more accurate constant-σ charging model certainly produces more reliable results for $\tilde{s}_{SiO2}$.

Appendix C: Details on the XPDP1 simulation

As mentioned in the main publication, a version of the particle-in-cell code XPDP1[8–10] was used that was modified for the Phelps argon collision cross sections[11], i.e. the Monte-Carlo collision model in the original version was extended by those cross sections. XPDP1 is a *1d3v* code, meaning that the spatial coordinates of the superparticles were only considered in one dimension (divided into 256 grid cells), while all three components of the velocity were considered. This reflects the symmetry of an infinitely expanded parallel plate reactor, which is a valid simplification for the real discharge. The simulation considers no dust particles, which is justified as the influence of a single microparticle on the plasma parameters as a whole should be negligible. The simulation was first run until equilibrating at ca. 3.5×10^5 superparticles,

which each consisted of 2×10^6 physical particles. Then, it was advanced 1000 timesteps of 0.1 ns each, covering a time of 100 ns, which covers slightly more than a rf period (which is ca. 73.7 ns at 13.56 MHz). The parameters of interest (electron and ion densities and velocity distributions, electric field) were averaged over the rf period. The resulting mean values were then used for the further analysis.

The accompanying input file for XPDP1 is for a version where the Phelps cross sections are implemented and enabled by setting the option `GAS` to 6. The standard cross sections can still be used by changing this option to 2, which also makes the input file compatible to the unmodified version of XPDP1 directly available for download.

[1] J. E. Allen, Probe theory - the orbital motion approach, Physica Scripta **45**, 497 (1992).

[2] A. Piel, *Plasma Physics - An Introduction to Laboratory, Space, and Fusion Plasmas*, 2nd ed. (Springer, 2017).

[3] A. Melzer, *Physics of Dusty Plasmas- An Introduction*, 1st ed. (Springer Nature Switzerland AG, 2019).

[4] A. Piel, H. Jung, and F. Greiner, Molecular dynamics simulations of wake structures behind a microparticle in a magnetized ion flow. II. Effects of velocity spread and ion collisions, Physics of Plasmas **25**, 10.1063/1.5039606 (2018).

[5] M. Lampe, T. B. Röcker, G. Joyce, S. K. Zhdanov, A. V. Ivlev, and G. E. Morfill, Ion distribution function in a plasma with uniform electric field, Physics of Plasmas **19**, 10.1063/1.4768456 (2012).

[6] F. W. Olver, *NIST handbook of mathematical functions* (Cambridge University Press, Cambridge and New York and Melbourne, 2010).

[7] F. X. Bronold and H. Fehske, Microscopic theory of electron absorption by plasma-facing surfaces, Plasma Physics and Controlled Fusion **59**, 014011 (2017).

[8] J. P. Verboncoeur, M. V. Alves, V. Vahedi, and C. K. Birdsall, Simultaneous potential and circuit solution for 1d bounded plasma particle simulation codes, Journal of Computational Physics **104**, 321 (1993).

[9] V. Vahedi, G. DiPeso, C. K. Birdsall, M. A. Lieberman, and T. D. Rognlien, Capacitive rf discharges modelled by particle-in-cell Monte Carlo simulation. I. Analysis of numerical techniques, Plasma Sources Science and Technology **2**, 261 (1993).

[10] V. Vahedi, C. K. Birdsall, M. A. Lieberman, G. DiPeso, and T. D. Ronhlien, Capacitive rf discharges modelled by particle-in-cell Monte Carlo simulation. II. Comparisons with laboratory measurements of electron energy distribution functions, Plasma Sources Science and Technology **2**, 273 (1993).

[11] A. V. Phelps, The application of scattering cross sections to ion flux models in discharge sheaths, Journal of Applied Physics **76**, 747 (1994).

Physics of Plasmas BRIEF COMMUNICATION pubs.aip.org/aip/pop

Electron sticking coefficients of dusty plasma relevant materials

Cite as: Phys. Plasmas **32**, 024501 (2025); doi: 10.1063/5.0251848
Submitted: 5 December 2024 · Accepted: 21 January 2025 ·
Published Online: 10 February 2025

Isabel König,[1,a)] Armin Mengel,[1,b)] and Franko Greiner[1,2,c)]

AFFILIATIONS

[1]Institute of Experimental and Applied Physics, Kiel University, 24118 Kiel, Germany
[2]Kiel Nano, Surface and Interface Science KiNSIS, Kiel University, 24118 Kiel, Germany

[a)]Electronic mail: koenig@physik.uni-kiel.de
[b)]Electronic mail: mengel@physik.uni-kiel.de
[c)]Author to whom correspondence should be addressed: greiner@physik.uni-kiel.de

ABSTRACT

Using a relative measurement approach, the sticking coefficients of dielectric materials commonly used in "dust in plasma" studies—specifically silica (SiO_2), melamine formaldehyde (MF, $[C_4H_8N_6O]_n$), and polymethyl methacrylate (PMMA, $[C_5O_2H_8]_n$)—were estimated. These results offer important insights for interpreting experiments involving various materials or their combinations, enabling more precise comparisons and experimental designs.

Since the mid-1990s, dusty plasma experiments involving micrometer-sized "artificial" dust particles have predominantly relied on dielectric (electrically insulating) polymer particles. Polymers are ideal materials for such studies because they can be produced as perfect spheres with a small standard deviation and they are commercially available.[1] In contrast, the production of monodisperse metallic spheres poses technical challenges and they are heavier, making it difficult to electrically confine them in the plasma sheath. For example, aluminum spheres are approximately twice as heavy as melamine formaldehyde (MF) spheres of the same size. The possibly differing charging behaviors of metallic and dielectric particles were identified and discussed early on. A key factor is the low mobility of charges on dielectric surfaces, which may approach zero for materials with zero electrical conductivity. This limited mobility can lead to asymmetric charging of a dielectric sphere in the directed ion flows of the plasma sheath. Such asymmetry may generate an electric dipole moment, causing the particle to spin. Over time, this spinning can average out the charge asymmetry, as discussed by Hutchinson.[2] Another critical aspect is the surface's electron-sticking efficiency. For low-pressure plasmas, where electron energies are typically below 10 eV, theoretical treatments of electron sticking become challenging. Using the "invariant embedding principle," Bronold and Fehske predicted electron sticking coefficients ($\bar{s}$) for several dielectric materials for 2 eV thermal plasma electrons. Their estimates suggest values of approximately 0.65 for silica (SiO_2), 0.42 for sapphire (Al_2O_3), and 0.30 for magnesia (MgO).[3] However, the electronic structures of polymers like melamine formaldehyde (MF) and polymethyl methacrylate (PMMA) remain insufficiently understood, preventing theoretical estimation of electron sticking coefficients for these materials.

Recently, we developed a dusty plasma-based method to measure the electron sticking coefficient of dielectric materials at low electron energies.[4] This method is currently being upgraded to accommodate nonspherical particles, such as sapphire and magnesia. The objective of this Brief Communication is to present results for melamine formaldehyde (MF), polymethyl methacrylate (PMMA), and silica. We believe that publishing the electron sticking coefficients of these highly relevant materials is essential for the dusty plasma community, as these values influence not only future experimental investigations but also the interpretation of previously published data involving different dust particle materials. As these materials are available as perfect spheres, the experimental setup described by Mengel *et al.*[4] was utilized for these measurements. For detailed information on the setup and methodology, we refer readers to the original publication.[4]

In short, the method for estimating $\bar{s}$ is based on the observation that different materials charge differently in the sheath of a low-pressure radio frequency plasma. Variations in charging currents result in differences in floating potentials, allowing precise measurements of the floating potential to be used to determine the electron sticking coefficient. To eliminate the dependence on charge density in the sheath, which varies with a particle's position, a relative measurement

Physics of Plasmas BRIEF COMMUNICATION pubs.aip.org/aip/pop

scheme was introduced in Ref. 4. Since gold (or gold-coated) particles exhibit a sticking coefficient of approximately one,[5] a calibration curve is established using gold-coated spheres of various radii. This enables the determination of the floating potential ratio Y between gold and the material of interest. The measured ratios are presented in Fig. 1(a), where each data point corresponds to the floating potential measurement of a single particle. The uncertainty bars reflect the average of approximately 100 excitation cycles using the PEOM method,[6] which provides the particle's charge-to-mass ratio (q/m) and the Epstein friction coefficient (γ). The propagation of uncertainty also accounts for pressure and particle radius. Figure 1(a) reveals clear differences in the floating potentials of melamine formaldehyde (MF), polymethyl methacrylate (PMMA), and silica. Figure 1(b) shows the electron sticking coefficient derived from the Y values shown in Fig. 1(a), Notably, the sticking coefficient of MF is found to be relatively close to that of a

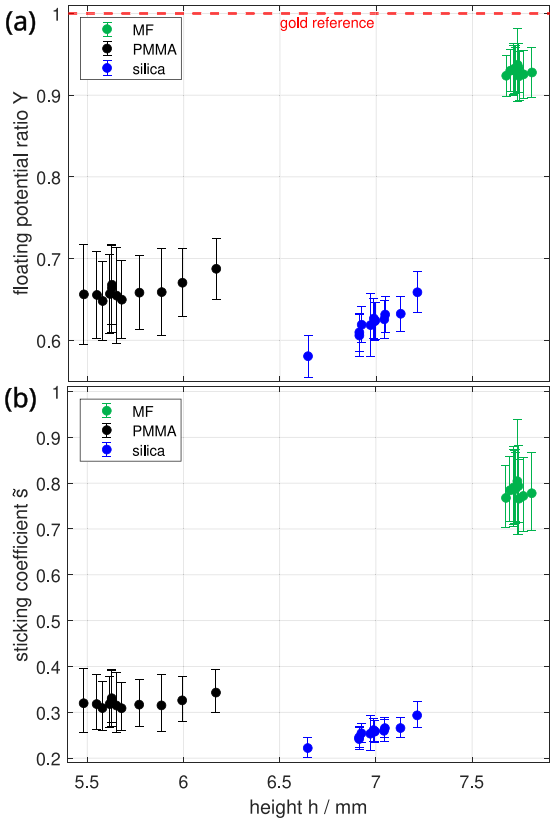

FIG. 1. (a) Floating potential ratio Y over the position in the sheath for MF, PMMA, and silica and gold-coated particles. The dashed red line is the gold reference. Each filled circle represents an individual dust particle. The floating potentials of PMMA and silica particles are significantly lower than that of a gold particle at the same height in the plasma sheath. The uncertainty bars are given by propagation of all measurement uncertainties.[4] (b) Sticking coefficient $\tilde{s}$ estimated from the floating potential ratio Y shown in (a). The increase in $\tilde{s}$ of silica shows a higher sensitivity of the coefficient to the electron energy compared to MF and PMMA, because the electron energy is different at different positions of the particles in the sheath.

TABLE I. Averaged electron sticking coefficient $\tilde{s}$ of silica, MF, and PMMA. For silica, a theoretical value of ($\tilde{s} = 0.65$) is available.[3] The deviation from the experimental value is probably due to the fact that the theory assumes crystalline silica, whereas the silica microspheres in the experiment are amorphous.

Material	MF, $[C_4H_8N_6O]_n$	PMMA, $[C_5O_2H_8]_n$	Silica, SiO_2
$\tilde{s}$	0.78 ± 0.08	0.32 ± 0.06	0.26 ± 0.03

metal, while silica exhibits the smallest value, with PMMA slightly exceeding silica in electron sticking efficiency.

For silica, a clear increase in the sticking coefficient with increasing height in the plasma sheath is observed. This trend is attributed to the sticking coefficient's energy dependence,[3] indicating a stronger relationship between the electron sticking coefficient and electron energy for silica compared to MF and PMMA.

In future work, our experimental setup will be upgraded to allow direct measurements of the energy dependence of the electron sticking coefficient. For now, the average values reported in Table I offer reasonable estimates of the sticking coefficient for electron energies in the single-digit electronvolt range.

We acknowledge the support from the Deutsche Forschungsgemeinschaft (DFG) in project GR1608/9-1 (Project Number 443791209).

AUTHOR DECLARATIONS

Conflict of Interest

The authors have no conflicts to disclose.

Author Contributions

Isabel König: Conceptualization (equal); Data curation (equal); Formal analysis (equal); Investigation (equal); Methodology (equal); Software (equal); Validation (equal); Visualization (equal); Writing – original draft (equal); Writing – review & editing (equal). **Armin Mengel:** Conceptualization (equal); Data curation (equal); Formal analysis (equal); Funding acquisition (equal); Investigation (equal); Methodology (equal); Software (equal); Supervision (equal); Validation (equal); Visualization (equal); Writing – original draft (equal); Writing – review & editing (equal). **Franko Greiner:** Conceptualization (equal); Data curation (equal); Formal analysis (equal); Funding acquisition (equal); Methodology (equal); Project administration (equal); Resources (equal); Supervision (equal); Validation (equal); Visualization (equal); Writing – original draft (equal); Writing – review & editing (equal).

DATA AVAILABILITY

The data that support the findings of this study are available from the corresponding author upon reasonable request.

REFERENCES

[1]microParticles GmbH, "microParticles Onlineshop" (2008). https://www.microparticles-shop.de.
[2]I. H. Hutchinson, "Spin stability of asymmetrically charged plasma dust," New J. Phys. **6**, 43 (2004).

[3]F. X. Bronold and H. Fehske, "Microscopic theory of electron absorption by plasma-facing surfaces," Plasma Phys. Controlled Fusion **59**, 014011 (2017).
[4]A. Mengel, F. X. Bronold, and F. Greiner, "Evidence of different charging behavior of conductive and dielectric materials in low-temperature plasmas and a new diagnostic for low-energy electron absorption," Phys. Rev. Lett. **133**, 185301 (2024).
[5]L. A. Gonzalez, M. Angelucci, R. Larciprete, and R. Cimino, "The secondary electron yield of noble metal surfaces," AIP Adv. **7**, 115203 (2017).
[6]A. Mengel, M. Artz, and F. Greiner, "Pulse excited oscillation: A new high-precision excitation method for the charge-to-mass ratio determination of microparticles in plasma and comparison to stepwise excitation and the phase-resolved resonance method," Phys. Plasmas **30**, 123704 (2023).

Physics of Plasmas ARTICLE pubs.aip.org/aip/pop

Equivalent spherical capacitor of non-spherical grains in a laboratory dusty plasma

Cite as: Phys. Plasmas **32**, 033703 (2025); doi: 10.1063/5.0249630
Submitted: 19 November 2024 · Accepted: 12 March 2025 ·
Published Online: 25 March 2025

Armin Mengel,[1,a] Isabel König,[1,b] Lorin S. Matthews,[2,c] and Franko Greiner[1,3,d]

AFFILIATIONS

[1]Institute of Experimental and Applied Physics, Kiel University, 24118 Kiel, Germany
[2]Center for Astrophysics, Space Physics, and Engineering Research, Baylor University, Waco, Texas 76798, USA
[3]Kiel Nano, Surface and Interface Science KiNSIS, Kiel University, Germany

[a]Author to whom correspondence should be addressed: mengel@physik.uni-kiel.de
[b]Electronic mail: koenig@physik.uni-kiel.de
[c]Electronic mail: lorin_matthews@baylor.edu
[d]Electronic mail: greiner@physik.uni-kiel.de

ABSTRACT

For spherical dust particles in dusty plasmas, the capacitor model is an easy and widely used model to link the charge of the particles to their floating potential. To extend dusty plasma studies to non-spherical particles, a similar relation for arbitrary particle shapes is needed. The non-spherical geometry can be reduced by relating the charge to that of an equivalent spherical particle. Such an equivalent radius is determined experimentally and by using simulations for microsphere aggregates under laboratory conditions. The results are compared to the electrostatic capacitance, as well as two approximative models, the orientation-averaged equivalent sphere model (OAES) and the smallest enclosing sphere model (SES). An excellent agreement with the electrostatic capacitance is found, validating the capacitor model for non-spherical particles. The OAES model can be used as a good approximation for compact particles or using a correction function, deviating $\leq 5\%$ from the capacitor model. The SES model is not an appropriate approximation under laboratory low-pressure plasma conditions.

I. INTRODUCTION

Up to the present time, the majority of nano- and microparticles considered in laboratory dusty plasma experiments and simulation are spherical or treated as such. The largest portion of related theory also focuses on spherical particles. However, many real world dusty plasma systems, like technological, ionospheric, and astrophysical plasmas, contain non-spherical particles and would benefit from a more detailed realistic description. For example, the alignment of interstellar dust to magnetic fields shows evidence that this dust has to be non-spherical,[1] and laboratory experiments have predicted ice dust grains in the interstellar medium to be elongated.[2] In the laboratory context, previous experimental and computational studies utilizing non-spherical particles were concerned with rodlike particles[3–9] or Janus particles. Janus particles have a coating on one of their hemispheres, which make their interactions with their environment non-symmetric.[10,11] The investigations looked at aspects like the particle orientation and motion in electrical fields, their interaction with each other, and the properties of the systems composed of them. Previous work on non-spherical particles was more focused on the growth of non-spherical particles in astrophysical dusty plasmas.[12–16] These investigations treated the charge on the aggregates in a heuristic way using fractal scaling laws. Other studies considered the formation of dipoles on non-spherical particles.[17] Perhaps the most central aspect, however, is the charge of a non-spherical particle. Simulations have successfully been used to examine the charge on more complicated non-spherical particles[18–20] and show a good agreement with experimental observations.[21] As the accurate description of the charging processes on a non-spherical grain is much more intricate than for a spherical grain, the theoretical models for spherical particles must be modified to take into account the complex surface geometry of a non-spherical grain.[15,16] One very crucial model is the capacitor model linking the charge q_s of a spherical particle to its floating potential Φ_f via the capacitance of a sphere.[22] In contrast to astrophysical dusty plasmas, quantities like the particle charge or its shape are directly

accessible in a laboratory situation. Therefore, the focus of this paper lies on the connection between charge and floating potential of a non-spherical particle in the laboratory dusty plasma context.

We will present results that allow one to describe this connection using an equivalent spherical capacitor model, where the equivalent spherical capacitor is characterized by its radius.

It has been postulated that the equivalent radius derived from the capacitance of non-spherical structures may be approximated by two different models: the orientation-averaged equivalent sphere, OAES, and the smallest enclosing sphere, SES, which will be presented in Sec. II. In Sec. III, the radius a_{eq} of an equivalent spherical particle carrying the same charge is experimentally determined for aggregates of 2–4 microspheres. Simulations yielding a_{eq} for aggregates of 13–27 spherical monomers are covered in Sec. IV. The results from Secs. III and IV are compared to the capacitance and the predictions made by the OAES and SES models. The capacitance and the equivalent radii of SES and OAES are also calculated for a set of simple geometries to allow further studies. The validity of the capacitor model and the applicability of OAES and SES as approximations thereof are finally discussed and compared to previous results in Sec. V, before a conclusion is drawn in Sec. VI.

II. THEORETICAL BACKGROUND

For dust particles in a plasma, generally, multiple charging mechanisms exist. In laboratory systems, charge collection is the dominant process and leads to negative charges in the order of magnitude of -10^3 to -10^5 e (where e is the elementary charge) for a typical dust particle with about 10 μm diameter. Charge collection is often described using the simple *orbital motion limited* (OML) model,[23–25] which describes an isotropic collisionless plasma. Anisotropy in the plasma, such as the ion flow in a plasma sheath, also affects the grain charge:[22] the charge on the grain can be enhanced or reduced depending on the flow speed and the grain material.[26] However, this presents only a minor influence on the particle charge.[27] A dipole moment is induced on dielectric grains, and the ion wake created downstream of charged grains results in a dipole potential field.[27–29] Improved models also exist for collisional plasmas,[30] but due to their complexity, those models are still not widely used in favor of the much simpler OML model. In astrophysical situations, photoemission and secondary electron emission from collisions with high-energy primaries are also relevant and even allow for the particle charge to become positive.[19,31] Particles in the plasma afterglow also usually attain positive charges[32–34] due to the much faster loss of electrons compared to ions, even though negative charges can still be achieved using charge control techniques.[33,35,36]

The surface potential of the particle reaches a stable steady state, the floating potential Φ_f, when all the charging currents cancel out to zero, bar minimal charge fluctuations.[37] These fluctuations happen on a much faster timescale ($< 1\mu s$) than the charging time, which is on the order of several $10\mu s$ for a typical microparticle under laboratory conditions.[24] In the time average over a few μs, these fluctuations therefore disappear.

A. Capacitor model

To calculate the charge q_s of a spherical particle from its floating potential, the capacitor model is used by default

$$q_s = C\Phi_f = 4\pi\varepsilon_0 a\Phi_f. \quad (1)$$

The capacitor model uses the capacitance $C = 4\pi\varepsilon_0 a$ of a single sphere with the radius a to create a relation between Φ_f and q_s. For situations where the particle radius a is comparable to the Debye length λ_D, the capacitance is enhanced by a factor $(1 + a/\lambda_D)$. In essence, the capacitor model simplifies the dust particle as a surface embedded in vacuum with a spatially constant surface potential equal to the floating potential Φ_f. This simplification describes the observed behavior of the charge of spherical microparticles very well. In principle, the capacitor model should be extensible to non-spherical particles.[22] The electrostatic potential and electric field around differently shaped particles with the same capacitance are identical at distances from the particle greater than roughly one ion Debye length.[38,39] In typical laboratory dusty plasmas, where the particle dimensions are much smaller than the Debye length, the electrostatic interaction of the particle with its surroundings is dominated by the total charge on the particle, as higher order terms of the multipole expansion decay faster with distance from the particle. The higher order terms come into play for the interaction between aggregates at grain separations below 10 times the particle dimensions.[20] Thus, every non-spherical particle is equivalent to a spherical particle with a radius R_C, which has the same capacitance,

$$R_C = \frac{C}{4\pi\varepsilon_0}. \quad (2)$$

R_C is used in place of the sphere radius a in Eq. (1) for non-spherical particles. Assuming the capacitor model to be true, one expects R_C to be equal to the radius a_{eq} of a spherical particle with equal charge, which is measured independently in Secs. III and IV. However, the application of the capacitor model generally requires accurate knowledge of the capacitance of the particle. For basic shapes like cylindrical disks and rods,[40,41] ellipsoids,[42] or touching doublespheres,[43] analytical expressions for the capacitance exist, while the capacitance of more complex geometries is generally not known or difficult to calculate or measure. This is especially true for experimental situations where the geometry of the particle cannot be exactly determined.

Two simpler models have been postulated to be approximating R_C, which shall be shortly introduced in the following.

B. Smallest enclosing sphere (SES) model

The *smallest enclosing sphere* (SES) model states that a non-spherical particle carries the same charge as a spherical particle with a radius R_e. The sphere with radius R_e is the smallest sphere completely enclosing the non-spherical particle in question. Observations supporting this model were made by comparing a ZnO tetrapod to a polymethyl methacrylate (PMMA) sphere in the sheath of an rf plasma[44] and by evaluating the trajectories of single microspheres and doublets (two touching microspheres) in the plasma afterglow.[45]

Finding the radius of the smallest enclosing sphere is equivalent to finding the radius a_{bs} of the *minimal bounding sphere* of all points on the particle surface. For a non-spherical particle consisting of spherical monomers with equal radii, the geometric problem of finding the minimal bounding sphere of the whole aggregate simplifies to finding the minimal bounding sphere of the monomer centers $a_{bs,c}$, and adding the monomer radius a_m,

Physics of Plasmas ARTICLE pubs.aip.org/aip/pop

$$R_e = a_{bs,c} + a_m. \quad (3)$$

As the minimal bounding sphere problem is a common problem in statistical analysis, operations research, and computer graphics, a plethora of algorithms has been developed over time, varying in accuracy and runtime. For all non-trivial non-spherical particles in this work, a_{bs} (or $a_{bs,c}$, respectively) was computed using a MATLAB implementation[46] of Welzl's algorithm.[47]

C. Orientation-averaged equivalent sphere (OAES) model

The *orientation-averaged equivalent sphere* (OAES) model, on the other hand, considers the reduced mean geometrical cross section of non-spherical structures compared to their enclosing spheres. In this model, R_C is approximated by the radius R_σ of a circle with an area equal to the orientation-averaged projected area (PA) of the particle,

$$R_\sigma = \sqrt{\frac{PA}{\pi}}. \quad (4)$$

The details on the numerical calculation of PA are given by Gopalakrishnan *et al.*[48] The MATLAB implementation written and used for this work is freely available to download.[49] With enough images of the particle from different angles, PA can in principle also be estimated as the mean projected area of the particle among these images. In this way, the OAES model is capable of yielding results when the capacitance cannot be calculated due to a lack of information on the three-dimensional structure of the particle. The application of this model to the charging of non-spherical particles was introduced by Matthews *et al.*[50] An important characterization of an aggregate's structure based on R_σ is the compactness factor Φ_σ, defined by Paszun and Dominik,[51]

$$\Phi_\sigma = \frac{V}{\frac{4\pi}{3}R_\sigma^3}, \quad (5)$$

where V is the volume of the particle. For a monodisperse particle (consisting of monomers with the same radius a_m), this simplifies to

$$\Phi_\sigma = \frac{N a_m^3}{R_\sigma^3}. \quad (6)$$

D. Calculations for simple geometries

To assess how well R_σ and R_e coincide with R_C, these three radii are computed for a range of simple particle geometries assembled from a number N of spherical monomers (*sphere aggregates*). The monomers had a constant radius a_m of 1 for simplicity, so that the resulting R_e, R_σ, and R_C were already given in units of the monomer radius a_m. R_e and R_σ were calculated as described in Secs. II B and II C, respectively.

The capacitance of each geometry was computed using the MATLAB implementation of the finite elements method. As a Dirichlet boundary condition, the potential $\Phi_{sim,S}$ on the particle surface was set to 1 V with respect to the potential $\Phi_\infty = 0$ at infinity. In the numerical calculation, $\Phi_\infty = 0$ was approximated by the potential on a distant bounding sphere with a radius $R \gg R_e$. Numerically solving this system yielded the electrostatic potential and electric field in the space between the particle surface and distant spherical hull. Using Gauss's law, the particle charge q_{sim} was then obtained by numerically integrating the electric field on a spherical surface enclosing the particle. For a better grasp on the variance of the obtained charge, the charge was calculated for integration surfaces with different radii. The average of this set of values was used for further calculations. Finally, the capacitance of the structure was obtained from its charge and the potential difference with respect to infinity,

$$C_{sim} = \frac{q_{sim}}{\Phi_{sim,S} - \Phi_\infty} = \frac{q_{sim}}{1\text{V}}. \quad (7)$$

R_C is then calculated as

$$R_C = \frac{C_{sim}}{4\pi\varepsilon_0}. \quad (8)$$

These calculations were carried out for the following groups of plausible aggregate structures (see also Fig. 1):

- straight linear chains of 2-25 monomers,
- triplets with varying central angle $\theta = 60$ to $180°$,
- tetrapods approximated by four linear chains of spheres joined at a central monomer,
- structures with monomers at the vertices of platonic bodies,
- planar structures with sphere centers arranged in $n \times n$ squares with $n \in [2; 5]$,
- 320 randomly generated structures of 6, 8, 9, 16, and 25 touching spheres.

The same calculations were also done for the experimentally observed particle structures (see Sec. III), if not already included in the list above, as well as the structures considered in the OML_LOS simulation later on (Sec. IV).

III. EXPERIMENT

The experiment uses aggregates of a few (2–4) microspheres as non-spherical particles. Observing single microspheres under the same

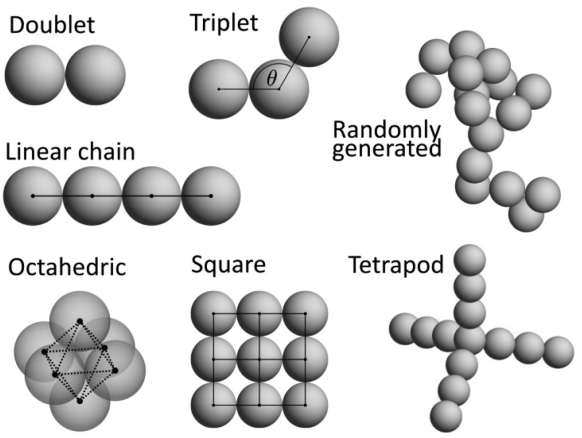

FIG. 1. Visualization of simple example structures for which R_e, R_σ, and R_C were calculated. The overlaid black lines and dots are meant to emphasize the three-dimensional structure of the respective aggregates. Each shown structure represents one group of structures, as described in Sec. II D.

conditions allows for comparison between the charges of the single and agglomerated microspheres. The particle size and geometry were measured using long-distance microscopy (LDM), while the *pulse-excited oscillation method* (PEOM)[52] yielded information about the charge and mass of the particles. The latter was checked against the *phase-resolved resonance method* (PRRM)[53] on a random test basis, which produced the same results, but is much more time-consuming. The details of the charging process of dust particles in the plasma sheath are potentially very intricate. However, this investigation focuses on the relation between the charge and floating potential of the particles, which can both be accessed with the used experimental approach. Therefore, the specifics of the charging process itself are not discussed here, as they can be found in the literature.[26,29,54–57]

A. Setup

The experiments in this work have been carried out in the *Sticking Cube II* reactor, a capacitively coupled argon RF discharge. The lower electrode was driven with a nominal power of $P_{\mathrm{RF}} = 1\,\mathrm{W}$ and a corresponding RF voltage amplitude of $\hat{U}_{\mathrm{RF,pp}} = 110\,\mathrm{V}$, while the upper electrode was grounded. A low-frequency excitation signal for use with the PEOM and PRRM was coupled onto the RF signal using a filter network. The electrode separation was 34 mm. Both electrodes had a diameter of 30 mm. The lower electrode had a cylindrical cavity (diameter 6 mm, 2 mm deep), and a metal ring (outer/inner diameter 21 mm/16 mm, 2 mm thick) was added on top of it for even stronger horizontal confinement. To accommodate the dust dropper, the upper electrode had a central 10.5 mm diameter hole. The argon pressure during all measurements was held at $p = 7.55 \pm 0.02\,\mathrm{Pa}$. Pressure and RF voltage and power were kept constant over all measurements, ensuring reproducibility. For each run of the measurement, the dust dropper was filled with commercially available[58] spherical gold-coated melamine formaldehyde (MF) particles with a different nominal size. In preliminary tests, the probability to observe aggregates of microparticles was decidedly higher using gold-coated particles than with silica or polymer spheres. The nominal diameters used were 4.13, 5.95, 7.89, 9.49, 9.94, and11.87 μm. Aggregates of 2–4 microspheres sometimes formed at random and could be trapped in the plasma sheath. The formation of the aggregates most likely happened in the dust dropper before being introduced into the plasma, as each aggregate was visible as a single coherent body in the laser illumination immediately after exiting the dust dropper. From the numbers of the trapped particles, empirical probabilities to trap an aggregate of 2 or more monomers were obtained. Doublets occurred with a chance of $\approx 16\%$, triplets with $\approx 7.6\%$, and quadruplets with $\approx 5.7\%$. The remaining particles were single spheres. A green laser ($\lambda = 532\mathrm{nm}$) beam was expanded to about 10 mm diameter and aimed at the particle using a pair of galvanometer mirrors. The laser beam was terminated in a beam dump outside the vacuum vessel. The galvanometer mirrors were each controlled by an external voltage, which allowed for particle illumination at every position in the plasma volume. A high-speed camera (max. 200 fps) was used to track the position of the illuminated particle during the PEOM and PRRM measurements. A white LED flash (flash duration 200 μs) and a high-resolution camera (4000 × 3000 pixel) with a LDM lens (magnification $M \approx 30$) were used to take 40–100 images of each particle. A typical LDM image of a doublet is shown in Fig. 4. Both cameras were calibrated with scales positioned in the empty chamber. The calibration of the PEOM

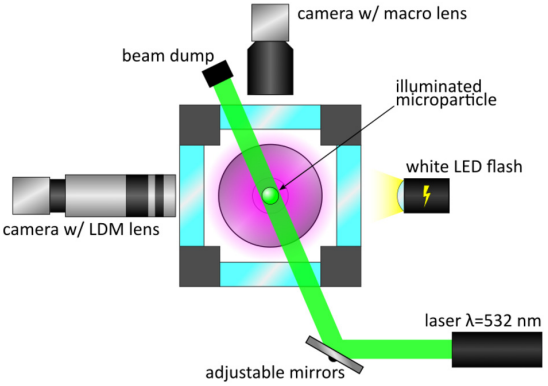

FIG. 2. Schematic top view of the experimental setup, emphasizing the optical setup. The mirror system allows the laser to be adjusted horizontally and vertically. The electrical setup for the PEOM and PRRM is shown in Fig. 3 separately.

camera allows for a determination of the absolute equilibrium height h of each particle above the electrode (1 px equates to 5.5 μm), while the calibration of the LDM camera allows for a conversion between pixels on the LDM images and absolute distance in the focal plane (1 px equates to 0.06 μm). The laser was switched off during the LDM measurements to avoid interfering with the lighting by the LED flash. A schematic view of the most important parts of the setup is shown in Figs. 2 and 3.

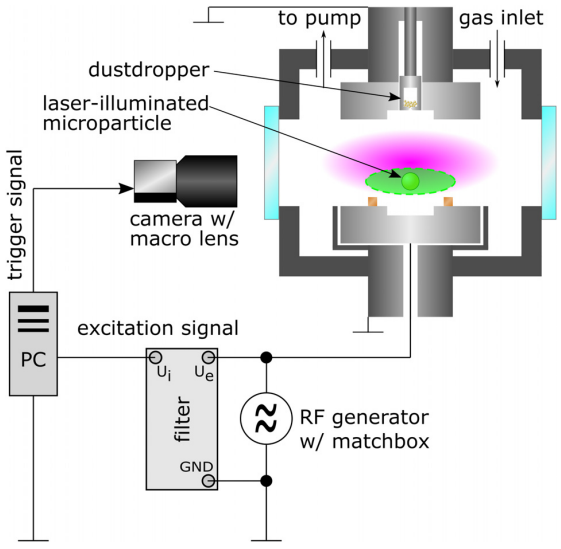

FIG. 3. Schematic side view of the setup, focusing on the electrical setup and the electrode geometry. The dust dropper is embedded in the upper electrode. A metal ring on the lower electrode enhances the horizontal confinement of the particles. All excitation and trigger signals needed for PEOM and PRRM are generated by a computer. The excitation signal is coupled into the driving voltage of the plasma via a filter network to avoid damage to the hardware.

Physics of Plasmas ARTICLE pubs.aip.org/aip/pop

B. Measurement and analysis scheme

The PEOM (and PRRM) measurements yield the eigenfrequency ω_0 and damping rate γ of each particle's oscillation in external excitation. ω_0 is defined as,

$$\omega_0 = \sqrt{\frac{q\rho_q}{m_d\varepsilon_0}}, \tag{9}$$

where ρ_q is the absolute space charge density at the particle position and m_d is the mass of the dust particle. For spherical particles, the Epstein model[59] for the damping rate γ is valid,

$$\gamma = \delta\frac{4}{\pi}\frac{p}{a\rho_m\hat{v}_{th,n}}, \tag{10}$$

where p is the gas pressure, ρ_m is the mean mass density of the particle, and $\hat{v}_{th,n}$ is the thermal velocity of the neutral gas. δ is a dimensionless coefficient determining whether the reflection of the neutral gas atoms at the particle surface is diffuse or specular, and if the particle is sufficiently thermally conductive. For dusty plasma situations with spherical particles, $\delta = 1.44 \pm 0.05$ has been found in experiments with MF particles in different noble gases.[53] The radius a of the spherical particles is obtained from the LDM images (Fig. 4). Using these radii and Eq. (10), the mass m_s of the spherical particles is calculated. To account for the height-dependency of both the charge density ρ_q and the charging currents determining the particle floating potential, an auxiliary quantity η_s is defined using the capacitor model for spherical particles [Eq. (1)] and the definition of the eigenfrequency ω_0 [Eq. (9)]. A closely related approach was used in previous work to compare the floating potential of different particles,[60]

$$\eta_s := \Phi_f(h)\rho_q(h) = \frac{m_s\omega_{0,s}^2}{4\pi a}, \tag{11}$$

where η_s is calculated for each spherical particle at its equilibrium levitation height h using the results for $\omega_{0,s}$, a, and the mass m_s obtained from the result for γ. Based on these points $\eta_s(h)$, η_s is interpolated in the whole range of spherical particle levitation heights (about 4.9–9.1 mm above the electrode) using a fifth-order polynomial fit. The data and interpolation for $\eta_s(h)$ based on the measurements for 74 single spheres are shown in Fig. 5. It is assumed that the floating potential is the same for all particles with the same surface material at the same height.[60] For non-spherical particles, the relation between the charge q_{ns} and Φ_f is not used in order to provide an independent measurement. Instead, the quantity $\kappa \propto q_s\rho_q(h)$ is calculated from the mass m_{ns} and eigenfrequency $\omega_{0,ns}$ of the non-spherical particles,

$$\kappa := \frac{1}{\varepsilon_0}q_{ns}\rho_q(h) = m_{ns}\omega_{0,ns}^2, \tag{12}$$

where m_{ns} is obtained using the mass density ρ_m of spherical particles of the same nominal diameter as the spherical constituents of the aggregate using Eq. (10). The equivalent radius a_{eq} of a spherical particle is defined as the radius of a (hypothetical) spherical particle with the same charge $q_s = q_{ns}$. The charge of a spherical particle at the same height h can be calculated using the spherical capacitor model [see Eq. (1)]. This yields the following formula for the determination of a_{eq}:

$$a_{eq} = \frac{q_{ns}}{4\pi\varepsilon_0\Phi_f(h)} = \frac{\kappa}{4\pi\eta_s(h)}. \tag{13}$$

Using this, the equivalent radius a_{eq} is calculated for each of the observed aggregates, without making assumptions about the capacitor model and thus independently measuring the equivalent radius.

C. Experimental results

A total of 17 doublets, 8 triplets, and 6 quadruplets have been recorded and evaluated. The calculation of a_{eq} for the observed aggregates yielded the results presented in Figs. 6, 7, and 8 and Table I. To make the comparison between different monomer sizes easier, a_{eq}, R_e,

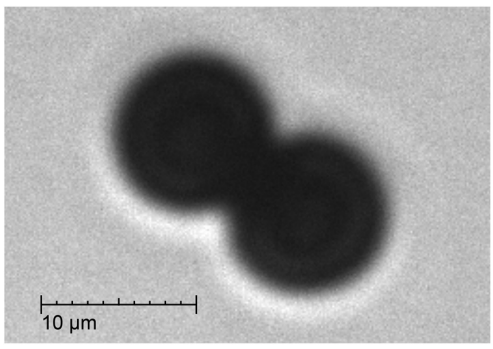

FIG. 4. Typical raw LDM image of a doublet consisting of two gold-coated MF spheres with a nominal diameter of 9.49 μm. For the analysis, the inhomogeneous lighting was corrected using a background image taken without a particle. The actual diameter of each sphere was determined from the average FWHM of multiple intensity profiles along straight lines crossing the respective circle center. One pixel of the image translates to 60.1 nm distance in the focal plane.

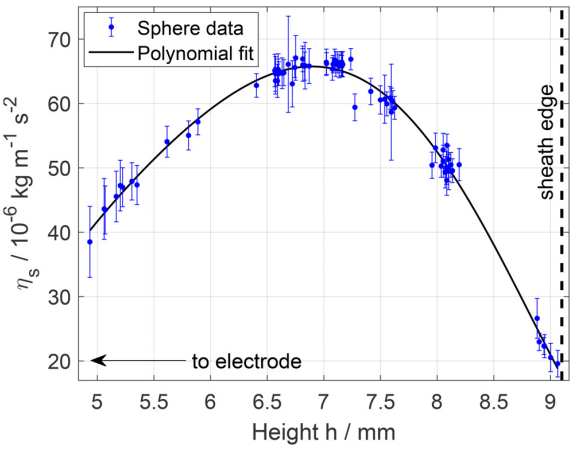

FIG. 5. Results for $\eta_s(h)$. Each individual data point represents one spherical particle for which η_s has been calculated from PEOM and LDM data. The solid line is a fifth-order polynomial fit used to interpolate η_s for any position h in the range of spherical particle levitation heights (about 4.9–9.1 mm above the lower electrode). The black dashed line indicates the lower sheath edge of the plasma, as determined by the plasma glow intensity.

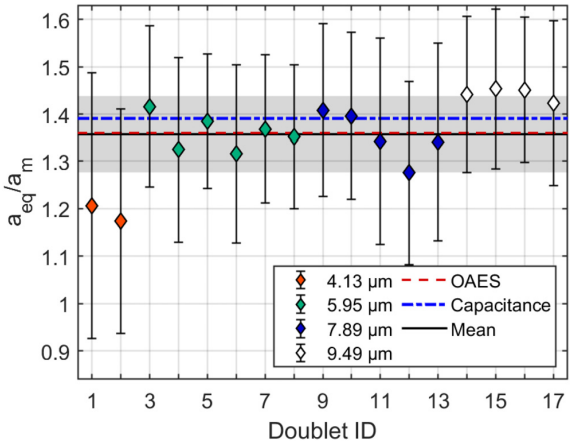

FIG. 6. Equivalent radius a_{eq} of the 17 observed doublets in units of the respective monomer radius a_m. The different fill colors of the markers represent the nominal monomer diameter. The prediction made using the OAES model, and the electrostatic capacitance are shown as red, dashed blue, and dashed-dotted lines, respectively. The SES prediction lies at 2, significantly above the data points and is therefore not displayed. The solid black line marks the mean of a_{eq}/a_m of all observed doublets, and the shaded area indicates the respective uncertainty.

R_σ, and R_C are given in units of the (mean) monomer radius a_m of the respective particle. The doublets, triplets, and one of the quadruplets had structures already considered in the calculations of R_σ and R_C (see Sec. II D). For the remaining quadruplets, the respective calculations were done after analyzing their structure using the LDM images.

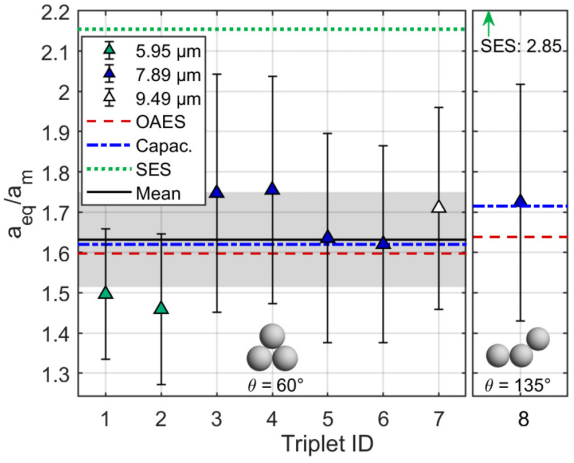

FIG. 7. Equivalent radius a_{eq} of the observed triplets in units of the respective monomer radius a_m. The color coding is the same as in Fig. 6 for the doublets. The left panel contains the data for the seven equilateral triplets ($\theta = 60°$), where a mean value for a_{eq}/a_m could be calculated. The right panel shows the data for the single non-equilateral triplet. The SES predictions are significantly above the measured data (2.15 and 2.85, respectively).

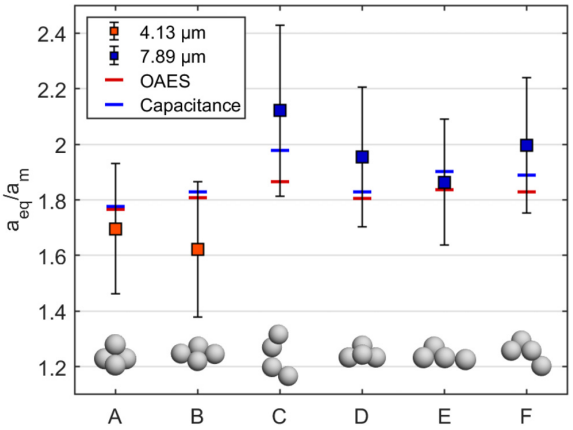

FIG. 8. Equivalent radius a_{eq} of the observed quadruplets in units of the respective monomer radius a_m. The color coding is similar to Figs. 6 and 7, but the predictions are individually plotted for each quadruplet. The quadruplets are labeled A-F in accordance with their nomenclature throughout this section. The structures of the quadruplets are sketched above the x-axis. The SES predictions are significantly above the measured data (see also Table I) and therefore not shown in this figure.

All doublets (Fig. 6) have an equivalent radius that is clearly incompatible with the SES model and very close to the OAES model and the electrostatic capacitance. The mean of a_{eq}/a_m over all doublets is almost identical to the OAES prediction, slightly below the capacitance value. Because the difference between the OAES prediction and the capacitance value ($1.39–1.36 = 0.03$) is very small in respect to the uncertainty of the measurement ($\Delta(a_{eq}/a_m) \geq 0.14$), no distinction can be made between capacitance and OAES based on the doublet results. The results from the doublets alone therefore allow no decision whether the OAES model or the capacitance agrees better with the experimental results.

TABLE I. Results for the equivalent radius a_{eq} in units of the mean monomer radius a_m, in comparison with the predictions by the SES and OAES model and the numerically calculated electrostatic capacitance.

	Experiment	Predictions		
	a_{eq}/a_m	SES R_e/a_m	OAES R_σ/a_m	Capacitance R_C/a_m
Doublets (mean)	1.36 ± 0.08	2.00	1.36	1.39[a]
Triplets $\theta = 60°$ (mean)	1.63 ± 0.12	2.15	1.60	1.62
Triplet $\theta = 135°$	1.7 ± 0.3	2.85	1.64	1.71
Quadruplet A	1.70 ± 0.24	2.22	1.77	1.78
Quadruplet B	1.62 ± 0.25	2.69	1.81	1.83
Quadruplet C	2.1 ± 0.3	3.17	1.87	1.98
Quadruplet D	1.95 ± 0.26	2.36	1.81	1.83
Quadruplet E	1.86 ± 0.23	2.99	1.84	1.90
Quadruplet F	2.00 ± 0.25	2.76	1.83	1.89

[a]The exact value for the doublet using the analytical capacitance provided by Lekner[43] is $R_C/a_m = 2\ln 2 \approx 1.386$.

Physics of Plasmas ARTICLE pubs.aip.org/aip/pop

Seven of the eight triplets (Fig. 7) had an equilateral structure ($\theta = 60°$). Their average a_{eq}/a_m is marginally above the capacitance value and the OAES prediction, but closer to R_C. a_{eq} of the last, more obtuse triplet ($\theta = 135°$) is almost identical to the predicted R_C, but both R_C and R_σ are easily within the uncertainty. For all triplets, the results were incompatible with the SES predictions.

Because the quadruplets (Fig. 8) all had different structures, no averaging is justified. There is no systematic tendency toward either the OAES prediction or capacitance value, but the experimental results always agree with both of these values while clearly contradicting the SES predictions.

IV. OML_LOS SIMULATION

A. Simulation procedure

To study the charge of aggregates with a higher number of monomers than could be achieved experimentally, the OML_LOS (*orbital motion limited—line-of-sight approximation*) simulation technique developed by Matthews *et al.*[18] is employed. The considered non-spherical structures were 108 aggregates of 13–27 spherical monomers generated to mimic experimentally observed aggregates of gold-coated melamine formaldehyde particles. The charging conditions in the simulation corresponded to those in a typical laboratory dusty plasma such as the one used in the experimental section of this work. A comparison between the conditions in laboratory dusty plasmas and protoplanetary disks as an astrophysical dusty plasma can be found in previous work.[50]

The surface of each particle is divided into surface elements, each of which receives the OML charging currents according to its surface potential during each time step. The line-of-sight approximation consists in attenuating the currents onto each surface element according to its LOS factor. The trajectories of incoming electrons and ions are assumed to follow straight line paths near the surface. The incoming particles are assumed only to contribute to the charging currents if they approach along open lines-of-sight, found by checking a number of test directions originating from the surface element to see if they intersect the rest of the particle surface. The LOS factor is the ratio of open lines-of-sight to the total number of test directions, which are distributed evenly over the solid angle. Thus, the charging current onto each surface element only accounts for electrons and ions not already blocked by other monomers of the same aggregate. The charge of each surface element is tracked separately, and its potential is updated according to the charge of all surface elements including itself after each time step. The OML currents were calculated assuming a isotropic plasma (as in the plasma bulk) consisting of electrons and argon ions, with temperatures $T_e = 46400\text{K} \approx 4\text{eV}$, $T_i = 298\text{K} \approx 0.026\text{eV}$, masses $m_e = 9.11 \times 10^{-31}\text{kg}$, $m_i = 40\text{u}$, and densities $n_e = n_i = 1.6 \times 10^{15}\text{m}^{-3}$. Using this technique, the steady-state charges of each structure were obtained as the sum over the charges of each surface element after equilibrating the system.

B. Simulation analysis and results

For the 108 artificially created aggregates (see Sec. IV A), the charge q was calculated using OML_LOS. Using the electron and ion masses and temperatures in the simulation, the floating potential of a sphere is calculated using the OML model.[23–25] The application of OML is justified here because the simulated aggregates are in a situation similar to the plasma bulk, where electrons and ions have isotropic, Maxwellian velocity distributions. The resulting floating potential $\Phi_f = -2.25 k_B T_e = -9.00\text{V}$ is used to calculate the equivalent capacitor radius as,

$$a_{eq} = \frac{q}{4\pi\varepsilon_0 \Phi_f}, \tag{14}$$

which is similar to Eq. (13), but with q/ε_0 and Φ_f replacing κ and η_s, respectively. For each of the particle geometries simulated with OML_LOS, R_e, R_σ, and R_C have also been calculated using the methods presented in Secs. II and II D. The results are displayed in Fig. 9. It is clearly visible that, aside from five single outliers, the capacitance radius R_C matches the equivalent charge radius a_{eq} extremely well, supporting the expectation that the capacitor model is valid for non-spherical particles. The remaining difference is attributed to errors arising from the discretization in the capacitance calculations. In contrast, the OAES prediction R_σ lies between 7% and 14% below a_{eq} for the largest portion of the simulated structures. The SES prediction R_e is significantly higher than a_{eq}. It overestimates a_{eq} by 21%–75%.

V. RESULTS AND DISCUSSION

A. Comparison of SES, OAES, and capacitor model

For all non-spherical geometries examined in this study, be it experimentally or via OML_LOS simulation, an excellent agreement of a_{eq} with the capacitor model is found. The OAES model performs almost as well for the experimentally observed particles with $N \leq 4$, but deviates by approximately 10% from the capacitance value and a_{eq} for the simulated particles, which have a lower compactness and $N \geq 13$. Both experiment and simulation contradict the SES model, which significantly overestimates a_{eq} in both those cases. The capacitor model is found to accurately describe the relation between particle charge and floating potential in a

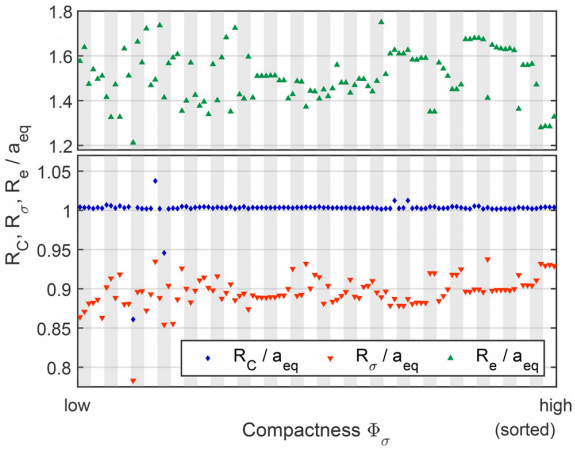

FIG. 9. Predicted radii R_C (capacitance), R_σ (OAES), and R_e (SES) compared to a_{eq}, computed for 108 particles simulated with OML_LOS. The predictions are given in units of a_{eq}, so that the horizontal line at 1 marks a perfect match between prediction (R_C, R_σ, R_e) and simulation results (a_{eq}). The values for R_e/a_{eq} are shown in a separate plot above, as they lie much farther away from 1 than the other predictions. Note the gap between the y-axes as well as their different scaling. All values are sorted along the x-axis according to the compactness Φ_σ of the respective structure, which increases from 0.32 to 0.44 along the x-axis.

plasma environment, justifying its use for non-spherical particles. The OAES model without further modifications can still approximate a_{eq} for aggregates with a high compactness ($\Phi_\sigma \gtrsim 0.6$) within 5%, which includes all geometries with $N \leq 3$. The latter is also true for some, but not all quadruplets. In contrast, the SES model does not predict a_{eq} for any simulated or experimentally observed particle, which is why we deem it not valid for the description of the charge of microsphere aggregates in typical laboratory (low-pressure) dusty plasmas.

B. Approximation of R_C by R_σ

As argued above, the electrostatic capacitance is a very accurate description of the equivalent radius a_{eq}. The OAES model is still a good approximation for low N (as seen with the experimentally observed particles in Sec. III C), but becomes less accurate with higher values of N, as can be seen with the simulated particles ($N \geq 13$, see Sec. IV B). For the simulated particles, the prediction R_σ of the OAES model was approximately 10% below the actual equivalent radius a_{eq} and the capacitance radius R_C. However, the purely geometrical calculation of R_σ is easier than solving the full electrostatic problem. Also, there may be situations when the capacitance is not easily calculated. Based on the data for R_C and R_σ of all geometries considered in this work, an empirical correction formula $F(\Phi_\sigma, N)$ is formulated. Using $F(\Phi_\sigma, N)$, R_C can be approximated as,

$$R_C \approx R_\sigma^{corr} = R_\sigma \times F(\Phi_\sigma, N), \tag{15}$$

where

$$F(\Phi_\sigma, N) = \Big[1.046 - (1.025 W_{lin}(N) + 0.0207) \times \exp\big(-11.28\big[\Phi_\sigma - \Phi_\sigma^{lin}(N)\big]\big)\Big]^{-1}, \tag{16}$$

$$W_{lin}(N) = 0.761 - 2.289\ \Phi_\sigma^{lin}(N) + 2.435\Big[\Phi_\sigma^{lin}(N)\Big]^2 - 0.904\Big[\Phi_\sigma^{lin}(N)\Big]^3, \tag{17}$$

and

$$\Phi_\sigma^{lin}(N) = N \times \left[1 + \frac{8}{3\pi}(N-1)\right]^{-3/2}. \tag{18}$$

This approximation formula is intended for aggregates of monodisperse spheres. For almost all ($\approx 98.3\%$) of the geometries in this work, R_σ^{corr} deviates less than 5% from R_C. The compactness factor Φ_σ of the aggregates was as low as 0.19. Using this formula, R_C of non-spherical particles approximated as aggregates of spheres[61] can be estimated based on R_σ, which is potentially easier to calculate for more complex geometries. Simplification of the charge estimation of non-spherical dust particles is important, since the study of the charge physics of non-spherical particles must rely on averages over a large number of particles. Simple experimental shape estimation (several 2D projections instead of a full 3D reconstruction) and capacity estimation (substitute capacity and approximation formula, instead of full numerical integration of the electric potential) will likely help laboratory dust plasma physics.

C. Previous SES observations

For the tetrapod-like aggregates investigated in Sec. II D, R_C and R_e differ significantly, indicating that the SES model is not specifically valid for tetrapodal particles. To explain the observations made by Asnaz *et al.*,[44] which gave rise to the SES model, other factors need to be taken into account. Previous work shows that dielectric and metallic surfaces charge to a different extent in the plasma due to their different electron sticking coefficient.[60] Asnaz *et al.* obtained a value for the equivalent radius of a ZnO tetrapod by comparison to a PMMA sphere. However, recent measurements revealed that the electron sticking coefficient of PMMA for low-energy electrons is significantly below 1.[62] The electron sticking coefficient of ZnO is not yet known for low energies. This could have significantly distorted the comparison. Repeating this measurement with the knowledge of the correct electron sticking coefficients would shed light on this seemingly contradictory observation. The results by van Minderhout *et al.*,[45] on the other hand, were measured in the spatial plasma afterglow at a much higher pressure (90Pa instead of 7.5Pa). Because the particles examined there carried positive charges, it is questionable whether the charging processes are comparable.

VI. CONCLUSION

The equivalent capacitor radius a_{eq} was experimentally determined for small ($N \leq 4$) sphere aggregates in the plasma sheath. Larger aggregates ($13 \leq N \leq 27$) in the plasma bulk were simulated using OML_LOS, from which the equivalent radius a_{eq} was determined as well. For the particles from both studies, as well as a set of simple geometries, the electrostatic capacitance, the smallest enclosing sphere, and the orientation-averaged projected area have been calculated for comparison. From these data sets, the radii R_C, R_e, and R_σ were obtained.

Both studies (experiment and OML_LOS simulation) show an excellent agreement with the capacitor model. This validates the capacitor model for the determination of the particle charge in dusty plasmas, as its simplifications seem to have negligible effect on the result in the dusty plasma context. The theoretical expectation that it is the correct description is therefore fulfilled. The OAES model is almost equally accurate for compact structures ($\Phi_\sigma \geq 0.6$), but its accuracy can be vastly improved using a correction function F for monodisperse aggregates with compactness parameters down to approximately 0.19, so that it approximates R_C and therefore a_{eq} with $\leq 5\%$ uncertainty. In principle, one could possibly also formulate a correction factor for polydisperse aggregates (such as those found in previous computational studies[18]) given enough data for the charge of such aggregates and a suitable parameter to use in place of the monomer count N. Finally, the SES model fails to accurately predict the equivalent radius in the laboratory plasma bulk and plasma sheath. Using these results, charge and floating potential of arbitrary non-spherical particles can be calculated from each other, because any arbitrary particle structure can be approximated as a monodisperse aggregate of a possibly high number of monomers. This connection, for example, allows the determination of the low-energy electron sticking coefficients of materials only available as non-spherical particles, using the relative measurement scheme initially developed for spherical particles.[60] Notably, dielectric materials, such as MgO or Al_2O_3, only occur as non-spherical grains. Dielectric materials are of high technological interest due to their central role in dielectric barrier discharges (DBDs) and their various applications,[63–66] which makes the knowledge of their surface properties highly desirable.

Physics of Plasmas ARTICLE pubs.aip.org/aip/pop

ACKNOWLEDGMENTS

A. M., I. K., and F. G. acknowledge the support from the Deutsche Forschungsgemeinschaft (DFG) in project GR 1608/9-1 (Project No. 443791209).

AUTHOR DECLARATIONS

Conflict of Interest

The authors have no conflicts to disclose.

Author Contributions

Armin Mengel: Conceptualization (lead); Data curation (equal); Formal analysis (lead); Investigation (supporting); Methodology (equal); Software (lead); Validation (equal); Visualization (lead); Writing – original draft (lead). **Isabel König:** Data curation (equal); Investigation (lead); Software (supporting); Validation (supporting); Visualization (supporting); Writing – review & editing (supporting). **Lorin Swint Matthews:** Conceptualization (supporting); Data curation (equal); Formal analysis (equal); Investigation (supporting); Methodology (equal); Validation (supporting); Writing – review & editing (equal). **Franko Greiner:** Conceptualization (equal); Funding acquisition (lead); Project administration (lead); Resources (lead); Software (supporting); Supervision (lead); Validation (equal); Writing – review & editing (lead).

DATA AVAILABILITY

The data that support the findings of this study are available from the corresponding author upon reasonable request. The MATLAB source code for the calculation of the orientation-averaged projected area is publicly available on the research data repository of Kiel University.[49]

REFERENCES

[1]A. Lazarian, "Tracing magnetic fields with aligned grains," J. Quant. Spectrosc. Radiat. Transfer **106**, 225–256 (2007).
[2]P. M. Bellan, "Why interstellar ice dust grains should be elongated," Astrophys. J. **905**, 96 (2020).
[3]V. I. Molotkov, A. P. Nefedov, M. Y. Pustyl'nik, V. M. Torchinsky, V. E. Fortov, A. G. Khrapak, and K. Yoshino, "Liquid plasma crystal: Coulomb crystallization of cylindrical macroscopic grains in a gas-discharge plasma," JETP Lett. **71**, 102–105 (2000).
[4]B. M. Annaratone, A. G. Khrapak, A. V. Ivlev, G. Söllner, P. Bryant, R. Sütterlin, U. Konopka, K. Yoshino, M. Zuzic, H. M. Thomas, and G. E. Morfill, "Levitation of cylindrical particles in the sheath of an rf plasma," Phys. Rev. E: Stat. Nonlinear Soft Matter Phys. **63**, 036406 (2001).
[5]B. M. Annaratone, A. G. Khrapak, and G. E. Morfill, "Peculiar properties of rodlike particles levitating in the sheath of an rf plasma," IEEE Trans. Plasma Sci. **37**, 1110–1115 (2009).
[6]B. M. Annaratone, A. V. Ivlev, V. E. Fortov, A. G. Khrapak, S. A. Khrapak, V. I. Molotkov, and G. E. Morfill, "Complex plasmas with rodlike particles," IEEE Trans. Plasma Sci. **39**, 2732–2733 (2011).
[7]N. Banu and C. M. Ticoş, "Precession of cylindrical dust particles in the plasma sheath," Phys. Plasmas **22**, 103704 (2015).
[8]W. J. Miloch, S. V. Vladimirov, H. L. Pécseli, and J. Trulsen, "Interaction of two elongated dust grains in flowing plasmas studied by numerical simulations," Phys. Plasmas **16**, 023703 (2009).
[9]N. Udrea, M.-L. Mitu, A. Scurtu, D. Ticoş, and C. M. Ticoş, "Chaotic oscillations of vertically aligned microrods in a plasma sheath," IEEE Trans. Plasma Sci. **51**, 835–846 (2023).
[10]V. Nosenko, F. Luoni, A. Kaouk, M. Rubin-Zuzic, and H. Thomas, "Active janus particles in a complex plasma," Phys. Rev. Res. **2**, 033226 (2020).
[11]V. Nosenko, "Two-dimensional complex (dusty) plasma with active Janus particles," Phys. Plasmas **29**, 123701 (2022).
[12]S. Okuzumi, "Electric charging of dust aggregates and its effect on dust coagulation in protoplanetary disks," Astrophys. J. **698**, 1122–1135 (2009).
[13]S. Okuzumi, H. Tanaka, T. Takeuchi, and M.-a. Sakagami, "Electrostatic barrier against dust growth in protoplanetary disks. I. Classifying the evolution of size distribution," Astrophys. J. **731**, 95 (2011a).
[14]S. Okuzumi, H. Tanaka, T. Takeuchi, and M.-a. Sakagami, "Electrostatic barrier against dust growth in protoplanetary disks. II. Measuring the size of the "frozen" zone," Astrophys. J. **731**, 96 (2011b).
[15]A. V. Ivlev, V. V. Akimkin, and P. Caselli, "Ionization and dust charging in protoplanetary disks," Astrophys. J. **833**, 92 (2016).
[16]V. V. Akimkin, A. V. Ivlev, and P. Caselli, "Inhibited coagulation of micron-size dust due to the electrostatic barrier," Astrophys. J. **889**, 64 (2020).
[17]J. Abrahamson and J. Marshall, "Permanent electric dipoles on gas-suspended particles and the production of filamentary aggregates," J. Electrostat. **55**, 43–63 (2002).
[18]L. S. Matthews, V. Land, and T. W. Hyde, "Charging and coagulation of dust in protoplanetary plasma environments," Astrophys. J. **744**, 8 (2012).
[19]Q. Ma, L. S. Matthews, V. Land, and T. W. Hyde, "Charging of aggregate grains in astrophysical environments," ApJ. **763**, 77 (2013).
[20]L. S. Matthews, D. A. Coleman, and T. W. Hyde, "Multipole expansions of aggregate charge: How far to go?," IEEE Trans. Plasma Sci. **44**, 519–524 (2016).
[21]R. Yousefi, A. B. Davis, J. Carmona-Reyes, L. S. Matthews, and T. W. Hyde, "Measurement of net electric charge and dipole moment of dust aggregates in a complex plasma," Phys. Rev. E: Stat. Nonlinear Soft Matter Phys. **90**, 033101 (2014).
[22]E. Whipple, T. G. Northrop, and D. A. Mendis, "The electrostatics of a dusty plasma," J. Geophys. Res.: Space Phys. **90**, 7405–7413, https://doi.org/10.1029/JA090iA08p07405 (1985).
[23]J. E. Allen, "Probe theory - the orbital motion approach," Phys. Scr. **45**, 497–503 (1992).
[24]A. Piel, *Plasma Physics – An Introduction to Laboratory, Space, and Fusion Plasmas*, 2nd ed. (Springer, 2017).
[25]A. Melzer, *Physics of Dusty Plasmas – An Introduction*, 1st ed. (Springer Nature Switzerland AG, 2019).
[26]I. H. Hutchinson, "Ion collection by a sphere in a flowing plasma: 3. Floating potential and drag force," Plasma Phys. Controlled Fusion **47**, 71–87 (2005).
[27]J. Manweiler, T. Armstrong, and T. Cravens, "Complex charge distributions of dielectric dust grains due to plasma flow," J. Plasma Phys. **63**, 269–283 (2000).
[28]G. Lapenta, "Dipole moments on dust particles immersed in anisotropic plasmas," Phys. Rev. Lett. **75**, 4409–4412 (1995).
[29]G. Lapenta, "Simulation of charging and shielding of dust particles in drifting plasmas," Phys. Plasmas **6**, 1442–1447 (1999).
[30]S. Khrapak and G. Morfill, "Basic processes in complex (dusty) plasmas: Charging, interactions, and ion drag force," Contrib. Plasma Phys. **49**, 148–168 (2009).
[31]N. Meyer-Vernet, "Flip-flop of electric potential of dust grains in space," Astron. Astrophys. **105**, 98–106 (1982).
[32]L. Wörner, A. V. Ivlev, L. Couëdel, P. Huber, M. Schwabe, T. Hagl, M. Mikikian, L. Boufendi, A. Skvortsov, A. M. Lipaev, V. I. Molotkov, O. F. Petrov, V. E. Fortov, H. M. Thomas, and G. E. Morfill, "The effect of a direct current field on the microparticle charge in the plasma afterglow," Phys. Plasmas **20**, 123702 (2013).
[33]B. van Minderhout, J. C. A. van Huijstee, B. Platier, T. Peijnenburg, P. Blom, G. M. W. Kroesen, and J. Beckers, "Charge control of micro-particles in a shielded plasma afterglow," Plasma Sources Sci. Technol. **29**, 065005 (2020).
[34]N. Chaubey, J. Goree, S. J. Lanham, and M. J. Kushner, "Positive charging of grains in an afterglow plasma is enhanced by ions drifting in an electric field," Phys. Plasmas **28**, 103702 (2021).
[35]N. Chaubey and J. Goree, "Controlling the charge of dust particles in a plasma afterglow by timed switching of an electrode voltage," J. Phys. D: Appl. Phys. **56**, 375202 (2023).

[36]N. Chaubey and J. Goree, "Controlling the charge of dust particles in an afterglow by modulating the plasma power," J. Phys. D: Appl. Phys. **57**, 205202 (2024).
[37]C. Cui and J. Goree, "Fluctuations of the charge on a dust grain in a plasma," IEEE Trans. Plasma Sci. **22**, 151–158 (1994).
[38]G. I. Sukhinin, A. V. Fedoseev, and M. V. Salnikov, "The influence of dust particle geometry on its charge and plasma potential," Contrib. Plasma Phys. **59**, 201800153 (2019).
[39]G. Sukhinin, Salnikov, and Fedoseev, "Plasma anisotropy around non-spherical conductive dust particle," Phys. Sci. Technol. **6**, 37–43 (2019).
[40]C. Maxwell, "On the electrical capacity of a long narrow cylinder, and of a disk of sensible thickness," Proc. London Math. Soc. **s1-9**, 94–102 (1877).
[41]J. D. Jackson, "Charge density on thin straight wire, revisited," Am. J. Phys. **68**, 789–799 (2000).
[42]G. V. Kraniotis and G. K. Leontaris, "Closed form solution for the surface area, the capacitance and the demagnetizing factors of the ellipsoid," arXiv:1306.0509v1 (2013).
[43]J. Lekner, "Capacitance coefficients of two spheres," J. Electrostat. **69**, 11–14 (2011).
[44]O. H. Asnaz, H. Jung, F. Greiner, and A. Piel, "Charging of an irregularly shaped particle in the sheath of an RF plasma," Phys. Plasmas **25**, 073702 (2018).
[45]B. van Minderhout, J. C. A. van Huijstee, R. M. H. Rompelberg, A. Post, A. T. A. Peijnenburg, P. Blom, and J. Beckers, "Charge of clustered microparticles measured in spatial plasma afterglows follows the smallest enclosing sphere model," Nat. Commun. **12**, 4692 (2021).
[46]A. Semechko, see https://github.com/AntonSemechko/Bounding-Spheres-And-Circles for "Exact Minimum bounding spheres and circles" (2019).
[47]E. Welzl, "Smallest enclosing disks (balls and ellipsoids)," in *New Results and New Trends in Computer Science*, Lecture Notes in Computer Science Vol. 555, edited by H. Maurer (Springer, Berlin, Heidelberg, 1991), pp. 359–370.
[48]R. Gopalakrishnan, T. Thajudeen, and C. J. Hogan, "Collision limited reaction rates for arbitrarily shaped particles across the entire diffusive Knudsen number range," J. Chem. Phys. **135**, 054302 (2011).
[49]A. Mengel, "Numerical calculation of the orientation-averaged projected area of an aggregate of spheres," opendata (2024).
[50]L. S. Matthews, B. Shotorban, and T. W. Hyde, "Discrete stochastic charging of aggregate grains," Phys. Rev. E **97**, 053207 (2018).
[51]D. Paszun and C. Dominik, "Collisional evolution of dust aggregates. from compaction to catastrophic destruction," Astron. Astrophys. **507**, 1023–1040 (2009).
[52]A. Mengel, M. Artz, and F. Greiner, "Pulse excited oscillation: A new high-precision excitation method for the charge-to-mass ratio determination of microparticles in plasma and comparison to stepwise excitation and the phase-resolved resonance method," Phys. Plasmas **30**, 123704 (2023).
[53]H. Jung, F. Greiner, O. H. Asnaz, J. Carstensen, and A. Piel, "Resonance methods for the characterization of dust particles in plasmas," J. Plasma Phys. **82**, 615820301 (2016).
[54]G. Lapenta, "Ion flow induced attractive force in complex plasma crystals," Phys.Scr. **64**, 599–604 (2001).
[55]I. H. Hutchinson, "Spin stability of asymmetrically charged plasma dust," New J. Phys. **6**, 43 (2004).
[56]K. S. Ashrafi, R. Yousefi, M. Chen, L. S. Matthews, and T. W. Hyde, "Dust as probes: Determining confinement and interaction forces," Phys. Rev. E **102**, 043210 (2020).
[57]L. S. Matthews, D. L. Sanford, E. G. Kostadinova, K. S. Ashrafi, E. Guay, and T. W. Hyde, "Dust charging in dynamic ion wakes," Phys. Plasmas **27**, 023703 (2020).
[58]See https://www.microparticles-shop.de for the website of microparticles GmbH.
[59]P. S. Epstein, "On the resistance experienced by spheres in their motion through gases," Phys. Rev. **23**, 710 (1924).
[60]A. Mengel, F. X. Bronold, and F. Greiner, "Evidence of different charging behavior of conductive and dielectric materials in low-temperature plasmas and a new diagnostic for low-energy electron absorption," Phys. Rev. Lett. **133**, 185301 (2024).
[61]V. R. M. Pola, R. K. Desu, and R. K. Annabattula, "Voxelization based packing analysis for discrete element simulations of non-spherical particles," arXiv:2110.14151v1 (2021).
[62]I. König, A. Mengel, and F. Greiner, "Electron sticking coefficients of dusty plasma relevant materials," Phys. Plasmas **32**, 024501 (2025).
[63]S. Li, X. Dang, X. Yu, G. Abbas, Q. Zhang, and L. Cao, "The application of dielectric barrier discharge non-thermal plasma in vocs abatement: A review," Chem. Eng. J. **388**, 124275 (2020).
[64]K. Ollegott, P. Wirth, C. Oberste-Beulmann, P. Awakowicz, and M. Muhler, "Fundamental properties and applications of dielectric barrier discharges in plasma–catalytic processes at atmospheric pressure," Chem. Ing. Tech. **92**, 1542–1558 (2020).
[65]S. Roy, B. Choudhury, J. Johnson, and A. Schindler-Tyka, "Application of dielectric barrier discharge for improving food shelf life and reducing spoilage," Sci. Rep. **11**, 19200 (2021).
[66]J. He, X. Wen, L. Wu, H. Chen, J. Hu, and X. Hou, "Dielectric barrier discharge plasma for nanomaterials: Fabrication, modification and analytical applications," TrAC, Trends Anal. Chem. **156**, 116715 (2022).

Bibliography

[1] F. X. Bronold and H. Fehske, "Microscopic theory of electron absorption by plasma-facing surfaces", Plasma Physics and Controlled Fusion **59**, 014011 (2017).

[2] M. A. Lieberman and A. J. Lichtenberg, *Principles of plasma discharges and materials processing*, 2nd ed. (Wiley-Interscience, Hoboken N.J., 2005), ISBN: 0-471-72001-1.

[3] R. d'Agostino, P. Favia, C. Oehr, and M. R. Wertheimer, "Low–temperature plasma processing of materials: Past, present, and future", Plasma Processes and Polymers **2**, 7–15 (2005).

[4] A. A. Fridman, *Plasma physics and engineering*, 2nd ed. (CRC Press, Hoboken, 2011), ISBN: 9781439812280.

[5] P. J. Bruggeman, F. Iza, and R. Brandenburg, "Foundations of atmospheric pressure non-equilibrium plasmas", Plasma Sources Science and Technology **26**, 123002 (2017).

[6] K.-D. Weltmann, J. F. Kolb, M. Holub, D. Uhrlandt, M. Šimek, K. Ostrikov, S. Hamaguchi, U. Cvelbar, M. Černák, B. Locke, A. Fridman, P. Favia, and K. Becker, "The future for plasma science and technology", Plasma Processes and Polymers **16**, 1800118 (2019).

[7] G. Franz, *Low pressure plasmas and microstructuring technology* (Springer, Berlin, Heidelberg, Germany, 2009), ISBN: 9783540858492.

[8] D. J. Economou, "Pulsed plasma etching for semiconductor manufacturing", Journal of Physics D: Applied Physics **47**, 303001 (2014).

[9] K. Racka-Szmidt, B. Stonio, J. Żelazko, M. Filipiak, and M. Sochacki, "A review: Inductively coupled plasma reactive ion etching of silicon carbide", Materials **15**, 123 (2021).

[10] L. Martinu and D. Poitras, "Plasma deposition of optical films and coatings: A review", Journal of Vacuum Science & Technology A **18**, 2619–2645 (2000).

[11] S. O. Mbam, S. E. Nwonu, O. A. Orelaja, U. S. Nwigwe, and X.-F. Gou, "Thin-film coating; Historical evolution, conventional deposition technologies, stress-state micro/nano-level measurement/models and prospects projection: A critical review", Materials Research Express **6**, 122001 (2019).

[12] B. Fotovvati, N. Namdari, and A. Dehghanghadikolaei, "On coating techniques for surface protection: A review", Journal of Manufacturing and Materials Processing **3**, 28 (2019).

[13] Y. Deng, W. Chen, B. Li, C. Wang, T. Kuang, and Y. Li, "Physical vapor deposition technology for coated cutting tools: a review", Ceramics International **46**, 18373–18390 (2020).

[14] F. Simchen, M. Sieber, A. Kopp, and T. Lampke, "Introduction to plasma electrolytic oxidation—An overview of the process and applications", Coatings **10**, 628 (2020).

[15] S. K. Pankaj, C. Bueno-Ferrer, N. N. Misra, V. Milosavljević, C. P. O'Donnell, P. Bourke, K. M. Keener, and P. J. Cullen, "Applications of cold plasma technology in food packaging", Trends in Food Science & Technology **35**, 5–17 (2014).

[16] M. Gebhard, F. Mitschker, C. Hoppe, M. Aghaee, D. Rogalla, M. Creatore, G. Grundmeier, P. Awakowicz, and A. Devi, "A combinatorial approach to enhance barrier properties of thin films on polymers: Seeding and capping of PECVD thin films by PEALD", Plasma Processes and Polymers **15**, 1700209 (2018).

[17] P. K. Chu, J. Y. Chen, L. P. Wang, and N. Huang, "Plasma-surface modification of biomaterials", Materials Science and Engineering: R: Reports **36**, 143–206 (2002).

[18] H. T. Sasmazel, M. Alazzawi, and N. K. A. Alsahib, "Atmospheric pressure plasma surface treatment of polymers and influence on cell cultivation", Molecules **26**, 1665 (2021).

[19] A. A. Fridman, *Plasma chemistry* (Cambridge Univ. Press, Cambridge and New York, 2008), ISBN: 978-0-521-84735-3.

[20] A. Bogaerts, X. Tu, J. C. Whitehead, G. Centi, L. Lefferts, O. Guaitella, F. Azzolina-Jury, H.-H. Kim, A. B. Murphy, W. F. Schneider, T. Nozaki, J. C. Hicks, A. Rousseau, F. Thevenet, A. Khacef, and M. Carreon, "The 2020 plasma catalysis roadmap", Journal of Physics D: Applied Physics **53**, 443001 (2020).

[21] D. Mei, X. Zhu, C. Wu, B. Ashford, P. T. Williams, and X. Tu, "Plasma-photocatalytic conversion of CO_2 at low temperatures: Understanding the synergistic effect of plasma-catalysis", Applied Catalysis B: Environmental **182**, 525–532 (2016).

[22] G. Chen, N. Britun, T. Godfroid, V. Georgieva, R. Snyders, and M.-P. Delplancke-Ogletree, "An overview of CO_2 conversion in a microwave discharge: The role of plasma-catalysis", Journal of Physics D: Applied Physics **50**, 084001 (2017).

[23] K. M. Bal, S. Huygh, A. Bogaerts, and E. C. Neyts, "Effect of plasma-induced surface charging on catalytic processes: Application to CO_2 activation", Plasma Sources Science and Technology **27**, 024001 (2018).

[24] R. Snoeckx and A. Bogaerts, "Plasma technology - a novel solution for CO_2 conversion?", Chemical Society Reviews **46**, 5805–5863 (2017).

[25] A. Jafarzadeh, K. M. Bal, A. Bogaerts, and E. C. Neyts, "Activation of CO_2 on Copper surfaces: The synergy between electric field, surface morphology, and excess electrons", The Journal of Physical Chemistry C **124**, 6747–6755 (2020).

[26] A. George, B. Shen, M. Craven, Y. Wang, D. Kang, C. Wu, and X. Tu, "A review of non-thermal plasma technology: A novel solution for CO_2 conversion and utilization", Renewable and Sustainable Energy Reviews **135**, 109702 (2021).

[27] E. C. Neyts, "Plasma-surface interactions in plasma catalysis", Plasma Chemistry and Plasma Processing **36**, 185–212 (2016).

[28] S. Zhang and G. S. Oehrlein, "From thermal catalysis to plasma catalysis: A review of surface processes and their characterizations", Journal of Physics D: Applied Physics **54**, 213001 (2021).

[29] N. Hershkowitz, R. L. Goettsch, C. Chan, K. Hendricks, and R. T. Carpenter, "Detection of secondary electrons in a multidipole plasma", Journal of Applied Physics **53**, 5330–5332 (1982).

[30] Y. Ohtsu and H. Fujita, "Production of high-density capacitively coupled radio-frequency discharge plasma by high-secondary-electron-emission oxide", Applied Physics Letters **85**, 4875–4877 (2004).

[31] T. Lafleur, P. Chabert, and J. P. Booth, "Secondary electron induced asymmetry in capacitively coupled plasmas", Journal of Physics D: Applied Physics **46**, 135201 (2013).

[32] I. Korolov, A. Derzsi, Z. Donkó, and J. Schulze, "The influence of the secondary electron induced asymmetry on the electrical asymmetry effect in capacitively coupled plasmas", Applied Physics Letters **103**, 064102 (2013).

[33] S. Wilczek, J. Trieschmann, J. Schulze, E. Schuengel, R. P. Brinkmann, A. Derzsi, I. Korolov, Z. Donkó, and T. Mussenbrock, "The effect of the driving frequency on the confinement of beam electrons and plasma density in low-pressure capacitive discharges", Plasma Sources Science and Technology **24**, 024002 (2015).

[34] I. Korolov, A. Derzsi, Z. Donkó, E. Schüngel, and J. Schulze, "The influence of electron reflection/sticking coefficients at the electrodes on plasma parameters in particle-in-cell simulations of capacitive radio-frequency plasmas", Plasma Sources Science and Technology **25**, 015024 (2016).

[35] C. Schulze, Z. Donkó, and J. Benedikt, "A computationally assisted technique to measure material-specific surface coefficients in capacitively coupled plasmas based on characteristics of the ion flux-energy distribution function", Plasma Sources Science and Technology **31**, 105017 (2022).

[36] R. Masheyeva, P. Hartmann, L.-Y. Luo, K. Dzhumagulova, Y.-X. Liu, J. Schulze, and Z. Donkó, "On the in-situ determination of the effective secondary electron emission coefficient in low pressure capacitively coupled radio frequency discharges based on the electrical asymmetry effect", Journal of Physics D: Applied Physics **58**, 045208 (2025).

[37] P. F. Ambrico, M. Ambrico, L. Schiavulli, T. Ligonzo, and V. Augelli, "Charge trapping induced by plasma in alumina electrode surface investigated by thermoluminescence and optically stimulated luminescence", Applied Physics Letters **94**, 051501 (2009).

[38] P. F. Ambrico, M. Ambrico, A. Colaianni, L. Schiavulli, G. Dilecce, and S. de Benedictis, "Thermoluminescence study of the trapped charge at an alumina surface electrode in different dielectric barrier discharge regimes", Journal of Physics D: Applied Physics **43**, 325201 (2010).

[39] A. D. Lele, Y. Xu, and Y. Ju, "Modelling the effect of surface charging on plasma synthesis of ammonia using DFT", Physical Chemistry Chemical Physics **26**, 9453–9461 (2024).

[40] M. G. Kong, G. Kroesen, G. Morfill, T. Nosenko, T. Shimizu, J. van Dijk, and J. L. Zimmermann, "Plasma medicine: An introductory review", New Journal of Physics **11**, 115012 (2009).

[41] S. Schneider, J.-W. Lackmann, F. Narberhaus, J. E. Bandow, B. Denis, and J. Benedikt, "Separation of VUV/UV photons and reactive particles in the effluent of a He/O_2 atmospheric pressure plasma jet", Journal of Physics D: Applied Physics **44**, 295201 (2011).

[42] A. A. Fridman and G. Friedman, *Plasma medicine* (John Wiley & Sons, Chichester West Sussex U.K., 2013), ISBN: 978-0-470-68969-1.

[43] Q. Zhang, J. Zhuang, T. von Woedtke, J. F. Kolb, J. Zhang, J. Fang, and K.-D. Weltmann, "Synergistic antibacterial effects of treatments with low temperature plasma jet and pulsed electric fields", Applied Physics Letters **105**, 104103 (2014).

[44] A. Lin, N. Chernets, J. Han, Y. Alicea, D. Dobrynin, G. Fridman, T. A. Freeman, A. Fridman, and V. Miller, "Non-equilibrium dielectric barrier discharge treatment of mesenchymal stem cells: Charges and reactive oxygen species play the major role in cell death", Plasma Processes and Polymers **12**, 1117–1127 (2015).

[45] S. Schneider, F. Jarzina, J.-W. Lackmann, J. Golda, V. Layes, V. Schulz-von der Gathen, J. E. Bandow, and J. Benedikt, "Summarizing results on the performance of a selective set of atmospheric plasma jets for separation of photons and reactive particles", Journal of Physics D: Applied Physics **48**, 444001 (2015).

[46] C. M. Wolff, J. F. Kolb, K.-D. Weltmann, T. von Woedtke, and S. Bekeschus, "Combination treatment with cold physical plasma and pulsed electric fields augments ROS production and cytotoxicity in lymphoma", Cancers **12**, 845 (2020).

[47] S. E. DeForest, "Spacecraft charging at synchronous orbit", Journal of Geophysical Research: Space Physics **77**, 651–659 (1972).

[48] A. Rosen, "Spacecraft charging: Environment-induced anomalies", Journal of Spacecraft and Rockets **13**, 129–136 (1976).

[49] E. C. Whipple, "Potentials of surfaces in space", Reports on Progress in Physics **44**, 1197–1250 (1981).

[50] L. K. Sarno-Smith, B. A. Larsen, R. M. Skoug, M. W. Liemohn, A. Breneman, J. R. Wygant, and M. F. Thomsen, "Spacecraft surface charging within geosynchronous orbit observed by the Van Allen probes", Space Weather **14**, 151–164 (2016).

[51] J.-C. Matéo–Vélez, A. Sicard, D. Payan, N. Ganushkina, N. P. Meredith, and I. Sillanpää, "Spacecraft surface charging induced by severe environments at geosynchronous orbit", Space Weather **16**, 89–106 (2018).

[52] N. Y. Ganushkina, B. Swiger, S. Dubyagin, J.-C. Matéo–Vélez, M. W. Liemohn, A. Sicard, and D. Payan, "Worst–case severe environments for surface charging observed at LANL satellites as dependent on solar wind and geomagnetic conditions", Space Weather **19**, e2021SW002732 (2021).

[53] J. I. Minow, V. K. Jordanova, D. Pitchford, N. Y. Ganushkina, Y. Zheng, G. Luca Delzanno, I. Jun, and W. Kim, "ISWAT spacecraft surface charging review", Advances in Space Research, 10.1016/j.asr.2024.08.058 (2024).

[54] A. Piel, *Plasma physics: An introduction to laboratory, space, and fusion plasmas* (Springer Berlin Heidelberg, Berlin, Heidelberg, 2010), ISBN: 978-3-642-10490-9.

[55] A. Melzer, *Lecture notes in physics*, Vol. 962: *Physics of dusty plasmas: An introduction* (Springer International Publishing, Cham, 2019), ISBN: 978-3-030-20259-0.

[56] C. K. Goertz, "Kinetic Alfvén waves on auroral field lines", Planetary and Space Science **32**, 1387–1392 (1984).

[57] O. Havnes, T. K. Aanesen, and F. Melandsø, "On dust charges and plasma potentials in a dusty plasma with dust size distribution", Journal of Geophysical Research: Space Physics **95**, 6581–6585 (1990).

[58] I. Goertz, F. Greiner, and A. Piel, "Effects of charge depletion in dusty plasmas", Physics of Plasmas **18**, 013703 (2011).

[59] A. Petersen, O. H. Asnaz, B. Tadsen, and F. Greiner, "Decoupling of dust cloud and embedding plasma for high electron depletion in nanodusty plasmas", Communications Physics **5**, 1–8 (2022).

[60] A. A. Fridman, L. Boufendi, T. Hbid, B. V. Potapkin, and A. Bouchoule, "Dusty plasma formation: Physics and critical phenomena. Theoretical approach", Journal of Applied Physics **79**, 1303–1314 (1996).

[61] U. Kortshagen and U. Bhandarkar, "Modeling of particulate coagulation in low pressure plasmas", Physical review. E, Statistical physics, plasmas, fluids, and related interdisciplinary topics **60**, 887–898 (1999).

[62] L. Bröcker, G. S. Perlick, and C.-P. Klages, "Evidence of ionic film deposition from single–filament dielectric barrier discharges in Ar–HMDSO mixtures", Plasma Processes and Polymers **17**, 2000129 (2020).

[63] D. Loffhagen, M. M. Becker, A. K. Czerny, and C.-P. Klages, "Modeling of atmospheric-pressure dielectric barrier discharges in argon with small admixtures of tetramethylsilane", Plasma Chemistry and Plasma Processing **41**, 289–334 (2021).

[64] S. Wohlfahrt, C. Wirtz, and D. Block, “Non-linear etch process of MF particles embedded in an rf plasma with oxygen admixture”, Physics of Plasmas **29**, 123702 (2022).

[65] K. Sgonina, C. Schulze, A. Quack, and J. Benedikt, “Vacuum–ultraviolet–photoionization chamber for the investigation of ion–based surface treatment and thin film deposition at atmospheric pressure”, Plasma Processes and Polymers **21**, 2400103 (2024).

[66] S. Wohlfahrt, “Änderung von Größe und Morphologie von Mikropartikeln im Plasma”, PhD Thesis (CAU, Kiel, 2025).

[67] Y. Gorbanev, J. Golda, V. Schulz-von der Gathen, and A. Bogaerts, “Applications of the COST plasma jet: More than a reference standard”, Plasma **2**, 316–327 (2019).

[68] K. Sgonina, G. Bruno, S. Wyprich, K. Wende, and J. Benedikt, “Reactions of plasma-generated atomic oxygen at the surface of aqueous phenol solution: Experimental and modeling study”, Journal of Applied Physics **130**, 043303 (2021).

[69] P. Gururani, P. Bhatnagar, B. Bisht, V. Kumar, N. C. Joshi, M. S. Tomar, and B. Pathak, “Cold plasma technology: Advanced and sustainable approach for wastewater treatment”, Environmental Science and Pollution Research **28**, 65062–65082 (2021).

[70] K. Kyere-Yeboah, I. K. Bique, and X.-C. Qiao, “Advances of non-thermal plasma discharge technology in degrading recalcitrant wastewater pollutants. A comprehensive review”, Chemosphere **320**, 138061 (2023).

[71] M. Bonitz, A. Filinov, J.-W. Abraham, K. Balzer, H. Kählert, E. Pehlke, F. X. Bronold, M. Pamperin, M. Becker, D. Loffhagen, and H. Fehske, “Towards an integrated modeling of the plasma-solid interface”, Frontiers of Chemical Science and Engineering **13**, 201–237 (2019).

[72] A. Chvyreva and A. J. M. Pemen, “Experimental investigation of electron emission from dielectric surfaces due to primary electron beam: A review”, IEEE Transactions on Dielectrics and Electrical Insulation **21**, 2274–2282 (2014).

[73] L. A. Gonzalez, M. Angelucci, R. Larciprete, and R. Cimino, “The secondary electron yield of noble metal surfaces”, AIP Advances **7**, 115203 (2017).

[74] C. J. Cook and W. J. Fredericks, “Interaction of slow electrons with insulating crystals. I. Absorption coefficient for cleaved alkali halides; Experimental techniques”, Journal of Applied Physics **32**, 860–866 (1961).

[75] C. J. Cook and W. J. Fredericks, “Interaction of 0.2- to 4.0-eV electron beams with cleaved MgO”, The Journal of Chemical Physics **36**, 608–611 (1962).

[76] J. F. Shackelford and W. Alexander, *CRC materials science and engineering handbook*, 3rd ed. (CRC Press, 2000), ISBN: 9780429117862.

[77] F. Greiner, *Towards a new method to measure low energy electron sticking coefficients using dusty plasmas*, German Research Foundation (DFG), project no. 443791209, https://gepris.dfg.de/gepris/projekt/443791209.

[78] R. Merlino, “Dusty plasmas: From Saturn’s rings to semiconductor processing devices”, Advances in Physics: X **6**, 1873859 (2021).

[79] A. Melzer, T. Trottenberg, and A. Piel, “Experimental determination of the charge on dust particles forming coulomb lattices”, Physics Letters A **191**, 301–308 (1994).

[80] H. Jung, F. Greiner, O. H. Asnaz, J. Carstensen, and A. Piel, “Resonance methods for the characterization of dust particles in plasmas”, Journal of Plasma Physics **82**, 615820301 (2016).

[81] P. Meijaard, T. J. A. Staps, and J. Beckers, “Step-wise excitation for the determination of the resonance frequency of a microparticle confined in a low pressure plasma”, Physics of Plasmas **28**, 083502 (2021).

[82] U. Konopka, L. Ratke, and H. M. Thomas, “Central collisions of charged dust particles in a plasma”, Physical Review Letters **79**, 1269–1272 (1997).

[83] Z. Zhang, K. Qiao, J. Kong, L. Matthews, and T. W. Hyde, “Simple method to measure the interaction potential of dielectric grains in a dusty plasma”, Physical review. E, Statistical, nonlinear, and soft matter physics **82**, 036401 (2010).

[84] J. Carstensen, F. Greiner, and A. Piel, “Determination of dust grain charge and screening lengths in the plasma sheath by means of a controlled cluster rotation”, Physics of Plasmas **17**, 083703 (2010).

[85] A. Melzer, S. Nunomura, D. Samsonov, Z. W. Ma, and J. Goree, “Laser-excited mach cones in a dusty plasma crystal”, Physical review. E, Statistical physics, plasmas, fluids, and related interdisciplinary topics **62**, 4162–4176 (2000).

[86] T. M. Flanagan and J. Goree, “Observation of the spatial growth of self-excited dust-density waves”, Physics of Plasmas **17**, 123702 (2010).

[87] K. O. Menzel, O. Arp, and A. Piel, “Spatial frequency clustering in nonlinear dust-density waves”, Physical review letters **104**, 235002 (2010).

[88] J. D. Williams, “Time-resolved measurement of global synchronization in the dust acoustic wave”, Physical review. E, Statistical, nonlinear, and soft matter physics **90**, 043103 (2014).

[89] V. V. Yaroshenko, S. A. Khrapak, M. Y. Pustylnik, H. M. Thomas, S. Jaiswal, A. M. Lipaev, A. D. Usachev, O. F. Petrov, and V. E. Fortov, “Excitation of low-frequency dust density waves in flowing complex plasmas”, Physics of Plasmas **26**, 033704 (2019).

[90] A. Melzer, H. Krüger, S. Schütt, and M. Mulsow, “Dust-density waves in radio-frequency discharges under magnetic fields”, Physics of Plasmas **27**, 033704 (2020).

[91] B. Tadsen, F. Greiner, S. Groth, and A. Piel, “Self-excited dust-acoustic waves in an electron-depleted nanodusty plasma”, Physics of Plasmas **22**, 113701 (2015).

[92] B. Tadsen, F. Greiner, and A. Piel, “Probing a dusty magnetized plasma with self-excited dust-density waves”, Physical review. E **97**, 033203 (2018).

[93] J. E. Allen, “Probe theory - the orbital motion approach”, Physica Scripta **45**, 497–503 (1992).

[94] E. C. Whipple, T. G. Northrop, and D. A. Mendis, “The electrostatics of a dusty plasma”, Journal of Geophysical Research: Space Physics **90**, 7405–7413 (1985).

[95] C. M. Ticoş, A. Dyson, and P. W. Smith, “The charge on falling dust particles in a rf plasma with dc negative bias”, Plasma Sources Science and Technology **13**, 395–402 (2004).

[96] N. Chaubey, J. Goree, S. J. Lanham, and M. J. Kushner, “Positive charging of grains in an afterglow plasma is enhanced by ions drifting in an electric field”, Physics of Plasmas **28**, 103702 (2021).

[97] N. Chaubey and J. Goree, “Controlling the charge of dust particles in a plasma afterglow by timed switching of an electrode voltage”, Journal of Physics D: Applied Physics **56**, 375202 (2023).

[98] N. Chaubey and J. Goree, “Controlling the charge of dust particles in an afterglow by modulating the plasma power”, Journal of Physics D: Applied Physics **57**, 205202 (2024).

[99] L. Wörner, A. V. Ivlev, L. Couëdel, P. Huber, M. Schwabe, T. Hagl, M. Mikikian, L. Boufendi, A. Skvortsov, A. M. Lipaev, V. I. Molotkov, O. F. Petrov, V. E. Fortov, H. M. Thomas, and G. E. Morfill, “The effect of a direct current field on the microparticle charge in the plasma afterglow”, Physics of Plasmas **20**, 123702 (2013).

[100] B. van Minderhout, T. Peijnenburg, P. Blom, J. M. Vogels, G. M. W. Kroesen, and J. Beckers, “The charge of micro-particles in a low pressure spatial plasma afterglow”, Journal of Physics D: Applied Physics **52**, 32LT03 (2019).

[101] B. van Minderhout, J. C. A. van Huijstee, B. Platier, T. Peijnenburg, P. Blom, G. M. W. Kroesen, and J. Beckers, “Charge control of micro-particles in a shielded plasma afterglow”, Plasma Sources Science and Technology **29**, 065005 (2020).

[102] B. van Minderhout, J. C. A. van Huijstee, R. M. H. Rompelberg, A. Post, A. T. A. Peijnenburg, P. Blom, and J. Beckers, “Charge of clustered microparticles measured in spatial plasma afterglows follows the smallest enclosing sphere model”, Nature Communications **12**, 4692 (2021).

[103] H. Krüger, E. Thiessen, F. X. Bronold, H. Fehske, and A. Melzer, “Charge measurement of SiO_2 nanoparticles in an rf plasma by IR absorption”, Physical review. E **104**, 045208 (2021).

[104] M. Hasani, G. Klaassen, Z. Marvi, M. Pustylnik, and J. Beckers, “Quantum dot photoluminescence as charge probe for plasma exposed surfaces”, en, Journal of Physics D: Applied Physics **56**, 025202 (2023).

[105] R. Wild and L. Stollenwerk, “Phase-resolved measurement of the spatial surface charge distribution in a laterally patterned barrier discharge”, New Journal of Physics **16**, 113040 (2014).

[106] C. Zafiu, A. Melzer, and A. Piel, "Nonlinear resonances of particles in a dusty plasma sheath", Physical review. E, Statistical, nonlinear, and soft matter physics **63**, 066403 (2001).

[107] P. S. Epstein, "On the resistance experienced by spheres in their motion through gases", Physical Review **23**, 710–733 (1924).

[108] J. Carstensen, H. Jung, F. Greiner, and A. Piel, "Mass changes of microparticles in a plasma observed by a phase-resolved resonance method", Physics of Plasmas **18**, 033701 (2011).

[109] J. Carstensen, F. Haase, H. Jung, B. Tadsen, S. Groth, F. Greiner, and A. Piel, "Probing the plasma sheath by the continuous mass loss of microparticles", IEEE Transactions on Plasma Science **41**, 764–768 (2013).

[110] O. H. Asnaz, H. Jung, F. Greiner, and A. Piel, "Size and density evolution of a single microparticle embedded in a plasma", Physics of Plasmas **24**, 083701 (2017).

[111] H. Jung, F. Greiner, A. Piel, and W. J. Miloch, "Experiments on wake structures behind a microparticle in a magnetized plasma flow", Physics of Plasmas **25**, 073703 (2018).

[112] O. H. Asnaz, H. Jung, F. Greiner, and A. Piel, "Charging of an irregularly shaped particle in the sheath of an rf plasma", Physics of Plasmas **25**, 073702 (2018).

[113] S. Peters, A. Homann, A. Melzer, and A. Piel, "Measurement of dust particle shielding in a plasma from oscillations of a linear chain", Physics Letters A **223**, 389–393 (1996).

[114] H. Schollmeyer, A. Melzer, A. Homann, and A. Piel, "Dust–dust and dust-plasma interactions of monolayer plasma crystals", Physics of Plasmas **6**, 2693–2698 (1999).

[115] B. Liu, J. Goree, V. E. Fortov, A. M. Lipaev, V. I. Molotkov, O. F. Petrov, G. E. Morfill, H. M. Thomas, H. Rothermel, and A. V. Ivlev, "Transverse oscillations in a single-layer dusty plasma under microgravity", Physics of Plasmas **16**, 083703 (2009).

[116] B. Liu, J. Goree, V. E. Fortov, A. M. Lipaev, V. I. Molotkov, O. F. Petrov, G. E. Morfill, H. M. Thomas, and A. V. Ivlev, "Dusty plasma diagnostics methods for charge, electron temperature, and ion density", Physics of Plasmas **17**, 053701 (2010).

[117] A. Homann, A. Melzer, and A. Piel, "Measuring the charge on single particles by laser-excited resonances in plasma crystals", Physical Review E **59**, R3835–R3838 (1999).

[118] W. W. Stoffels, E. Stoffels, G. H. P. M. Swinkels, M. Boufnichel, and G. M. W. Kroesen, "Etching a single micrometer-size particle in a plasma", Physical Review E **59**, 2302–2304 (1999).

[119] L. P. T. Schepers, J. Beckers, and W. L. IJzerman, "Determination of microparticle characteristics in an etching plasma", Contributions to Plasma Physics **58**, 985–994 (2018).

[120] S. Wohlfahrt and D. Block, "High-precision in situ measurements of size and optical properties of single microparticles in an rf plasma", Physics of Plasmas **28**, 123701 (2021).

[121] S. I. Krasheninnikov and R. D. Smirnov, "On the force exerted on a non-spherical asymmetric dust grain from homogeneous, stationary, isotropic, non-magnetized plasma", Physics of Plasmas **31**, 023702 (2024).

[122] J. Kong, T. W. Hyde, B. Harris, K. Qiao, and J. Carmona-Reyes, "Measurement of the vertical nonuniformity of the plasma sheath in a complex plasma", IEEE Transactions on Plasma Science **37**, 1620–1625 (2009).

[123] Ş. S. Bayin, *Mathematical methods in science and engineering* (John Wiley & Sons, Ltd, Hoboken, 2006), ISBN: 978-0-470-04142-0.

[124] G. F. Knoll, *Radiation detection and measurement*, 3rd ed. (Wiley, New York, NY and Weinheim, 2000), ISBN: 9780471073383.

[125] N. Balcon, D. Payan, M. Belhaj, T. Tondu, and V. Inguimbert, "Secondary electron emission on space materials: Evaluation of the total secondary electron yield from surface potential measurements", IEEE Transactions on Plasma Science **40**, 282–290 (2012).

[126] V. M. Dusevich, J. H. Purk, and J. D. Eick, "Choosing the right accelerating voltage for SEM (An introduction for beginners)", Microscopy Today **18**, 48–52 (2010).

[127] C. Davisson and L. H. Germer, "The scattering of electrons by a single crystal of nickel", Nature **119**, 558–560 (1927).

[128] K. Oura, V. G. Lifšic, A. Saranin, A. Zotov, and M. Katayama, *Surface science: An introduction*, Softcover reprint of the hardcover 1st ed., Physics and astronomy online library (Springer, Berlin and Heidelberg, 2003), ISBN: 3540005455.

[129] M. Henzler, "LEED studies of surface imperfections", Applications of Surface Science **11-12**, 450–469 (1982).

[130] M. Horn-von Hoegen, "Growth of semiconductor layers studied by spot profile analysing low energy electron diffraction", Zeitschrift für Kristallographie - Crystalline Materials **214**, 684–721 (1999).

[131] J. Schou, "Secondary electron emission from solids by electron and proton bombardment", Scanning Microscopy **2**, 607–632 (1988).

[132] G. F. Dionne, "Origin of secondary–electron–emission yield–curve parameters", Journal of Applied Physics **46**, 3347–3351 (1975).

[133] S. G. Ingram and N. S. J. Braithwaite, "Ion and electron energy analysis at a surface in an rf discharge", Journal of Physics D: Applied Physics **21**, 1496–1503 (1988).

[134] I. Langmuir, "Studies of electric discharges in gases at low pressures", General Electric Review **27**, 449, 538, 616, 762, 810 (1924).

[135] H. M. Mott-Smith and I. Langmuir, "The theory of collectors in gaseous discharges", Physical Review **28**, 727–763 (1926).

[136] F. X. Bronold and H. Fehske, “Absorption of an electron by a dielectric wall”, Physical review letters **115**, 225001 (2015).

[137] F. X. Bronold, K. Rasek, and H. Fehske, “Electron microphysics at plasma–solid interfaces”, Journal of Applied Physics **128**, 180908 (2020).

[138] F. X. Bronold and H. Fehske, “Invariant embedding approach to secondary electron emission from metals”, Journal of Applied Physics **131**, 113302 (2022).

[139] F. X. Bronold and F. Willert, “Electron surface scattering kernel for a plasma facing a semiconductor”, Physical review. E **110**, 035207 (2024).

[140] R. F. Dashen, “Theory of electron backscattering”, Physical Review **134**, A1025–A1032 (1964).

[141] C. D. Child, “Discharge from hot CaO”, en, Physical Review (Series I), 492–511 (1911).

[142] I. Langmuir, “The effect of space charge and residual gases on thermionic currents in high vacuum”, Physical Review **2**, 450–486 (1913).

[143] R. P. Brinkmann, “The plasma–sheath transition in low temperature plasmas: On the existence of a collisionally modified bohm criterion”, Journal of Physics D: Applied Physics **44**, 042002 (2011).

[144] A. Douglass, V. Land, L. Matthews, and T. Hyde, “Dust particle charge in plasma with ion flow and electron depletion near plasma boundaries”, Physics of Plasmas **18**, 083706 (2011).

[145] N. Kohlmann, F. Wieben, O. H. Asnaz, D. Block, and F. Greiner, “High-precision in-situ size measurements of single microparticles in an rf plasma”, Physics of Plasmas **26**, 053701 (2019).

[146] L. G. D’yachkov, A. G. Khrapak, S. A. Khrapak, and G. E. Morfill, “Model of grain charging in collisional plasmas accounting for collisionless layer”, Physics of Plasmas **14**, 042102 (2007).

[147] S. Khrapak and G. Morfill, “Basic processes in complex (dusty) plasmas: Charging, interactions, and ion drag force”, Contributions to Plasma Physics **49**, 148–168 (2009).

[148] A. Piel, H. Jung, and F. Greiner, “Molecular dynamics simulations of wake structures behind a microparticle in a magnetized ion flow. II. Effects of velocity spread and ion collisions”, Physics of Plasmas **25**, 083703 (2018).

[149] M. Lampe, T. B. Röcker, G. Joyce, S. K. Zhdanov, A. V. Ivlev, and G. E. Morfill, “Ion distribution function in a plasma with uniform electric field”, Physics of Plasmas **19**, 113703 (2012).

[150] F. W. Olver, *Nist handbook of mathematical functions* (Cambridge University Press, Cambridge, New York, and Melbourne, 2010), ISBN: 9780521192255.

[151] J. P. Verboncoeur, M. V. Alves, V. Vahedi, and C. K. Birdsall, “Simultaneous potential and circuit solution for 1D bounded plasma particle simulation codes”, Journal of Computational Physics **104**, 321–328 (1993).

[152] V. Vahedi, G. DiPeso, C. K. Birdsall, M. A. Lieberman, and T. D. Rognlien, "Capacitive rf discharges modelled by particle-in-cell Monte Carlo simulation. I. Analysis of numerical techniques", Plasma Sources Science and Technology **2**, 261–272 (1993).

[153] V. Vahedi, C. K. Birdsall, M. A. Lieberman, G. DiPeso, and T. D. Rognlien, "Capacitive rf discharges modelled by particle-in-cell Monte Carlo simulation. II. Comparisons with laboratory measurements of electron energy distribution functions", Plasma Sources Science and Technology **2**, 273–278 (1993).

[154] A. V. Phelps, "The application of scattering cross sections to ion flux models in discharge sheaths", Journal of Applied Physics **76**, 747–753 (1994).

[155] F. H. Harlow, M. Evans, and R. D. Richtmyer, "A machine calculation method for hydrodynamic problems", Los Alamos Scientific Laboratory of the University of California (1955).

[156] J. M. Dawson, "Particle simulation of plasmas", Reviews of Modern Physics **55**, 403–447 (1983).

[157] F. Haase, "Einfluss der elektrischen Leitfahigkeit auf die Aufladung von Staub in Plasmen", Bachelor Thesis (CAU, Kiel, 2012).

[158] M. Dapor, M. Ciappa, and W. Fichtner, "Monte carlo modeling in the low-energy domain of the secondary electron emission of polymethylmethacrylate for critical-dimension scanning electron microscopy", Journal of Micro/Nanolithography, MEMS, and MOEMS **9**, 023001 (2010).

[159] Y. Lin and D. C. Joy, "A new examination of secondary electron yield data", Surface and Interface Analysis **37**, 895–900 (2005).

[160] J. E. Daugherty and D. B. Graves, "Particulate temperature in radio frequency glow discharges", Journal of Vacuum Science & Technology A **11**, 1126–1131 (1993).

[161] G. H. P. M. Swinkels, H. Kersten, H. Deutsch, and G. M. W. Kroesen, "Microcalorimetry of dust particles in a radio-frequency plasma", Journal of Applied Physics **88**, 1747–1755 (2000).

[162] H. Maurer, R. Basner, and H. Kersten, "Measuring the temperature of microparticles in plasmas", The Review of scientific instruments **79**, Journal Article, 093508 (2008).

[163] M. Lampe, V. Gavrishchaka, G. Ganguli, and G. Joyce, "Effect of trapped ions on shielding of a charged spherical object in a plasma", Physical review letters **86**, 5278–5281 (2001).

[164] M. Lampe, R. Goswami, Z. Sternovsky, S. Robertson, V. Gavrishchaka, G. Ganguli, and G. Joyce, "Trapped ion effect on shielding, current flow, and charging of a small object in a plasma", Physics of Plasmas **10**, 1500–1513 (2003).

[165] Z. Sternovsky, M. Lampe, and S. Robertson, "Orbiting ions in the debye shielding cloud around dust particles in weakly collisional plasmas", IEEE Transactions on Plasma Science **32**, 632–636 (2004).

[166] F. X. Bronold, H. Fehske, H. Kersten, and H. Deutsch, "Towards a microscopic theory of particle charging", Contributions to Plasma Physics **49**, 303–315 (2009).

[167] C. Cui and J. Goree, "Fluctuations of the charge on a dust grain in a plasma", IEEE Transactions on Plasma Science **22**, 151–158 (1994).

[168] I. H. Hutchinson, "Spin stability of asymmetrically charged plasma dust", New Journal of Physics **6**, 43 (2004).

[169] O. Ishihara and N. Sato, "On the rotation of a dust particulate in an ion flow in a magnetic field", IEEE Transactions on Plasma Science **29**, 179–181 (2001).

[170] S. I. Krasheninnikov, V. I. Shevchenko, and P. K. Shukla, "Spinning of a charged dust particle in a magnetized plasma", Physics Letters A **361**, 133–135 (2007).

[171] R. Yousefi, A. B. Davis, J. Carmona-Reyes, L. S. Matthews, and T. W. Hyde, "Measurement of net electric charge and dipole moment of dust aggregates in a complex plasma", Physical review. E, Statistical, nonlinear, and soft matter physics **90**, 033101 (2014).

[172] B. M. Annaratone, A. G. Khrapak, A. V. Ivlev, G. Söllner, P. Bryant, R. Sütterlin, U. Konopka, K. Yoshino, M. Zuzic, H. M. Thomas, and G. E. Morfill, "Levitation of cylindrical particles in the sheath of an rf plasma", Physical review. E, Statistical, nonlinear, and soft matter physics **63**, 036406 (2001).

[173] A. V. Ivlev, A. G. Khrapak, S. A. Khrapak, B. M. Annaratone, G. Morfill, and K. Yoshino, "Rodlike particles in gas discharge plasmas: Theoretical model", Physical review. E, Statistical, nonlinear, and soft matter physics **68**, 026403 (2003).

[174] B. M. Annaratone, A. G. Khrapak, and G. E. Morfill, "Peculiar properties of rodlike particles levitating in the sheath of an rf plasma", IEEE Transactions on Plasma Science **37**, 1110–1115 (2009).

[175] N. Banu and C. M. Ticoş, "Precession of cylindrical dust particles in the plasma sheath", Physics of Plasmas **22**, 103704 (2015).

[176] B. M. Annaratone, A. V. Ivlev, V. E. Fortov, A. G. Khrapak, S. A. Khrapak, V. I. Molotkov, and G. E. Morfill, "Complex plasmas with rodlike particles", IEEE Transactions on Plasma Science **39**, 2732–2733 (2011).

[177] N. Udrea, M.-L. Mitu, A. Scurtu, D. Ticoş, and C. M. Ticoş, "Chaotic oscillations of vertically aligned microrods in a plasma sheath", IEEE Transactions on Plasma Science **51**, 835–846 (2023).

[178] S. A. Maiorov, "Charging of a rodlike grain in a plasma flow", Plasma Physics Reports **30**, 766–771 (2004).

[179] W. J. Miloch, S. V. Vladimirov, H. L. Pécseli, and J. Trulsen, "Numerical simulations of potential distribution for elongated insulating dust being charged by drifting plasmas", Physical review. E, Statistical, nonlinear, and soft matter physics **78**, 036411 (2008).

[180] L. S. Matthews, V. Land, and T. W. Hyde, “Charging and coagulation of dust in protoplanetary plasma environments”, The Astrophysical Journal **744**, 8 (2012).

[181] G. I. Sukhinin, A. V. Fedoseev, and M. V. Salnikov, “The influence of dust particle geometry on its charge and plasma potential”, Contributions to Plasma Physics **59**, 201800153 (2019).

[182] L. S. Matthews, D. A. Coleman, and T. W. Hyde, “Multipole expansions of aggregate charge: How far to go?”, IEEE Transactions on Plasma Science **44**, 519–524 (2016).

[183] L. S. Matthews, B. Shotorban, and T. W. Hyde, “Discrete stochastic charging of aggregate grains”, Physical review. E **97**, 053207 (2018).

[184] G. Sukhinin, M. Salnikov, and A. Fedoseev, “Plasma anisotropy around non-spherical conductive dust particle”, Physical Sciences and Technology **6**, 37–43 (2019).

[185] C. Maxwell, “On the electrical capacity of a long narrow cylinder, and of a disk of sensible thickness”, Proceedings of the London Mathematical Society **s1-9**, 94–102 (1877).

[186] G. V. Kraniotis and G. K. Leontaris, “Closed form solution for the surface area, the capacitance and the demagnetizing factors of the ellipsoid”, arXiv: **1305.0509v1** (2013).

[187] J. Lekner, “Capacitance coefficients of two spheres”, Journal of Electrostatics **69**, 11–14 (2011).

[188] R. Gopalakrishnan, T. Thajudeen, and C. J. Hogan, “Collision limited reaction rates for arbitrarily shaped particles across the entire diffusive Knudsen number range”, The Journal of Chemical Physics **135**, 054302 (2011).

[189] X. Chen, T. Seto, U. R. Kortshagen, and C. J. Hogan, “Size and structural characterization of Si nanocrystal aggregates from a low pressure nonthermal plasma reactor”, Powder Technology **373**, 164–173 (2020).

[190] D. Paszun and C. Dominik, “Collisional evolution of dust aggregates. From compaction to catastrophic destruction”, Astronomy & Astrophysics **507**, 1023–1040 (2009).

[191] K. Wada, H. Tanaka, T. Suyama, H. Kimura, and T. Yamamoto, “Collisional growth conditions for dust aggregates”, The Astrophysical Journal **702**, 1490–1501 (2009).

[192] Y. Hasegawa, T. K. Suzuki, H. Tanaka, H. Kobayashi, and K. Wada, “Collisional growth and fragmentation of dust aggregates with low mass ratios. I. Critical collision velocity for water ice”, The Astrophysical Journal **915**, 22 (2021).

[193] S. Arakawa, H. Tanaka, and E. Kokubo, “Collisional growth efficiency of dust aggregates and its independence of the strength of interparticle rolling friction”, The Astrophysical Journal **939**, 100 (2022).

[194] E. N. Millán, M. B. Planes, E. M. Bringa, and M. G. Parisi, “Construction of granular aggregates with different porosity, shape, and size distributions”, Granular Matter **27**, 1–17 (2025).

[195] A. V. Filippov, M. Zurita, and D. E. Rosner, “Fractal-like aggregates: Relation between morphology and physical properties”, Journal of Colloid and Interface Science **229**, 261–273 (2000).

[196] V. R. M. Pola, R. K. Desu, and R. K. Annabattula, “Voxelization based packing analysis for discrete element simulations of non-spherical particles”, arXiv: **2110.14151v1** (2021).

[197] O. H. Asnaz, “In-situ Größenbestimmung einzelner Mikropartikel in Plasmen”, Master Thesis (CAU, Kiel, 2016).

[198] J. H. Pagán Muñoz, X. Wang, M. Horányi, V. Kvon, L. Heijmans, M. Chaudhuri, M. van de Kerkhof, A. M. Yakunin, P. Krainov, and D. Astakhov, “Charging and mobilization of dust particles on a surface in plasma”, Physical Review Letters **133**, 115301 (2024).

[199] M. Mecklenburg, A. Schuchardt, Y. K. Mishra, S. Kaps, R. Adelung, A. Lotnyk, L. Kienle, and K. Schulte, “Aerographite: Ultra lightweight, flexible nanowall, carbon microtube material with outstanding mechanical performance”, Advanced Materials **24**, 3437 (2012).

[200] I. Hölken, G. Neubüser, V. Postica, L. Bumke, O. Lupan, M. Baum, Y. K. Mishra, L. Kienle, and R. Adelung, “Sacrificial template synthesis and properties of 3D hollow-silicon nano- and microstructures”, ACS Applied Materials & Interfaces **8**, 20491–20498 (2016).

[201] F. Rasch, F. Schütt, L. M. Saure, S. Kaps, J. Strobel, O. Polonskyi, A. S. Nia, M. R. Lohe, Y. K. Mishra, F. Faupel, L. Kienle, X. Feng, and R. Adelung, “Wet-chemical assembly of 2D nanomaterials into lightweight, microtube-shaped, and macroscopic 3D networks”, ACS Applied Materials & Interfaces **11**, 44652–44663 (2019).

[202] I. Plesco, V. Ciobanu, T. Braniste, V. Ursaki, F. Rasch, A. Sarua, S. Raevschi, R. Adelung, J. Dutta, and I. Tiginyanu, “Highly porous and ultra-lightweight aero-Ga2O3: Enhancement of photocatalytic activity by noble metals”, Materials **14**, 1985 (2021).

[203] L. M. Saure, N. Kohlmann, H. Qiu, S. Shetty, A. Shaygan Nia, N. Ravishankar, X. Feng, A. Szameit, L. Kienle, R. Adelung, and F. Schütt, “Hybrid aeromaterials for enhanced and rapid volumetric photothermal response”, ACS Nano **17**, 22444–22455 (2023).

[204] K. Hansen, “Charakterisierung von Plasmen in Aeromaterialien”, Master Thesis (CAU, Kiel, 2024).

[205] I. König, “Nicht-sphärische Mikroteilchen in der Plasmarandschicht”, Master Thesis (CAU, Kiel, 2024).

[206] D. Geelen, J. Jobst, E. E. Krasovskii, S. J. van der Molen, and R. M. Tromp, “Nonuniversal transverse electron mean free path through few-layer graphene”, Physical review letters **123**, 086802 (2019).

[207] W. S. M. Werner, “Questioning a universal law for electron attenuation”, Physics **12**, 93 (2019).

[208] *Srem: the stopping and range of electrons in matter*, (11.04.2014) http://www.srim.org/SREM.htm.

[209] F. Salvat, “Penelope 2018: a code system for monte carlo simulation of electron and photon transport”, Workshop proceedings, Barcelona, Spain, 28 January – 1 February 2019, OECD Publishing, Paris, 10.1787/32da5043-en (2019).

[210] M. P. Seah and W. A. Dench, “Quantitative electron spectroscopy of surfaces: A standard data base for electron inelastic mean free paths in solids”, Surface and Interface Analysis **1**, 2–11 (1979).

[211] S. Bauer and N. Stock, “MOFs – Metallorganische Gerüststrukturen. Funktionale poröse Materialien”, Chemie in unserer Zeit **42**, 12–19 (2008).

[212] H. Furukawa, K. E. Cordova, M. O’Keeffe, and O. M. Yaghi, “The chemistry and applications of metal-organic frameworks”, Science **341**, 1230444 (2013).

[213] H. Rohr, “Synthese von Zeolith-ähnlichen Imidazolat-Gerüstverbindungen und Behandlung mit nicht-thermischem Plasma”, Master Thesis (CAU, Kiel, 2023).

[214] A. Quack, “Plasma-assisted catalysis with metal-organic-frameworks and non-thermal atmospheric pressure plasma”, Master Thesis (CAU, Kiel, 2023).

[215] V. Vahedi, C. K. Birdsall, M. A. Lieberman, G. DiPeso, and T. D. Rognlien, “Verification of frequency scaling laws for capacitive radio-frequency discharges using two-dimensional simulations”, Physics of Fluids B: Plasma Physics **5**, 2719–2729 (1993).

[216] C. K. Birdsall, D. Cooperberg, V. P. Gopinath, P. Mirrashidi, V. Vahedi, and J. Verboncoeur, “XPDC2-Rθ: A two dimensional electrostatic PIC code”, International Conference on Plasma Science (papers in summary form only received), Madison, WI, USA, pp. 204- (1995).

[217] V. Vahedi and G. DiPeso, “Simultaneous potential and circuit solution for two-dimensional bounded plasma simulation codes”, Journal of Computational Physics **131**, 149–163 (1997).

[218] *The plasma theory and simulation group*, https://ptsg.egr.msu.edu/.

[219] P. Parodi and F. Petronio, “Step-by-step verification of particle-in-cell Monte Carlo collision codes”, Physics of Plasmas **32**, 013902 (2025).

[220] T. Shirakawa and H. Sugai, “Plasma oscillation method for measurements of absolute electron density in plasma”, Japanese Journal of Applied Physics **32**, 5129 (1993).

[221] A. Schwabedissen, E. C. Benck, and J. R. Roberts, “Comparison of electron density measurements in planar inductively coupled plasmas by means of the plasma oscillation method and Langmuir probes”, Plasma Sources Science and Technology **7**, 119–129 (1998).

[222] J. Beckers, W. W. Stoffels, and G. M. W. Kroesen, “Temperature dependence of nucleation and growth of nanoparticles in low pressure Ar/CH4 RF discharges”, Journal of Physics D: Applied Physics **42**, 155206 (2009).

[223] F. M. J. H. van de Wetering, J. Beckers, and G. M. W. Kroesen, "Anion dynamics in the first 10 milliseconds of an argon–acetylene radio-frequency plasma", Journal of Physics D: Applied Physics **45**, 485205 (2012).

[224] B. Platier, T. Staps, P. Koelman, M. van der Schans, J. Beckers, and W. IJzerman, "Probing collisional plasmas with MCRS: Opportunities and challenges", Applied Sciences **10**, 4331 (2020).

[225] T. J. M. Donders and J. Beckers, "Real-time in situ monitoring of dust particle growth in a low-pressure nanodusty plasma based on laser-induced photodetachment", Applied Physics Letters **124**, 094101 (2024).

[226] J. W. Manweiler, T. P. Armstrong, and T. E. Cravens, "Complex charge distributions of dielectric dust grains due to plasma flow", Journal of Plasma Physics **63**, 269–283 (2000).

[227] L. Xin-Hua, X. Jia-Yue, J. Min, S. Hui, and L. Xiao-Min, "Electrical and optical properties of bulk ZnO single crystal grown by Flux Bridgman method", Chinese Physics Letters **23**, 3356–3358 (2006).

[228] S. S. Shariffudin, M. Salina, S. H. Herman, and M. Rusop, "Effect of film thickness on structural, electrical, and optical properties of sol-gel deposited layer-by-layer ZnO nanoparticles", Transactions on Electrical and Electronic Materials **13**, 102–105 (2012).

[229] A. Walther and A. H. E. Müller, "Janus particles: Synthesis, self-assembly, physical properties, and applications", Chemical reviews **113**, 5194–5261 (2013).

[230] V. Nosenko, F. Luoni, A. Kaouk, M. Rubin-Zuzic, and H. Thomas, "Active Janus particles in a complex plasma", Physical Review Research **2**, 033226 (2020).

[231] V. Nosenko, "Two-dimensional complex (dusty) plasma with active Janus particles", Physics of Plasmas **29**, 123701 (2022).

[232] S. W. S. Apolinario and F. M. Peeters, "Binary dusty plasma coulomb balls", Physical review. E, Statistical, nonlinear, and soft matter physics **83**, 041136 (2011).

[233] C. Killer, T. Bockwoldt, S. Schütt, M. Himpel, A. Melzer, and A. Piel, "Phase separation of binary charged particle systems with small size disparities using a dusty plasma", Physical review letters **116**, 115002 (2016).

[234] F. Wieben, J. Schablinski, and D. Block, "Generation of two-dimensional binary mixtures in complex plasmas", Physics of Plasmas **24**, 033707 (2017).

[235] S. Schütt, M. Himpel, and A. Melzer, "Experimental investigation of phase separation in binary dusty plasmas under microgravity", Physical review. E **101**, 043213 (2020).

[236] F. Wieben, D. Block, M. Himpel, and A. Melzer, "Configurational temperature of multispecies dusty plasmas", Physical review. E **104**, 045205 (2021).

[237] S. Schütt and A. Melzer, "Simulations and experiments of phase separation in binary dusty plasmas", Physical review. E **103**, 053203 (2021).

[238] K. Jiang and C.-R. Du, “Dynamics in binary complex (dusty) plasmas”, Reviews of Modern Plasma Physics **6**, 1–45 (2022).

[239] C. K. Goertz, “Dusty plasmas in the solar system”, Reviews of Geophysics **27**, 271–292 (1989).

[240] O. Havnes, C. K. Goertz, G. E. Morfill, E. Grün, and W. Ip, “Dust charges, cloud potential, and instabilities in a dust cloud embedded in a plasma”, Journal of Geophysical Research: Space Physics **92**, 2281–2287 (1987).

[241] L. Boufendi, A. Plain, J. P. Blondeau, A. Bouchoule, C. Laure, and M. Toogood, “Measurements of particle size kinetics from nanometer to micrometer scale in a low-pressure argon-silane radio-frequency discharge”, Applied Physics Letters **60**, 169–171 (1992).

[242] P. D. Haaland, A. Garscadden, B. Ganguly, S. Ibrani, and J. Williams, “On form and flow in dusty plasmas”, Plasma Sources Science and Technology **3**, 381–387 (1994).

[243] M. Dworschak, O. H. Asnaz, and F. Greiner, “A minimally invasive electrostatic particle extractor for nanodusty plasmas and its application for the verification of in situ mie polarimetry”, Plasma Sources Science and Technology **30**, 035011 (2021).

[244] R. F. Kemp and J. M. Sellen, “Plasma potential measurements by electron emissive probes”, Review of Scientific Instruments **37**, 455–461 (1966).

[245] V. I. Demidov, S. F. Adams, I. D. Kaganovich, M. E. Koepke, and I. P. Kurlyandskaya, “Measurements of low-energy electron reflection at a plasma boundary”, Physics of Plasmas **22**, 104501 (2015).

[246] B. G. Heil, J. Schulze, T. Mussenbrock, R. P. Brinkmann, and U. Czarnetzki, “Numerical modeling of electron beams accelerated by the radio frequency boundary sheath”, IEEE Transactions on Plasma Science **36**, 1404–1405 (2008).

[247] Z. Donkó, J. Schulze, U. Czarnetzki, A. Derzsi, P. Hartmann, I. Korolov, and E. Schüngel, “Fundamental investigations of capacitive radio frequency plasmas: Simulations and experiments”, Plasma Physics and Controlled Fusion **54**, 124003 (2012).

[248] J. Schulze, Z. Donkó, E. Schüngel, and U. Czarnetzki, “Secondary electrons in dual-frequency capacitive radio frequency discharges”, Plasma Sources Science and Technology **20**, 045007 (2011).

[249] M. Artz, “Schnelle Bestimmung des Ladungs-zu-Masse-Verhältnisses von Staubteilchen in der Plasmarandschicht mittels Pulsanregung”, Bachelor Thesis (CAU, Kiel, 2022).

Eidesstattliche Erklärung

Ich, Armin Mengel, versichere an Eides statt, dass diese Dissertation mit dem Titel „Measuring Electron Sticking Coefficients using Dust in Plasma" folgende Bedingugen erfüllt: Diese Arbeit wurde eigenständig von mir verfasst, und verwendet – abgesehen von der Beratung durch meinen Betreuer PD. Dr. Franko Greiner – nur die angegebenen Hilfsmittel. Diese Arbeit ist unter Einhaltung der Regeln Guter Wissenschaftlicher Praxis *der Deutschen Forschungsgemeinschaft entstanden. Diese Arbeit wurde weder als Ganzes noch in Teilen zuvor zum Zwecke eines Prüfungsverfahrens an anderer Stelle vorgelegt. Teile der Arbeit wurden bereits publiziert, oder zur Publikation eingereicht, wie angegeben. Mir wurde niemals ein akademischer Grad entzogen.*

Kiel,

_____

Armin Mengel

Danksagung

An dieser Stelle möchte ich allen Menschen danken, die mich während der Promotion unterstützt haben, und ohne die diese Arbeit in dieser Form nicht möglich gewesen wäre.
Allen voran danke ich natürlich PD Dr. Franko Greiner für die Möglichkeit, an diesem Projekt als Doktorand zu arbeiten, und die (inzwischen fast 8 Jahre zurückliegende) Aufnahme in die Arbeitsgruppe, damals als Studentische Hilfskraft. Ich konnte mich bei Fragen, Unsicherheiten oder Problemen fachlicher und organisatorischer Natur stets an ihn wenden. Seine Ideen für Forschungsprojekte jenseits eingefahrener Grenzen zwischen einzelnen Fachgebieten und sein unermüdlicher Einsatz für seine Mitarbeitenden sind eine Bereicherung für die Arbeitsgruppe, und haben für eine angenehme Atmosphäre während der Promotion gesorgt.
Ich möchte auch Prof. Jan Benedikt für die Aufnahme in den größeren Kontext der AG Experimentelle Plasmaphysik danken, und für kurze Dienstwege in dringenden Fällen.
Auch danke ich PD Dr. Franz Xaver Bronold und Prof. Lorin Swint Matthews für die erfolgreichen und erhellenden Kollaborationen, und die Möglichkeit sehr spezifischer fachlicher Fragen.
Weiterhin gilt mein Dank all jenen, die mich während der Promotion mit Ratschlägen, Fachwissen, und Ermutigung unterstützt haben. Besonders hervorheben möchte ich dabei Kerstin Sgonina, Sören Wohlfahrt, und Andreas Petersen, die ich ohne zu zögern jederzeit um Rat fragen konnte. Dr. Oguz Han Asnaz und Dr. Hendrik Jung danke ich für die fachliche Unterstützung am Beginn des Projektes, ohne die ich das Rad hätte neu erfinden müssen.
Karin Hansen und Isabel König danke ich für ein unproblematisches und kollegiales Zusammenleben im gemeinsamen Büro, und Alexander Schmitz für unvergessliche (möglicherweise nicht komplett fachliche) Diskussionen. Ich danke auch den anderen Doktoranden Maren Dworschak, Tristan Winzer, Christian Schulze, He Li, Yang Liu, Natascha Blosczyk, Jana Mergemeier, Görkem Bilgin und Alex Quack, dem Postdoc Dr. Luka Hansen und allen Masteranden und Bacheloranden für eine stets angenehme und produktive Atmosphäre und für erinnerungswürdige Tagungsreisen. Mein Dank gilt natürlich auch Volker Rohwer, Michael Poser und Frank Brach für erstklassige technische Betreuung, die den Aufbau des Experiments erst möglich gemacht hat. Im gleichen Zuge müssen natürlich auch Tobias Marten und das Team der zentralen Werkstatt erwähnt werden. Danke für eure kompetente Umsetzung von bloßen Ideen in Bauteile, die maßgeblich zur Realisierung der Sticking Machine beigetragen haben. Stephanie Thiedemann danke ich für ihre Hilfe bei allen erdenklichen bürokratischen Angelegenheiten.
Ein besonderer Dank gilt natürlich auch meinen Eltern, Martina und Albrecht Mengel, und meiner Schwester Marion, die mich während meiner gesamten Studienzeit immer unterstützt haben. Auch möchte ich Sadia Gernandt dafür danken, dass sie abseits

der Uni immer für mich da ist.
Zu guter Letzt bedanke ich mich bei allen derzeitigen wie ehemaligen Mitgliedern der Arbeitsgruppe für eine wunderbare Atmosphäre und zahllose Kaffeepausen, oftmals geprägt von aus verschiedensten Gründen mitgebrachtem Kuchen und/oder unterschiedlich absurden Gesprächsthemen, sowie für eure schier unerschöpfliche Toleranz gegenüber Wortwitzen. An diese 8 Jahre mit euch werde ich wohl immer gerne zurückdenken.